

1-1-2011

Optimal Port Placement And Automated Robotic Positioning For Instrumented Laparoscopic Biosensors

Brady King
Wayne State University

Follow this and additional works at: http://digitalcommons.wayne.edu/oa_dissertations

Recommended Citation

King, Brady, "Optimal Port Placement And Automated Robotic Positioning For Instrumented Laparoscopic Biosensors" (2011).
Wayne State University Dissertations. Paper 214.

This Open Access Dissertation is brought to you for free and open access by DigitalCommons@WayneState. It has been accepted for inclusion in Wayne State University Dissertations by an authorized administrator of DigitalCommons@WayneState.

**OPTIMAL PORT PLACEMENT AND AUTOMATED ROBOTIC
POSITIONING FOR INSTRUMENTED LAPAROSCOPIC
BIOSENSORS**

by

BRADY KING

DISSERTATION

Submitted to the Graduate School

of Wayne State University,

Detroit, Michigan

in partial fulfillment of the requirements

for the degree of

DOCTOR OF PHILOSOPHY

2011

MAJOR: Computer Engineering

Approved by:

Advisor

Date

**© COPYRIGHT BY
BRADY KING
2011
All Rights Reserved**

DEDICATION

To my parents

Thank you for giving me all the opportunities and tools needed to succeed

ACKNOWLEDGEMENTS

I would first like to thank my family: my parents, my brothers, and everyone else. You have been so supportive over the years, making sure that I always had what I needed to succeed. Thank you for everything you have done, for all the love and support, and for helping me even though I can be a bit of pain now and then.

I would like to thank my girlfriend Sheryl. You have been here since I started this journey, and without you I don't think I would be here at the end. Thank you for your unwavering support and love.

I would like to thank my advisor, Dr. Abhilash Pandya. You have been a constant supporter and close friend through my years at Wayne State. You have provided me with the tools and encouragement to exceed my limitations and to strive beyond what I thought I could do. When I first came to Wayne State, I had no idea that I would be doing medical research. Your enthusiasm in this area has inspired me over the years and will never forget that. I would like to thank Dr. Darin Ellis for help in setting up subject tests. Without you I would have been lost in a statistics maze. Thank you for all of your help, valuable advice, and serving on my dissertation committee. I would like to thank Dr. Greg Auner for the SSIM group and serving on my dissertation committee. Without you, none of this work would be possible. I would also like to thank Dr. Le Yi Wang for serving on my dissertation committee.

There are several colleagues that I must recognize. Luke Reisner... who would have thought on that day 26 years ago when we met that we would be here, still best friends and trying to both get a Ph.D. You have helped me with so much over the years from writing

papers, to doing research, to finishing the latest video game. Thanks for everything! Alex Cao, our resident “go to” guy. You have done so much, not just for me, but our entire research group, and I can’t thank you enough. Dr. Lavie Golenberg has been my friend since I started here at Wayne State. Thank you for all the help with my various projects and being there to play cards with whenever I needed a break. Dr. Keshav Chintamani helped me decide how to tackle the AESOP 1000 robot. Without you this project never would have taken off. Dr. Yang Zhao gave me my teaching assistant position, getting me paid to do what I love. Thank you for your support and trust. Dr. Michael Klein and Dr. Madhu Prasad, you both have been so generous with your time, allowing me to experience things at the hospital that I never thought I would get to see. Mohammand Syed, you did a huge amount of work to develop the robotic test platform. Thank you for all of your help and hard work. I would like to thank Ajay Mudunuri, who I have worked with on spin off projects over the last few years. You’re an incredible researcher and I wish you all the luck in future.

Finally, the contributions of the numerous colleagues and friends of the CARES research group must be acknowledged. You all have done such great work: Sam Li, Dr. Shawn Hunt, Dr. Rachel Kast, Steve Dworzecki, Prem Sivakumar, Umer Khalid, and many many more.

TABLE OF CONTENTS

Dedication.....	ii
Acknowledgements	iii
List of Figures	ix
Chapter 1: Introduction and Motivation.....	1
1.1 Motivation and Problem Statement.....	3
1.2 Research Objectives and Specific Aims	4
1.3 Outline of the Dissertation	6
Chapter 2: Background	8
2.1 Biosensors	8
2.1.1 Raman Spectroscopy	9
2.1.2 Why Use Raman Spectroscopy?	10
2.2 Medical Robotics	12
2.2.1 Why Do We Need Medical Robotics?.....	16
2.3 The Importance of Port Placement in Laparoscopic Surgery	17
2.4 What is Image-Guided Surgery?	18
2.4.1 Why is Image-Guided Surgery Important?	20
Chapter 3: Optimized Port Placement	22

3.1 Background	22
3.2 Methods.....	25
3.2.1 Reachable Point Algorithm.....	28
3.2.2 Identifying the Best Port Location.....	33
3.2.3 Visualization.....	34
3.3 Results.....	36
3.4 Discussion	41
Chapter 4: Human Performance in the Task of Port Placement.....	45
4.1 Methods.....	45
4.1.1 Participants.....	45
4.1.2 Apparatus	46
4.1.3 Experimental Task	46
4.1.4 Trial-Level Procedure.....	48
4.1.5 Experimental Design.....	48
4.2 Results.....	54
4.3 Problem Scenarios	61
4.3.1 Separating Ridge.....	61
4.3.2 Multiple Targets Separated by Distance	62
4.3.3 Significant Distance from Target	63

4.3.4 Indented Ridge	64
4.3.5 Obstructions	65
4.4 Discussion	67
Chapter 5: Automating Biosensor Probe Placement	70
5.1 Background	70
5.1.1 Denavit-Hartenberg (D-H) Notation	73
5.1.2 Locating the End-Effector (Forward Kinematics)	75
5.1.3 Optical Encoders.....	79
5.2 Methods.....	80
5.2.1 Test Platform	80
5.2.2 Physical Parameters	83
5.2.3 Positioning the End-Effector (Inverse Kinematics).....	87
5.3 Results.....	94
5.3.1 Home Position and Encoder Conversion.....	95
5.3.2 D-H Parameters	96
5.3.3 Registration	97
5.3.4 Port Location Registration.....	97
5.4 Discussion	98
Chapter 6: Summary, Applications, and Future Work	100

6.1 Summary/Contributions	100
6.2 Applications and Future Research	101
6.2.1 Robotically Positioned Raman Biosensor	102
6.2.2 Automated Laparoscopic/Robotic Surgical Camera Placement	104
6.2.3 Port Placement Training	105
6.2.4 Optimized Ablation.....	105
Appendix A: AESOP 1000 Control Pins.....	107
Appendix B: AESOP 1000 Linear Joint Encoder Conversion	110
Appendix C: AESOP 1000 Shoulder Joint Encoder Conversion	111
Appendix D: AESOP 1000 Elbow Joint Encoder Conversion	112
Appendix E: AESOP 1000 Wrist Joint Potentiometer Conversion.....	113
Appendix F: AESOP 1000 Finger Joint Potentiometer Conversion	114
Appendix G: AESOP Positional Accuracy Tests.....	115
Bibliography.....	118
Abstract	128
Autobiographical Statement.....	130

LIST OF FIGURES

Figure 1-1: Data flow in the conceived system.....	6
Figure 2-1: Raman spectra for various tissue types. The y-axis represents the amount of photons observed. Image provided with permission from authors of [8].....	10
Figure 2-2: A Raman probe attached to an InPhotonics portable Raman spectrometer.....	11
Figure 2-3: Laparoscopic tools	13
Figure 2-4: The da Vinci surgical system. The surgeon sits at the control station on the left, while the tools are inserted into the patient on the right. Image © 2011 Intuitive Surgical, Inc.....	14
Figure 2-5: The AESOP medical robot holding an endoscope for a surgeon. Image © 2011 Intuitive Surgical, Inc.	16
Figure 2-6: Laparoscopic tools and endoscope in the “Golden Triangle” arrangement. The triangle here refers to the location of the ports on the patient’s skin.	18
Figure 2-7: A virtual reality view (left) and augmented reality view (right) of a phantom skull .	19
Figure 3-1: Raman spectra of naphthalene captured with a Raman probe at angles of 45° and 90° (perpendicular)	23
Figure 3-2: Data flow within the system.....	26
Figure 3-3: Raman spectroscopy probe	27
Figure 3-4: Diagram of the collision test algorithm. A collision occurs when $ v_2 < v_1 $ and x is less than the radius of the biosensor.	30
Figure 3-5: Flowchart of the Reachable Point Algorithm	32
Figure 3-6: Flowchart for selection of best possible port location. This method is optimized for cancer detection using Raman spectroscopy (maximizing the number of reachable points). Other methods can be utilized as necessary.	34
Figure 3-7: Target volume selection (red box) within the visualization system.....	35
Figure 3-8: Cross-sectional views of five test scenarios used to validate the performance of the system	37

Figure 3-9: Port placement within the visualization system. The blue box encloses potential port locations, with the green dot indicating the optimal location for use with the enclosed red target area. 40

Figure 3-10: Visualization system showing all points reachable (green markers) by the biosensor from the manually selected port location (green dot) 41

Figure 3-11: Example of a collision that would be undetected due to wide triangle point spacing. This problem can be prevented with a pre-processing stage..... 43

Figure 4-1: Example test scene from section 1. The pink sphere is the skin surface, and the enclosed blue model provides the target surface. The red dots represent target points. The red cylinder is a representation of the Raman probe, which provides a reference for scale. The letters are used by 3D Slicer to provide information about the current viewpoint (right, anterior, posterior, etc.)..... 49

Figure 4-2: Close-up view of a section 2 test scene that demonstrates a complex target surface 50

Figure 4-3: Close-up view of a section 3 test scene that demonstrates large target surface area 51

Figure 4-4: Close-up view of a section 4 test scene that demonstrates a complex skin surface 52

Figure 4-5: Close-up view of a section 5 test scene that demonstrates an obstruction 53

Figure 4-6: Average percentage of maximum (PoM) points reached for each test section. The black vertical lines represent the 95% confidence interval about each mean. 55

Figure 4-7: Average percentage of maximum (PoM) points reached for each participant over all test scenes. The black vertical lines represent the 95% confidence interval about each mean. 56

Figure 4-8: Performance for the baseline/control section. Squares represent the port placer system’s performance, while diamonds represent the average participant performance. The black vertical lines represent the 95% confidence interval about each mean. 57

Figure 4-9: Performance for the complex target surface section. Squares represent the port placer system’s performance, while diamonds represent the average participant performance. The black vertical lines represent the 95% confidence interval about each mean. 58

Figure 4-10: Performance for the expansive target surface section. Squares represent the port placer system’s performance, while diamonds represent the average participant

performance. The black vertical lines represent the 95% confidence interval about each mean.	59
Figure 4-11: Performance for the complex skin surface section. Squares represent the port placer system’s performance, while diamonds represent the average participant performance. The black vertical lines represent the 95% confidence interval about each mean.	60
Figure 4-12: Performance for the obstructions section. Squares represent the port placer system’s performance, while diamonds represent the average participant performance. The black vertical lines represent the 95% confidence interval about each mean.	61
Figure 4-13: Example of the “separating ridge” scenario. The green circle represents the correct choice for port placement, while the blue squares represent typical choices made by participants. The red triangles represent the target points.....	62
Figure 4-14: Example of the “multiple targets separated by distance” scenario. The green circle represents the correct choice for port placement, while the blue squares represent typical choices made by participants. The red triangles represent the target points.....	63
Figure 4-15: Example of the “significant distance from target” scenario. The green circle represents the correct choice for port placement, while the blue squares represent typical choices made by participants. The red triangles represent the target points. The probe model was shown in all scenes to give participants a representation of its length.	64
Figure 4-16: Example of the “indented ridge” scenario. The correct choice for port placement (the green circle) is surrounded by the choices of participants (blue circles). The red triangles represent the target points.....	65
Figure 4-17: Examples of the “obstructions” scenario. The top diagram demonstrates a scenario in which the choice is obvious, whereas the bottom demonstrates a scenario in which the choice is ambiguous. The green circles represent the correct choices for port placement, while the blue squares represent typical choices made by participants. The red triangles represent the target points.....	66
Figure 5-1: AESOP 1000 robotic arm.....	71
Figure 5-2: AESOP 1000 motion controller	71
Figure 5-3: The AESOP 1000 in the default position. Joint names are nicknames for easy reference.	72
Figure 5-4: A three degree-of-freedom robot	74

Figure 5-5: Example of standard D-H notation	75
Figure 5-6: Fiducial markers in a virtual scene and their corresponding markers on the real object. Image provided with permission from author of [14].	78
Figure 5-7: Quadrature optical encoder outputs for sensors A and B for clockwise and counter-clockwise movements of a motor	79
Figure 5-8: AESOP 1000 break-out box and block diagram	81
Figure 5-9: Galil motion controller attached to the break-out box.....	82
Figure 5-10: Diagram of the D-H configuration of the AESOP 1000 robot	84
Figure 5-11: Starting and intermediary positions for robot movement from current target to next target	93
Figure 6-1: The Raman probe, attached to the end of the MicroScribe G2X, is used to scan a plastic cup and other objects with the phantom skull.....	103
Figure 6-2: A screenshot of our visualization system showing 3D models (derived from CT imaging of the phantom skull), the location of the tracked Raman probe, collected Raman spectra, and colored markers denoting the classifications (computed from Raman scan data) of various objects within the skull.....	104

CHAPTER 1: INTRODUCTION AND MOTIVATION

Medical biological sensors (biosensors) are a relatively new area of research. Even more novel are sensors affixed to surgical tools, capable of gathering a multitude of types of data, obtaining information from inside the body. Many different types of sensors are being developed such as various compound detectors, temperature measurement, ultrasound, optical spectroscopy, thermo imaging, and more [1-4]. For instance, biosensors based on Raman spectroscopy (a light-based sensing technique) have been shown to be very effective at identifying various forms of cancer [5-8]. Raman spectroscopy biosensors are now made in a probe form, similar to a laparoscopic camera, for use *in vivo*.

An application where biosensors can play a significant role is surgical resection of cancerous tissue. Cancer kills over 500,000 people each year in the U.S. alone [9, 10]. In many cases, a surgical resection is the most effective way of treating it. However, there is no definitive way of determining the amount of tissue that should be excised. A typical resection procedure consists of two phases. The first, the intraoperative gross examination, involves the surgeon removing obvious tumor tissue. The second phase, the postoperative histologic examination, is done by a pathologist who determines the margins of the tumor. This process generally takes 24–48 hours, and it may result in a positive margin, indicating an incomplete resection. Thus, a second procedure is required to remove cancer at the margins, further risking the patient's life. Research has shown that if negative margins (indicating a lack of cancer in the surrounding tissues) can be achieved, the need for follow-up procedures is greatly reduced [11, 12]. A frozen section analysis attempts to achieve this during the operation by

taking a small slice of the excised tissue and looking for evidence of tumor tissue at the margins. However, this is not a complete analysis due to its discrete approach. Moreover, it can still take 20 minutes per specimen tested, possibly adding hours to the operation. During this process, the patient is still on the operating table, under the risk of infection and other complications.

Recently, robotic surgery is increasingly being used in medical procedures [13]. With advantages such as motion scaling, tremor filtration, and dexterity enhancement, robotics is proving its ability to augment a surgeon's performance. Medical robots manipulate laparoscopic tools through small ports in the patient's skin. These smaller incisions lead to less trauma for the patient and faster recoveries. Although still frequently slower than laparoscopic surgery, the robot's advantages can outweigh the extra time. For example, with robotics it is possible to use more than two ports/arms, enabling the surgeon to use the additional arms to hold tissue or carry sensors for monitoring. These robots can be tracked very accurately and visualized within a virtual 3D workspace, allowing the surgeons to visualize what they can't directly see with their eyes [14]. These virtual environments can be realized in either virtual or augmented reality.

There is potential to further enhance a surgeon's performance by combining biosensors with the rigid platform of medical robotics. For example, by leveraging Raman spectroscopic probes, it may be possible to map tumor margins. Some other techniques have been developed to aid in margin assessment, including optical mammography analysis and methods using optical tomography. However, as of yet, none have achieved widespread use [15-17]. Utilizing the positioning and tracking abilities of robotics in conjunction with the diagnostic abilities of Raman spectroscopy could enable for accurate margin assessment. Technology

capable of ensuring a complete resection would prevent secondary procedures and reduce the risk to patients' lives.

The overall goal of this research is to provide techniques that best leverage biosensors' diagnostic capabilities. Because it is representative of many biosensors and the subject of current research, a Raman probe is used as the proof of concept biosensor. Therefore, the aim is to create a system capable of defining a tumor's margin quickly and accurately during a patient's first procedure. A medical biosensor capable of distinguishing between normal and malignant cells is integrated with an image-guided surgery visualization system and robotic surgery hardware. The robotic hardware could enable safe and accurate positioning of the biosensor within the body, while information derived from the sensor could be displayed in an image-guided surgery system to aid in the visualization of lesions. This information would allow the surgeon to visualize the margins of a tumor before removing any tissue.

1.1 Motivation and Problem Statement

In order to use a biosensor *in vivo*, several problems must be addressed. First, the biosensor must be threaded into the body through a port. The port is a hole in the patient's skin through which tools, sensors, or cameras can be threaded, allowing access to the internal structures with little trauma. Port placement in laparoscopic procedures is currently done by a surgeon based on previous knowledge and experience. The port represents a pivot point, which adds significant limits on the reachable target surfaces within the body due to physical constraints. In addition, most biosensors have particular configurations in which they can be manipulated (degrees of freedom) and limited distance or angles (angles of incidence) in which they can operate. When limits such as the angle of incidence are reached or exceeded, data

collection will be poor or impossible. Because of these physical limitations, the surgeon must be able to visualize the target areas in relation to the pivot point (port) to ensure total target accessibility, which is quite challenging.

Second, many current biosensors only obtain data from a very small area (e.g. 150 microns in diameter), and future incarnations may collect from even smaller areas. This requires the sensor to be placed at many target points in order to map tumor margins, which is challenging and compounds the first problem. For this reason, manually holding and moving the biosensor may not be possible as stability (due to hand tremors) and accuracy are not within acceptable limits for the sensor.

Third, the surgeon needs to be able to define the areas of interest for scanning and see the possible port locations required for the particular sensor that is being used. Current image-guided surgery systems use CT, MRI, and ultrasound data to generate virtual reality 3D views, while augmented reality 3D views are less common. However, these systems currently do not provide any type of control of biosensors or presentation of biosensor data.

1.2 Research Objectives and Specific Aims

This section outlines work towards creating techniques and tools to enable biosensors to be best utilized in the surgical environment. Each area of research is described below as a separate specific aim.

The port location the biosensor is threaded through determines the quality of data it obtains. As stated above, this task is non-trivial. My *first specific aim* was the development of a program to aid the surgeon in planning of the best possible port placement for proper biosensor use. This program is abstracted for use with any biosensor, but tested with the

Raman probe. It uses 3D data obtained from pre-operative imaging and calculates the best port location on the patient's skin, facilitating the biosensor's operation. In addition, visual control of this software is integrated with an image-guided surgery system.

The port placement system has functions for evaluating the quality of a user selected port location. Until now, this type of determination was impossible. My *second specific aim* was to use this system to determine cases where human port placement is diminished. By identifying these scenarios, it will be possible to create training programs and further enhance the port placement system.

Precise positioning of the biosensor and scanning techniques are needed to move the biosensor to cover a large area of interest. A biosensor probe is attached to a robot manipulator to enable positioning it at a specific site, holding it steady, and taking measurements. A reasonable choice for this robot is the AESOP 1000 (Intuitive Surgical, Inc., Sunnyvale, CA) robotic manipulator. This robot is medically approved but has no accessible interface to control specific joint angles and positions. My *third specific aim* was to develop control algorithms to position the AESOP's end-effector (the tip of the attached tool, which in this case is the biosensor) at a desired location. The robot is evaluated for accuracy. Specific factors contributing to its accuracy are identified for future consideration in robotic systems. In addition, control over movements and data capture is integrated into an image-guided surgery system.

In Figure 1-1 we can see the interconnection of the separate components. In this configuration, the port placer, visualization system, and robot control software exist as

separate entities. In this way, it is possible to integrate additional software and hardware if desired.

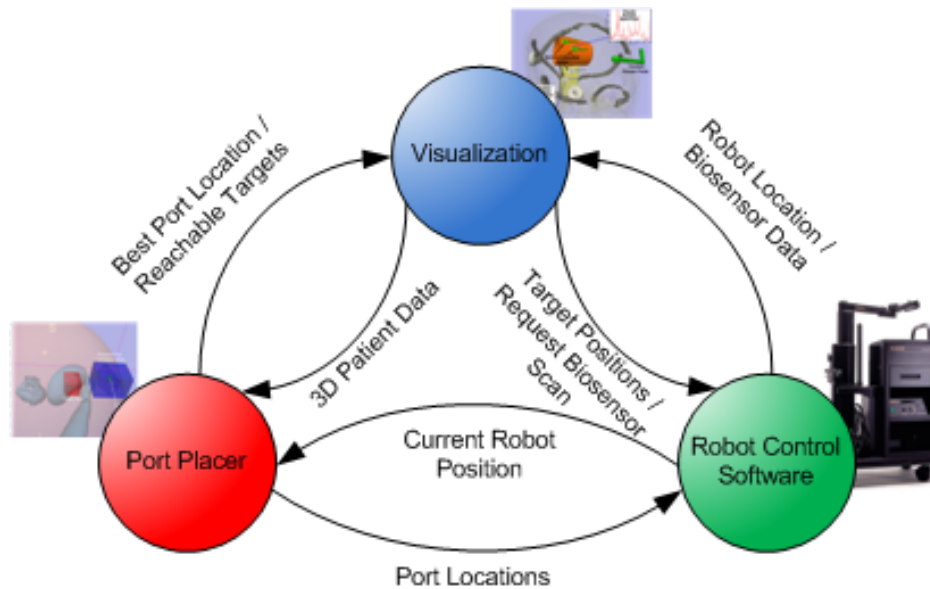


Figure 1-1: Data flow in the conceived system

1.3 Outline of the Dissertation

The outline of the dissertation is as follows: Chapter 2: provides background information on medical robotics and image guided surgery. A section is also provided on Raman spectroscopy, since it is the biosensor of choice for implementation and testing.

Chapter 3: describes the implementation details of an automated port placement system. This system indicates the best possible port location, which maximizes the data collection potential of a particular biosensor based on patient data and biosensor limitations. In this chapter, biosensor-specific limitations are based on a Raman spectroscopy probe.

Chapter 4: describes a human factors study in which the major question is: “What is typical human performance in the task of port placement for biosensor use?” A secondary question is “Are there scenarios in which human performance is degraded?”

Chapter 5: describes the technology necessary to automate the placement of a biosensor *in vivo*. This chapter includes implementations details and a discussion of the accuracy of a current robotic platform.

Chapter 6: summarizes the findings in this dissertation, discusses possible applications including preliminary investigations, and suggests future work.

CHAPTER 2: BACKGROUND

In this chapter the definitions of the technology used to develop this dissertation are given. First, biosensors are described along with a description of a particular biosensor chosen for demonstration of this work. Second, a literature survey of the advantages and disadvantages of medical robotics and port placement are given. Finally, image-guided surgery is defined with respect to both virtual and augmented reality.

2.1 Biosensors

In the medical field, “biosensors” can refer to any type of device that detects the biological makeup of some target, gathering any of a multitude of types of data in the process. Many of these devices are small sensors that gather the data from within the body [1-4]. These sensors can be affixed to the end of surgical instruments and threaded into the body. Monitoring such things as glucose levels, blood flow, and even disease stages, biosensors lead to more informed decisions and accurate analyses of patients.

Related to the field of biosensors is that of treatment delivery tools. These tools are also threaded into the body, affixed to the end of surgical instruments. However, these tools treat disease instead of detecting it. Examples include microwave ablation, cryoablation, and radiofrequency ablation. It is conceivable to have both a detection and treatment system mounted on the same tool. In this case, the port placement issues would be similar, and detection and treatment could occur simultaneously.

2.1.1 Raman Spectroscopy

Raman spectroscopy is a non-invasive technique for analyzing the molecular makeup of substances [18]. Coherent laser light (at a particular frequency) is shined onto a specimen, and the scattered light is analyzed. Most of the light coming back is Rayleigh-scattered, meaning it has the same energy as the excitation beam. A small amount of light is Raman-scattered, a process where a molecule absorbs a photon while simultaneously giving off another photon at a different energy level. This photon scatters with a different wavelength than the excitation source. The amount of light shifted and the wavelengths of the light correspond to the frequency of the vibrating modes of the molecules in the target. A Raman spectrum is made up of the number of photons scattered, referred to as intensity, and the specific wavelengths at which they are scattered (see Figure 2-1). By studying the amount of photons scattered in this manner and the wavelength which they scatter, Raman spectroscopy allows us to analyze the molecular makeup of a target.

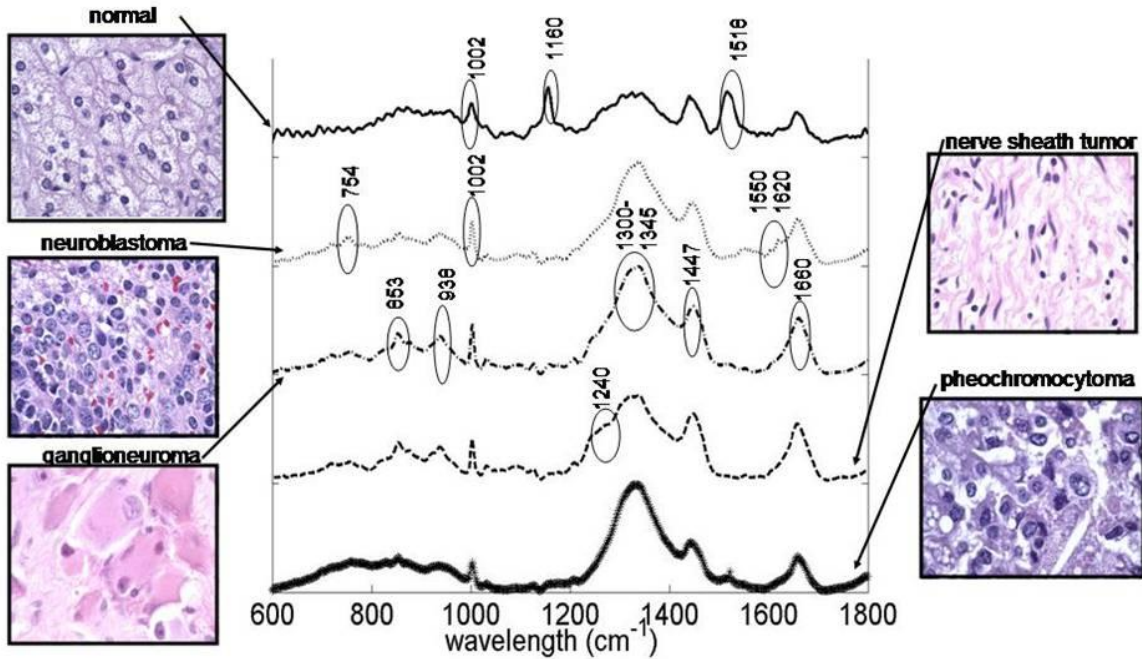


Figure 2-1: Raman spectra for various tissue types. The y-axis represents the amount of photons observed. Image provided with permission from authors of [8].

2.1.2 Why Use Raman Spectroscopy?

Cancer, at its most basic form, modifies the molecular makeup of cells. Therefore, by looking for specific features in a Raman spectrum, one can distinguish normal and malignant cells [5-8]. This classification is now done by computer using various techniques such as principal component analysis, support vector machines, and neural networks [19-21]. The promise of this technology is threefold. First, this technique can collect and classify a spectrum in near real time, meaning a diagnosis can be done within minutes rather than the 20 minutes for frozen section analysis or the hours for a postoperative histologic exam [22]. Second, because of its non-destructive nature, the risk of removing more tissue than is needed (for histology) is eliminated because a diagnosis can be done *in vivo* [22-24]. And third, the sensitivity of Raman spectroscopy allows for the assessment of tumor grades [25, 26].

Due to these properties, a Raman spectrometer may be ideal for *in vivo* cancer detection. There are many groups adapting Raman spectrometer technology for use on human tissue [3, 27, 28]. Raman probes are fiber optic devices attached to a Raman spectrometer that facilitate the collection of Raman spectra from human tissue. These Raman probes are capable of being threaded into the body in the same fashion as cameras and laparoscopic tools for minimally invasive surgery (see Figure 2-2). Raman spectroscopic probes are also representative of typical biosensors. Current Raman probes are rigid in design and gather data from a single small point on the surface of tissue. For these reasons a Raman probe is a sensible choice of an example for this research.



Figure 2-2: A Raman probe attached to an InPhotonics portable Raman spectrometer

2.2 Medical Robotics

In general, there are two types of surgery. Open surgery involves a large incision in the patient and allows the surgeon to use tools and his hands directly on the target site. Minimally invasive surgery involves small ports through which instruments are threaded. The benefits of this compared to open surgery are reduced trauma to the patient and faster recovery time [29-31]. Currently the most common form of minimally invasive surgery is laparoscopy. Laparoscopic tools are long, tube-like instruments with mechanical manipulators on the end (see Figure 2-3). The surgeon positions and manipulates these tools by hand. A camera called an endoscope, similar in design to the tools, is inserted through another port, enabling the surgeon to see the surgical site on a monitor.



Figure 2-3: Laparoscopic tools

Medical robotic surgery is a new form of minimally invasive surgery that uses robots under the surgeon's control. In this type of surgery, tools similar to laparoscopic ones are used in a comparable fashion, but they are held, positioned, and manipulated by a robot. The surgeon controls the robot from a remote console with hand controllers (see Figure 2-4).



Figure 2-4: The da Vinci surgical system. The surgeon sits at the control station on the left, while the tools are inserted into the patient on the right. Image © 2011 Intuitive Surgical, Inc.

While laparoscopy adds benefits for the patient, the surgeon's work is more difficult [32]. The surgeon's vision of the surgical site is limited by the camera view. Because the tools are inserted through ports, all movements at the end-effector (the tip of the tool) are reversed in direction. That is, because there is now a pivot point between the surgeon's hands and the tool tip, an upward motion of the surgeon's hands results in a downwards movement at the end-effector. In addition, tremors and inaccuracies are amplified due the length of the tools.

Medical robotics addresses some of the limitations of laparoscopic surgery while adding some useful features. Robotically actuated joints provide far greater accuracy than any human in positioning a tool [33]. The hand controller interface enables motion scaling, whereby movements at the surgeon's hands can be scaled down to smaller movements at the surgical

site. The hand controller interface also enables the filtration of tremors in the surgeon's hands. In addition, the surgeon no longer has to be standing and possibly arched over the patient for the entire length of the surgery. Current robotic surgery systems have an interface whereby the surgeon sits in a comfortable chair with ergonomic hand controls.

There are numerous examples of medical robots. One such example is the AESOP 1000 (Intuitive Surgical, Inc., Sunnyvale, CA), a medical robot designed to position and hold endoscopic cameras (see Figure 2-5). This robot is controlled through either voice, hand, or foot controls and frees the surgeon from having an assistant control the camera. Another example is the Zeus medical system (Intuitive Surgical, Inc., Sunnyvale, CA). Built on the basics of the AESOP architecture, Zeus adds manipulation of tools similar to laparoscopic ones. With this system, the surgeon sits at a console and controls two robotic arms through hand controls and a camera through voice control. Finally, the newest example is the da Vinci (Intuitive Surgical, Inc.). This medical robot is very similar to Zeus, but adds better dexterity at the tool-tip, 3D camera views, better ergonomic controls, and other improvements.

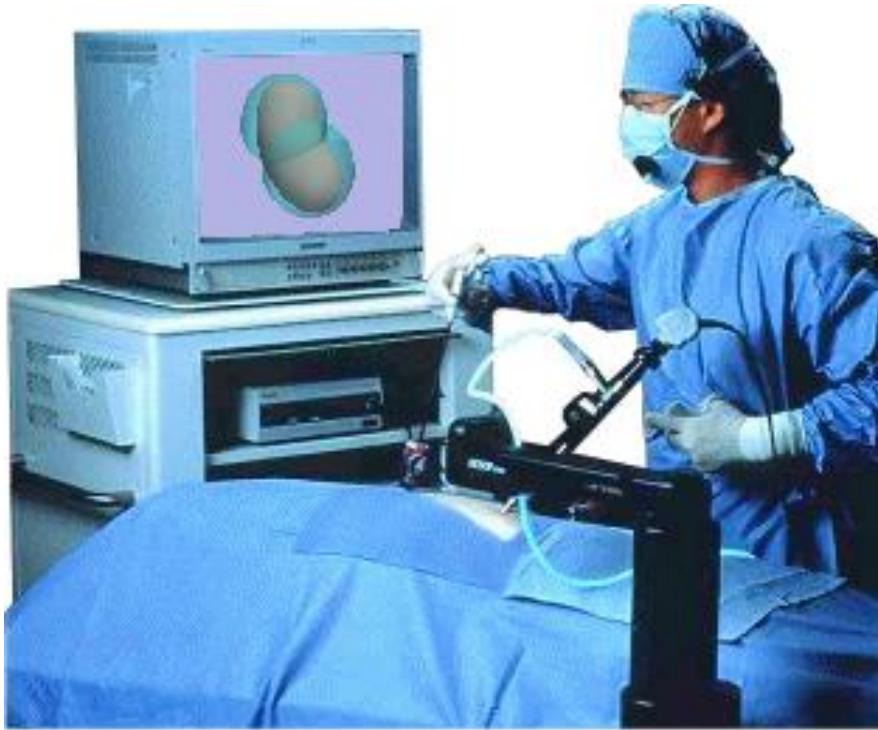


Figure 2-5: The AESOP medical robot holding an endoscope for a surgeon. Image © 2011 Intuitive Surgical, Inc.

2.2.1 Why Do We Need Medical Robotics?

Current biosensors are positioned and held by hand. Because these probes are capable of data collection from such a small area, hand stability and positional accuracy are critical to obtaining data from the targeted area. For example, many Raman probes collect spectra from an area on the order of microns in diameter. Furthermore, because of the small sampling area of a Raman probe, margin assessment involves spectra collection from many points. Hand control is inadequate for the selection of these points of interest [33].

Medical robotics provides a stable platform for both positioning and holding medical tools. The enhanced accuracy and tremor filtration provided by a robot can be applied to the use of a Raman probe and other biosensors. A robotic manipulator can facilitate Raman spectra collection by enabling precise, stable positioning and assisting in the scanning of areas of tissue. Moreover, many medical robots were designed with the ability to use many different

types of tools (scissors, cauterization tools, hooks, etc.). This ability to swap tools will allow easy integration of a Raman probe onto a medical robot. Finally, medical robots are already used in the operating room. By leveraging a medical robot, biosensors will be easier to integrate with current medical procedures.

2.3 The Importance of Port Placement in Laparoscopic Surgery

Port locations for laparoscopic surgery are chosen to create the “golden triangle” orientation (see Figure 2-6). This orientation places the surgeon’s hands on either side of the surgical site while placing their vision (through the endoscope) in the center. This orientation mimics natural viewing and working envelopes during open surgery to maximize visualization, dexterity, and comfort. These locations are most commonly chosen by the surgeon based on experience and selected during the surgery. Some automated techniques for port placement have been developed [34-40]. These techniques focus on creating the triangle of ports such that when the tools meet at the surgical site *in vivo*, they are positioned at certain angles with respect to each other. Most of these techniques focus on specific surgical procedures since the requirements for each of these procedures are different.

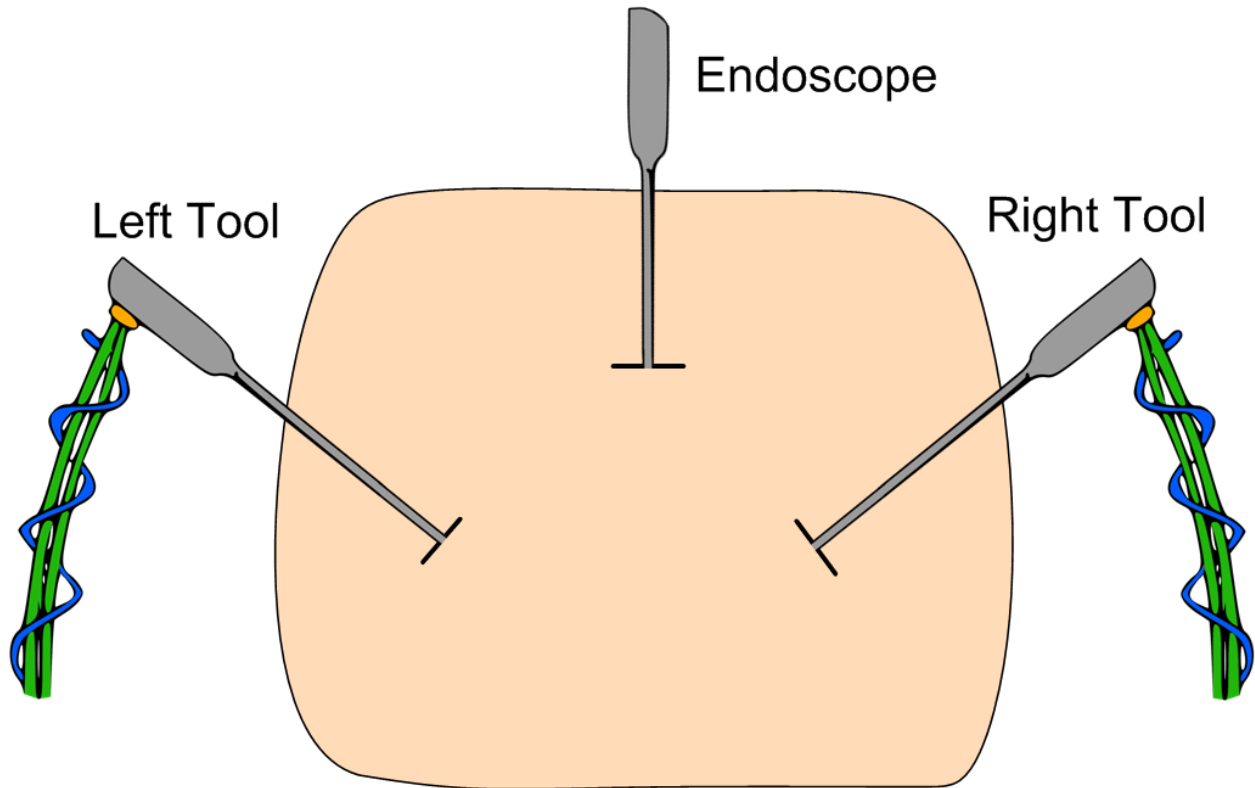


Figure 2-6: Laparoscopic tools and endoscope in the “Golden Triangle” arrangement. The triangle here refers to the location of the ports on the patient’s skin.

2.4 What is Image-Guided Surgery?

Recent advancements in medical technology have led to the use of image guidance in surgical procedures [14, 41]. Image-guided surgery is any procedure where the surgeon uses some type of device to gain an indirect image of the target site. Some examples of these devices include flexible endoscopes, fiber optic guides, and ultrasound machines. The use of these devices gives a surgeon a better view of the inside of a patient.

With more powerful computers, it is now possible to generate full 3D views of a patient to use as an additional source for image guidance. These 3D views are typically generated from pre-operative images such as CT or MRI data [14, 42]. The 3D data is then “registered” to the patient, allowing tools whose movements are tracked in real time to be seen in the virtual

environment [43, 44]. This type of technology is now used in minimally invasive surgery [45, 46], enabling the surgeon to visualize the relative locations of targets and tools inside a patient without actually being able to see them.

Augmented and virtual reality can be used to display these 3D views (see Figure 2-7). In a virtual reality environment, the 3D models of the patient and tools are rendered on a computer screen. Augmented reality, an extension of virtual reality, overlays the 3D data on top of real-time camera images [14, 47]. This mix of real and computer-generated views allows for a host of interesting new types of data to be presented to the surgeon. For example, it can be used to provide a view similar to the popular notion of “x-ray vision”, allowing the surgeon to see through occluding structures [47, 48]. This technology can also be used to show tool trajectories and visualize port placements.

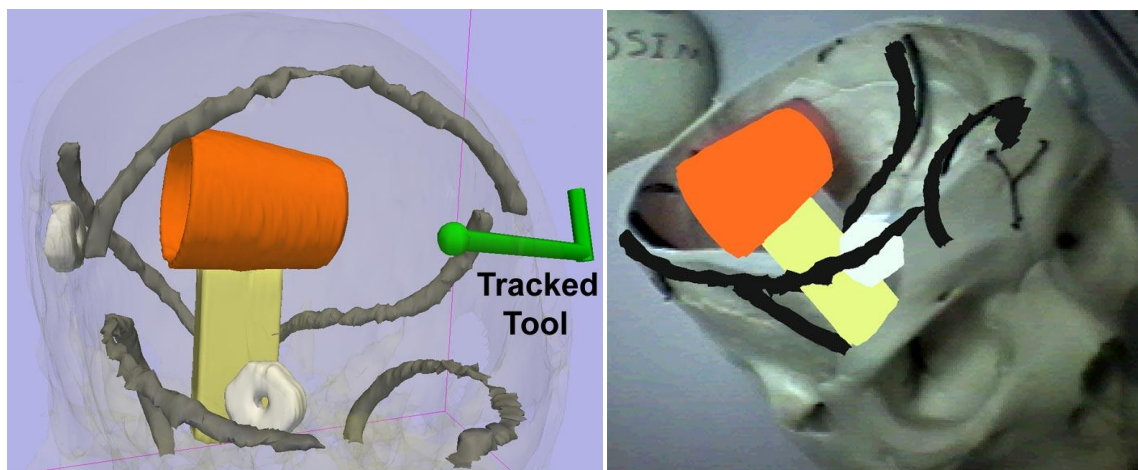


Figure 2-7: A virtual reality view (left) and augmented reality view (right) of a phantom skull

The tracking of tools can be accomplished in many different ways [49]. The use of medical robots allows tools to be tracked by measuring the individual joint angles of the robot. If the location of the base of the robot in relation to the patient is known, simple calculations using the joint angles can be performed to locate the end-effector of the robot in relation to

the patient [50]. Another type of tracking uses optical infrared reflection. Special hardware is used to precisely locate infrared reflecting material that is attached to the tools. Again, if the location of the special hardware in relation to the patient is known, calculations can be done to find the location of the tool relative to the patient. These concepts are further explained in Chapter 5: .

2.4.1 Why is Image-Guided Surgery Important?

Biosensors require precise positioning in order to collect a data from a target. In addition, biosensors can only capture high-quality data within specific physical limitations, such as the angle of incidence from the target for a Raman probe. These requirements place a significant challenge on the surgeon: proper port placement. The selection of a port location, through which the probe is inserted, is critical in ensuring total target accessibility. An image-guided surgery system, which is already set up to display patient data in 3D, would allow the surgeon to visualize the reachable targets inside the body before a port location is selected.

Once a biosensor is threaded into the body, the tip of the sensor is no longer in view. Laparoscopic instruments suffer from the same problem. Image-guided surgery systems provide navigation abilities for a surgeon by showing the relative locations of instruments and targets inside the patient. Because the biosensor can be treated as another instrument, the same navigation abilities can be applied to the probe. In addition, the 3D views of a patient enable us to present other information to the surgeon. As discussed above, the biosensor requires precision placement beyond the capabilities of human hand control, and we wish to automate the placement of the sensor. An image-guided surgery system could provide path-planning and port placement information to the surgeon. Although the system does not

directly control the movement of the sensor, this information would enable the surgeon to ensure the probe does not impinge on vital areas, such as the heart.

Once data is collected and analyzed, the results must be presented to the surgeon so he can make advised decisions. The data from the target tissue is location-specific. Because an image-guided surgery system provides configurable views of patient data, it is possible to display the results directly over patient data. This provides the surgeon with location-specific data about the target tissue and the ports that need to be placed on the surface of the patient.

CHAPTER 3: OPTIMIZED PORT PLACEMENT

Laparoscopic procedures involve the use of minimally invasive tools, which are inserted into the patient through small ports in the skin. Biosensors, such as a Raman probe, will also operate through these same ports. This chapter covers the design, implementation, and testing of an automated system to optimize the placement of these ports with respect to patient anatomy and biosensor configuration.

3.1 Background

Many of the most effective biosensor technologies (Raman spectroscopy, surface acoustic wave, electroencephalography, etc.) require near or direct contact with tissue in order to collect optimal data. Biosensors may also scan a localized region, requiring the sensor to be placed in multiple positions within a volume of interest. In addition, the angle between the probe and the tissue may be important, limiting its effectiveness when outside some operating envelope. In Figure 3-1, the data collected at a 45° angle produces a drastically weaker signal as compared to the orthogonal placement. For spectroscopic sensors, the maximum performance is typically attained when the probe is perpendicular to the tissue [3]. In addition, the size and limited degrees of freedom (flexibility) of the probe can make it difficult to achieve optimal sensor positioning. The complexity of tissue surfaces and the presence of obstructions inside the body also make the task nontrivial.

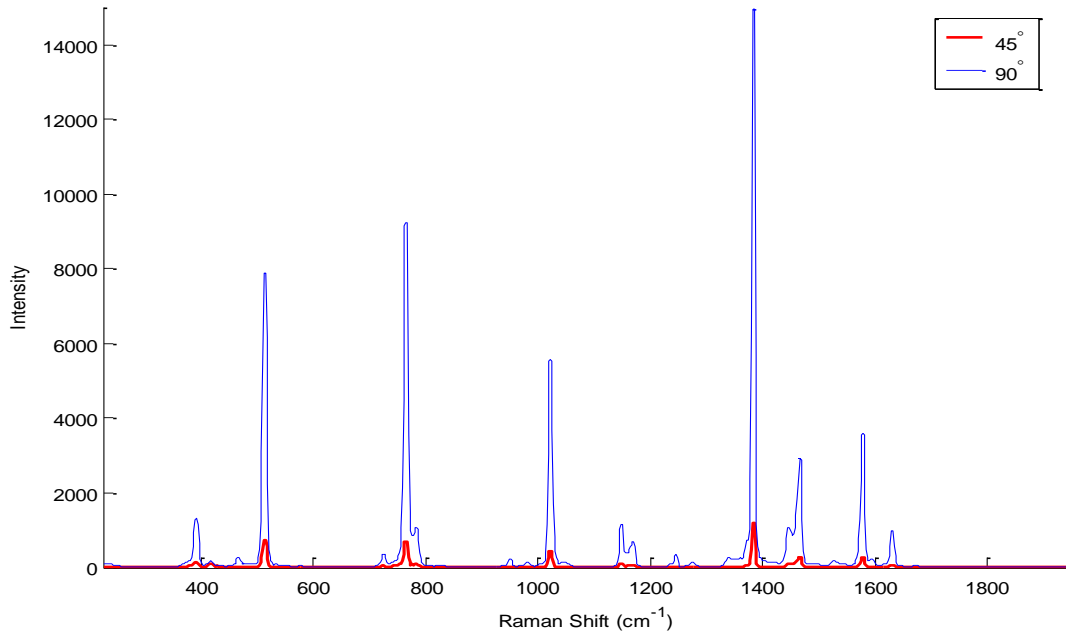


Figure 3-1: Raman spectra of naphthalene captured with a Raman probe at angles of 45° and 90° (perpendicular)

In minimally invasive medical procedures, surgeons operate through small ports in the patient's skin. Thus, any biosensor that is used during these procedures must be inserted and used through one of these ports. The biosensor must therefore pivot at a single location on the skin surface, severely limiting the positions and orientations that it can reach. Consequently, the choice of a port's location is critical to the performance of a biosensor.

An automated port placement algorithm can be used to help select an optimal location through which a probe can be threaded into the body. Some automated techniques for port placement have been developed [34-40]. In general, these techniques were designed to place two surgical instruments and a camera for laparoscopic procedures in a manner that makes the surgeon more comfortable while ensuring working accessibility. Different techniques focus on specific surgical procedures for their specific needs. For example, rib avoidance, or dexterity optimization for the surgeon during heart surgeries can be taken into account. As the

requirements for different surgeries are quite diverse, the creation of a single optimized port placement system has been difficult. Unfortunately these automated techniques do not address the needs of optimal biosensor placement.

Many of the techniques place the surgical instruments in a “golden triangle” arrangement. In this arrangement, the camera port is placed on the top of the triangle with the two surgical arm ports on either side. For biosensor placement, only a single port is required. The goal, depending on the type of sensor, is to maximize the surface area that can be scanned, or to achieve the highest quality reading. Thus, the golden triangle is not applicable for a biosensor placement. However, the golden triangle can still be used to place the endoscope and surgical tools as needed. While this work does not take into account other tools within the surgical site at the time of biosensor placement, it would be possible to consider the other tools in the collision avoidance algorithms discussed later.

Evaluating the quality of a biosensor’s port placement requires different metrics than the existing port placement techniques. Many of the existing port placement techniques focus on a specific surgical procedure (e.g. coronary artery bypass) and its outcome as a measure of its performance. In contrast, the evaluation of biosensor effectiveness focuses on its ability to achieve high quality scans of target areas. The quality of scans is directly affected by the port placement. Therefore, surgical outcome is not a good metric for proper port placement. Instead, the area of coverage and probability of successful scans are better metrics for a biosensor application.

The automated system described in this chapter addresses restrictions in biosensor probe placement, such as the incident angle, as well as inadequacies of existing port placement

solutions. The system is capable of being used with any laparoscopic biosensor but was implemented with a Raman probe for the purposes of testing. The system allows the surgeon to select a region of tissue he wishes to scan within the patient's body, for which an optimized port location is computed. The system avoids unsafe port locations by avoiding collisions between the probe and anatomical structures. It also maximizes the performance of the biosensor by allowing proper orientation of the probe at the target location. Optimized port placement minimizes the risk to the patient while ensuring the most effective use of biosensor technology. This will enable a surgeon to make more informed and timely decisions during interventions.

3.2 Methods

The implementation of the system consists of two computer algorithms. One algorithm (the Reachable Point Algorithm) is used to determine points that are reachable from a given port location, and another (the algorithm for identifying the best port) is used to determine an optimal port location. A visualization interface has also been created to allow easier use of the system and interpretation of its results.

From a user's perspective, the system is designed to operate in the following manner. First, 3D models of a patient must be created (via segmentation) from medical imaging, e.g. CT or MRI scans. Next, areas of interest (biosensor scan locations) are chosen on the 3D models. Note that because the 3D coordinates of the two systems are the same, it is possible to select points of interest on the CT/MRI imaging. The system then determines an optimized port location based on the 3D information and the limitations of the biosensor (Figure 3-2).

Alternatively, the surgeon may select a port location, and the system determines all possible valid targets. This information is presented to the user in a virtual reality interface.

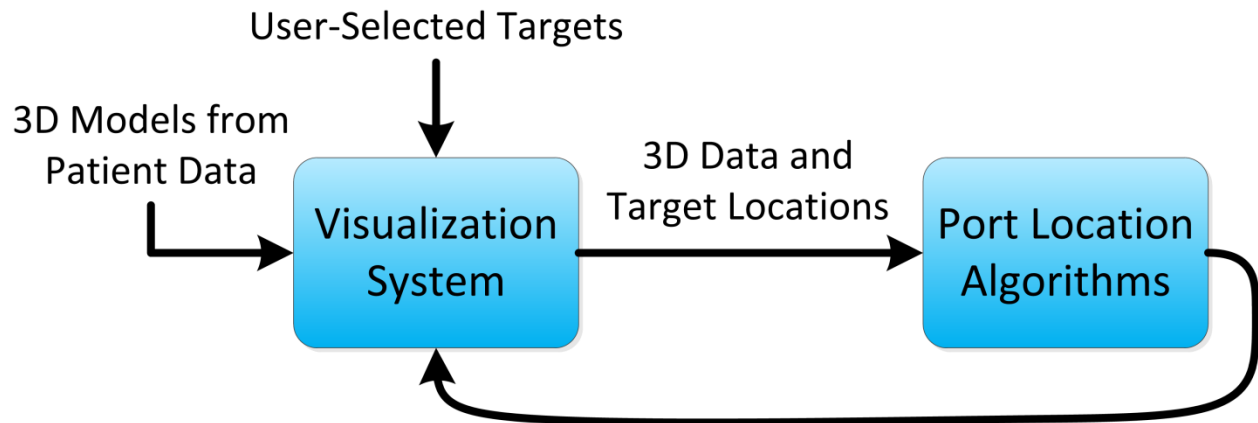


Figure 3-2: Data flow within the system

To prove the feasibility of the system, the implementation has been designed with respect to a Raman spectroscopy probe called the Process RamanProbe (InPhotonics, Norwood, MA). However, the system is intended to generalize to other types of biosensors. There are parameters and functions that can be changed in our algorithms to accommodate biosensors of different designs, such as probes of different dimensions or having angle-dependent response functions.

The Raman probe used in the design and validation of the system is a cylinder that is approximately 27 cm in length and 1 cm in diameter (Figure 3-3). It is non-flexible, and, like most optical sensors, the probe achieves the best scan when it is placed perpendicular to the tissue of interest.



Figure 3-3: Raman spectroscopy probe

The algorithms detailed in this section are designed to work with 3D representations (models) of patient data. These 3D models are made up of triangles, which are themselves defined by points. Each point in a 3D model has a corresponding normal vector that indicates a direction approximately perpendicular to the surface at that point. Specifically, the normal vector for each point is the average of the normal vectors for all triangles that share the point. Each point in the model can be considered a possible point for biosensor data capture, referred to as target points. Therefore, if a model has less detail (points), the algorithms will execute faster, but there will be a reduced number of targets a surgeon may choose to scan. The port

placement system supports whatever level of model detail is required by the surgical application or is possible within time constraints and computing power. If the provided models lack sufficient detail, a pre-processing stage can be used to increase the number of points.

A special “skin” model, which contains all potential port locations, must be defined. This model is thin (i.e. just the surface of the patient’s skin and not its thickness), which aids the collision detection algorithm (described in the following section). Each point in the skin model can be a possible port location. Thus, the model should be as detailed as necessary for an application.

3.2.1 Reachable Point Algorithm

An algorithm was created to test if a point is reachable from a given port location (Figure 3-5). The algorithm tests three critical criteria to determine if a point is reachable. If a point fails any test, it is determined to be unreachable. Thus, it is not subjected to any further tests, which shortens the execution time of the system. The three tests are described in the following subsections.

3.2.1.1 Biosensor Length Test

The first test is a simple biosensor length test, which ensures the biosensor is long enough to reach the target from the port location. If the target point is farther from a port location than the length of the biosensor, it is considered to be unreachable. This test is performed first because it is computationally the fastest and eliminates many unreachable targets. For some applications it may also be desirable to eliminate points that are too close to the port location. In this case, if the distance to the target from the port location is below some

defined threshold, the point is considered unreachable. In testing, this threshold was set at 10 mm.

3.2.1.2 Collision Test

The second test is a collision algorithm that ensures the biosensor does not collide with any other point while moving the probe towards the given target. The algorithm was designed to be extremely fast for the port placement application with a rigid probe. To handle a biosensor probe with a flexible or multi-jointed design, the algorithm could be modified. For example, if the probe had extra joints, the collision test could be done in separate stages (i.e. treating each link between the joints as a separate entity).

The first step of the collision test is to create a vector from the given port location point to the target point. In addition, vectors from the port location to all other geometry points (potential points of collision) are created (Figure 3-4).

The second step is to determine the distance from the port location to each of the potential points of collision. Any point that is farther away than the target point is eliminated as a point of collision, as the biosensor will never have to reach far enough to intersect with that point.

Any remaining potential collision points are now known to be closer to the port location than the target point. The third and final step determines if any of these points are within the radius of the biosensor. If the shortest distance between a potential collision point and the vector between the port location and the target point (representing the biosensor) is less than the radius of the biosensor, then the biosensor would collide with that point while trying to

reach the target point (see Equation 3-1 and Figure 3-4). If even a single collision is determined to occur, the target point is deemed unreachable.

$$x = \|v_2\| \sin(\arccos(\hat{v}_1 \cdot \hat{v}_2))$$

Equation 3-1

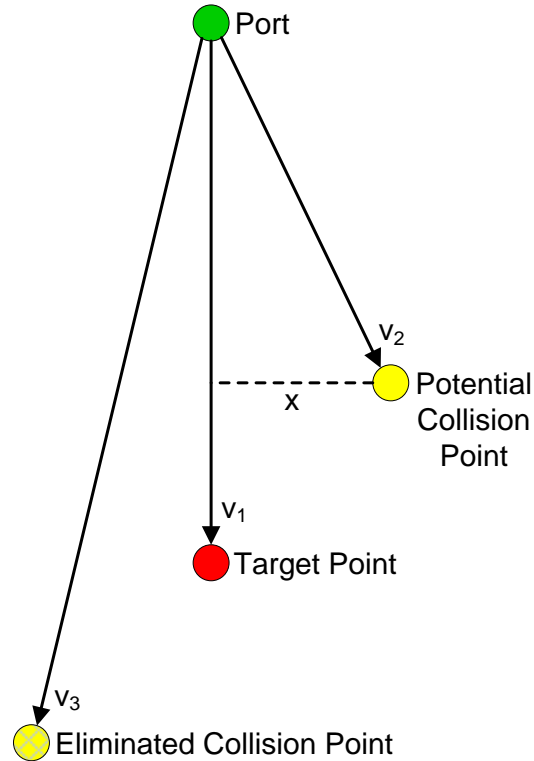


Figure 3-4: Diagram of the collision test algorithm. A collision occurs when $\|v_2\| < \|v_1\|$ and x is less than the radius of the biosensor.

3.2.1.3 Biosensor-Specific Scoring Function

The final test is a biosensor-specific scoring function. This test is used to determine the quality of a scan the biosensor will obtain from a given target. A score of zero is treated as a non-reachable point, while a score of one is considered a perfect scan. For our Raman probe, we used a relatively simple scoring function (Equation 3-2).

$$\text{Score} = \begin{cases} 1 - \frac{90^\circ - \theta}{45^\circ} & 45^\circ \leq \theta \leq 90^\circ \\ 0 & \text{Otherwise} \end{cases}$$

Equation 3-2

In Equation 3-2, θ represents the angular deviation of the probe to the tissue surface. The equation returns a 1 for a perfectly perpendicular orientation (θ equal to 90° from the surface) and decreases linearly to 0 as the probe approaches 45° from perpendicular. Although Raman biosensors are known to have a nonlinear response function [3], this linear equation reasonably approximates the same response. It was chosen for its simplicity and to illustrate the functionality of the port placement algorithm detailed below. Nonlinear functions or functions with angles other than 45° could be used to work with other biosensor probes.

Figure 3-5 shows the flow chart of the Reachable Point Algorithm. All target points are tested separately. First the biosensor length test is done because of its computation speed and ability to eliminate many target points as possibilities. A target point that passes this test is then checked with the collision test. If it is determined that the biosensor would not collide with any other points in reaching the target point, it is finally scored with the biosensor specific scoring function. If the point has a nonzero score after this test, it is deemed to be reachable.

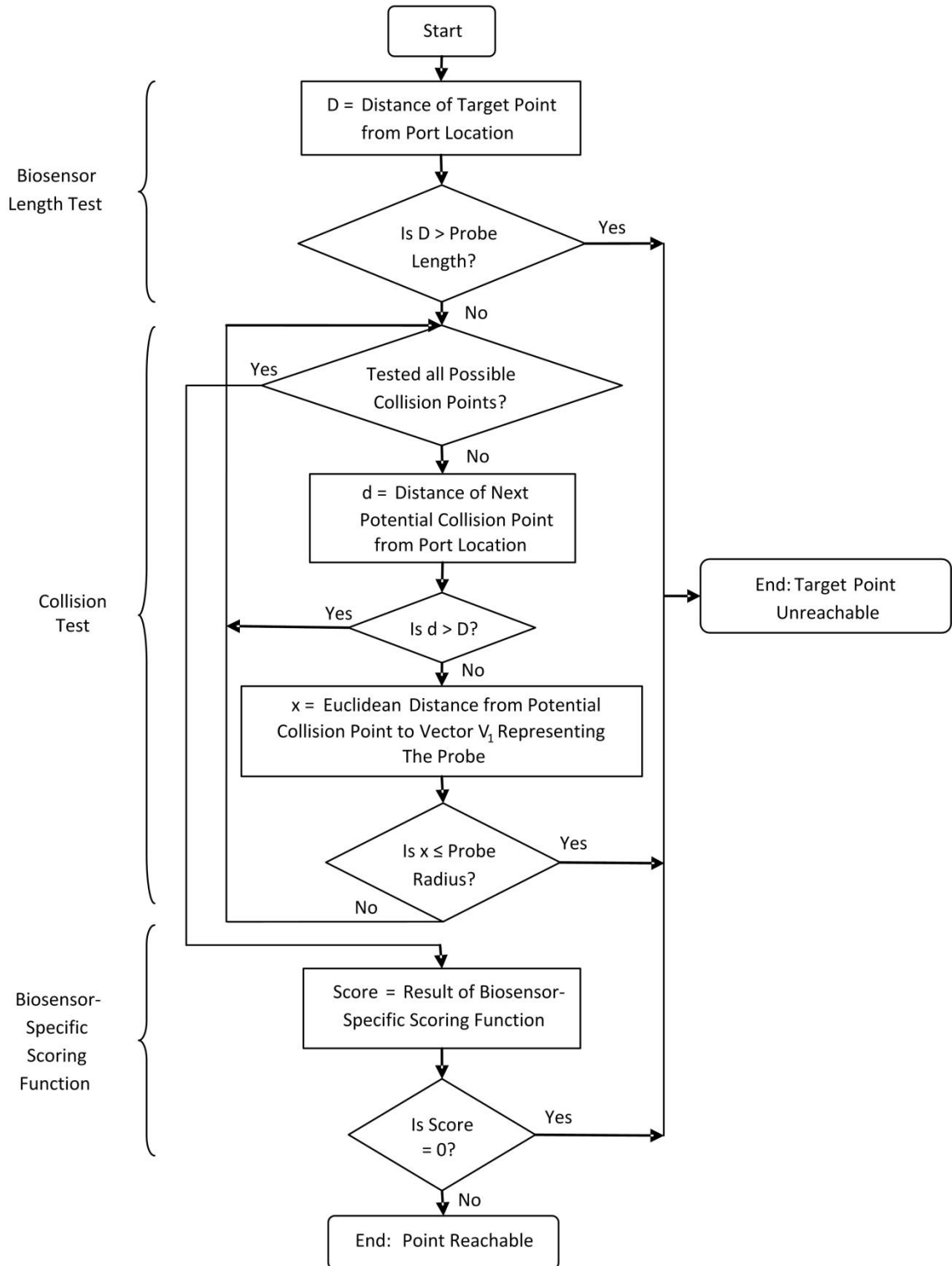


Figure 3-5: Flowchart of the Reachable Point Algorithm

3.2.2 Identifying the Best Port Location

The best port location is one that enables the best coverage of the target area by the biosensor. To find this location, the system evaluates each point in the skin model (or a user-selected subset of the skin) for its suitability as a port location (Figure 3-6). The evaluation of each skin point is carried out by executing the Reachable Point Algorithm with the skin point and all target points. This process provides the number or percentage of reachable target points and the average biosensor-specific score for each potential port location.

For the test application (Raman cancer detection), priority is given to the number of reachable points rather than to the biosensor-specific scoring function when determining the best port location. This is because it is critical to ensure that as many reachable points are scanned as possible, due to the importance of not leaving any cancerous cells behind during resection. Therefore, the best port location enables the maximum number of target points to be reached. If two or more port locations allow the same number of target points to be reached, the best port is chosen using the average result of the biosensor-specific scoring function. For example, if two ports can reach the same number of target points with a Raman biosensor, the port location that provides the smallest average angular deviation from perpendicular will be chosen.

It is possible that other biosensors may need a different priority or some combination of the scoring function and number/percentage of reachable points to determine a best port location. In this case, a weighted decision function could be used, allowing a combination of the number of reachable points and the scoring function to be used to determine which port is best.

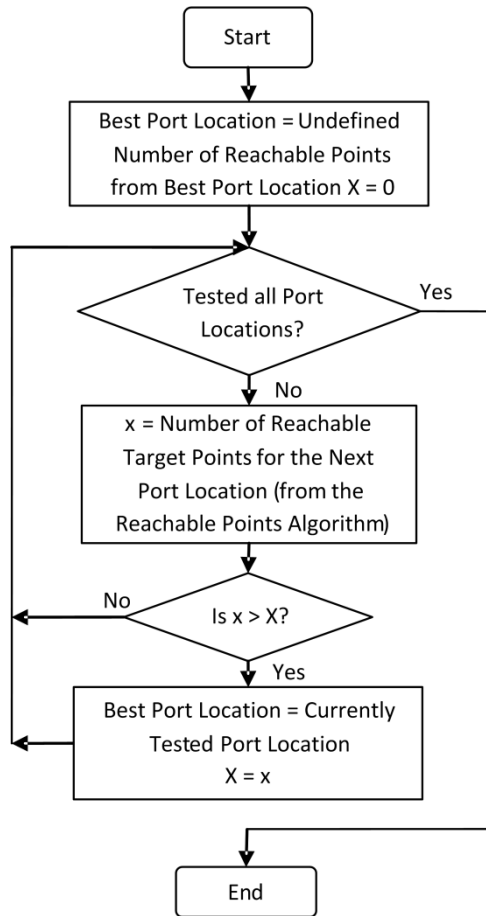


Figure 3-6: Flowchart for selection of best possible port location. This method is optimized for cancer detection using Raman spectroscopy (maximizing the number of reachable points). Other methods can be utilized as necessary.

3.2.3 Visualization

A 3D virtual reality display is used for the interface of the port placement system. It is based on 3D Slicer [51], an open source application for visualizing medical data. 3D Slicer displays the 3D models derived from segmentation as well as the various interface elements used by the system. To accommodate graphics and interactivity needed for the port placement application, a custom module was added to 3D Slicer. The module handles target area selection, port placement, and the presentation of the system's results.

Target area selection is carried out in the following fashion. First, the user selects a point in the center of a volume he wishes to scan, causing a "volume of interest" box to appear

around that point. The point selected belongs to a specific 3D model, therefore indicating which model is the target surface. Then the user adjusts the size of the box to enclose the desired target surface area. Once the region is finalized, small markers appear at each of the points that are both within the region and on the target surface (Figure 3-7). These points are considered to be the target points.

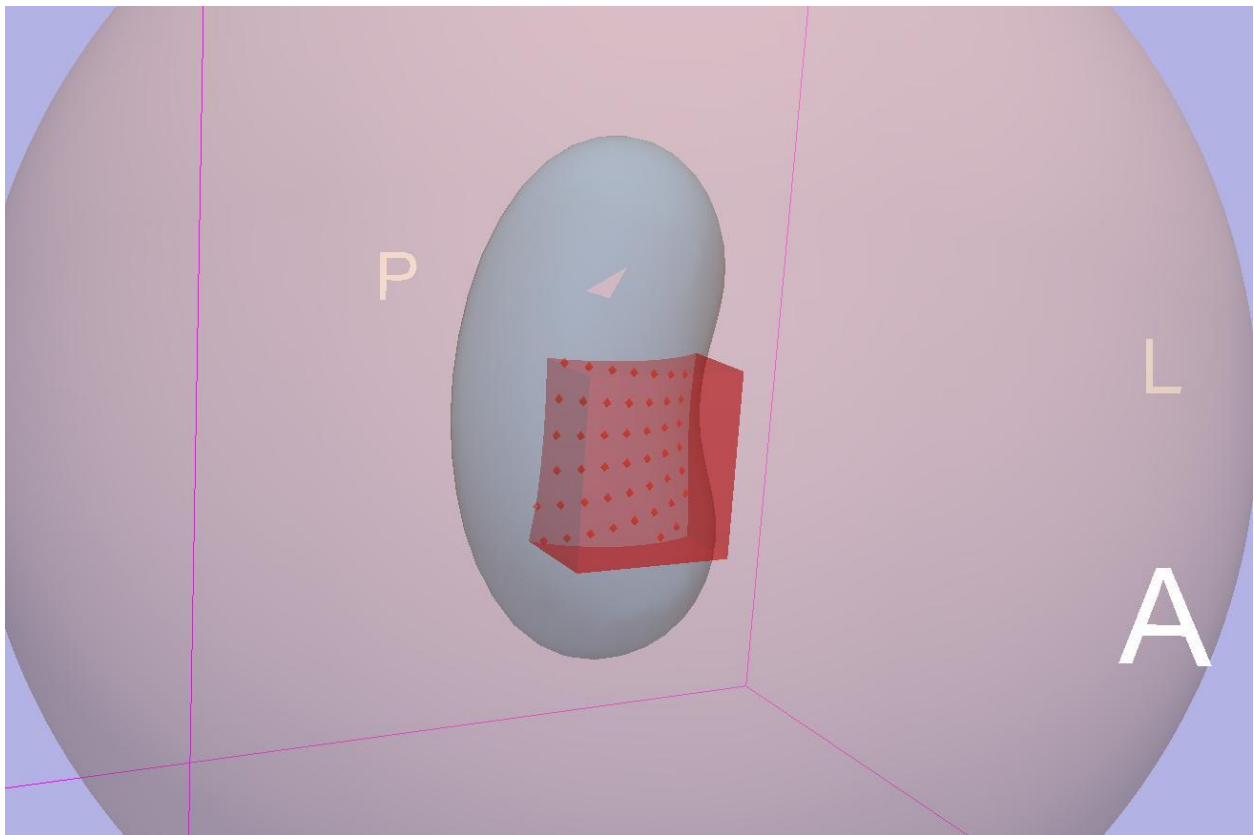


Figure 3-7: Target volume selection (red box) within the visualization system

Once the target points have been selected, the system can find an optimized port location. It can evaluate every point on the skin model, or the search can be restricted to a subset of the skin model. Selecting a subset of the skin model is accomplished in exactly the same fashion as choosing target points, consisting of a box being placed and the size adjusted.

The chosen subset of points is also highlighted with markers of a different color than the targets.

After the port placement algorithms are executed, a marker is placed at the optimized port location. This enables the user to see the port location relative to other body structures. In addition, a pop-up box displays the percentage of reachable points and the average biosensor-specific score for that location.

In addition to the computer-generated optimal port location, the user can choose a specific port location for the system to evaluate. This simply requires the user to click at a desired location on the skin model. If target points have been selected, the percentage of reachable points and average biosensor-specific score for the chosen port are calculated and presented. If a target region has not been selected, the system calculates all reachable points (points that pass all three tests within the Reachable Point Algorithm) from the chosen port. These points are highlighted with markers on the 3D models.

3.3 Results

To verify the operation of the port placement system, a number of test scenes were created. These scenes contained simple objects (planes, cylinders, etc.) with geometrically provable solutions for the optimal port locations. Using these scenes, the various components of the system were validated. It was shown that the algorithms are able to find optimal port locations, find all reachable target locations, and avoid collisions. Figure 3-8 demonstrates the test scenarios that were used to validate the system.

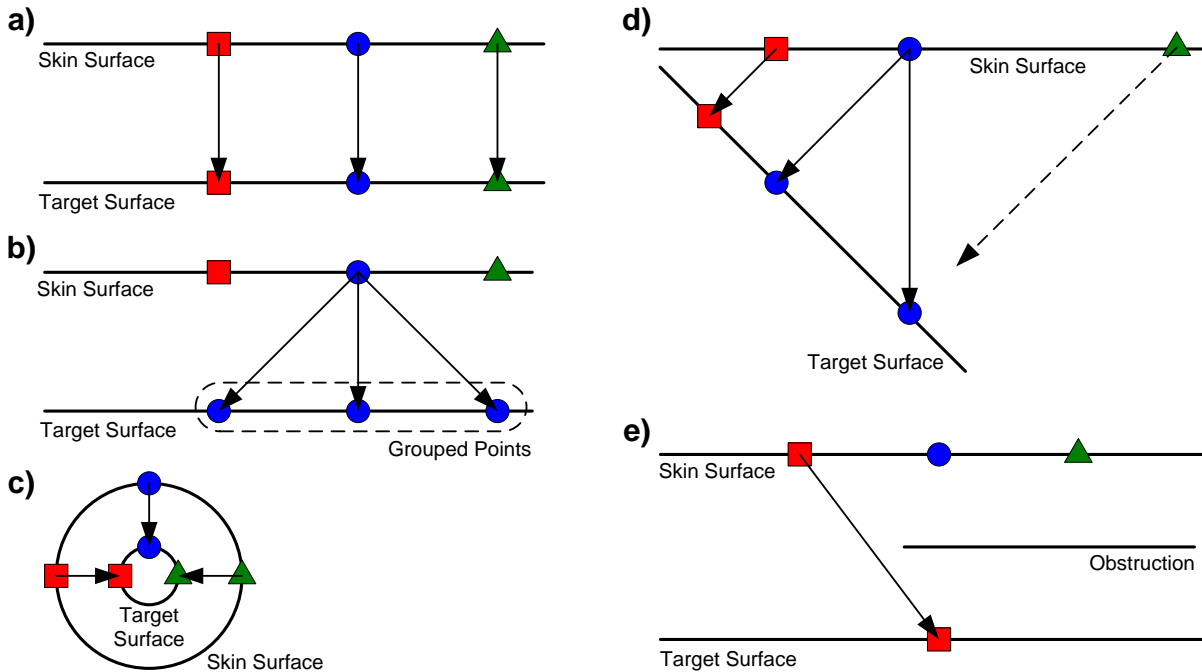


Figure 3-8: Cross-sectional views of five test scenarios used to validate the performance of the system

Part (a) in Figure 3-8 shows a cross-section of two parallel planes. The top plane represents the skin surface, whose points are potential port locations. The bottom plane is identical to the top plane but shifted downwards. It represents a target surface, whose points must be reached by the biosensor. In this scenario, the algorithms were executed with a single point selected at a time as the target. From the diagram, it is clear that the skin point directly above each target point is the best location for a port. This is because the approach vector from the skin surface to the target point is perpendicular to the target surface, which maximizes the Raman scoring function. This scenario was designed to verify that the system would function properly under very simple conditions.

The test scenario in part (b) is very similar to the one in part (a). The only difference is that the algorithms were executed with multiple points selected at a time as the targets. The

selected target points were always odd in quantity, centered below one of the skin points, and uniformly spaced. Under these constraints, the best port location is the skin point above the center of the group of target points. For any other skin point, the average value of the biosensor scoring function is lower because the average angle from the approach vector to the target surface at each target point is further from perpendicular. The purpose of this scenario was to validate the system's operation when multiple target points are selected.

Part (c) shows a cross-section of two concentric cylinders. The outer cylinder represents the skin surface, and the inner cylinder represents the target surface. The cylinders are made from the same model with the same points, but they were scaled to different radii. The algorithms were executed with a single point selected at a time as the target. As in test scenario (a), the best port location for each target point is the skin point directly across from it. This test was used to verify that the system would work with non-planar (curved) surfaces.

In part (d), there is another cross-section of two planes. The top and bottom planes represent the skin and target surfaces, respectively. In this scenario, the algorithms were executed with a single point selected at a time as the target. Because of the angle between the two planes (45°), the best port location for a given target point is not directly above the target point. Instead, the best port location, which maximizes the biosensor scoring function, is more to the right of the target point. This is because the approach vector and target surface at the target point are perpendicular for the skin point on the right. However, there is an exception for the rightmost target point. The distance from this point to the green triangle point on the skin surface was made to be greater than the length of the biosensor probe. Thus, the green triangle point was not a valid port location. The blue circle point of the skin surface enables the

biosensor probe to reach the target and achieves an angle closest to perpendicular, so it is the best port location. Therefore, this test scenario verifies the system's performance when the skin and target surfaces are not parallel and when a target point exceeds the length of the biosensor probe.

Part (e) shows a test scenario that is very similar to the one in part (a). The same parallel skin and target surfaces are used, but there is an obstruction placed between them. The single target point is only accessible from the leftmost skin point. This test demonstrates that the system works by avoiding collisions when obstructions are present.

These test scenarios show that the Reachable Point Algorithm and the algorithm for identifying the best location work as intended. Since finding all reachable points from a given port location is merely an application of the Reachable Point Algorithm, the results demonstrate that this function of the port placement system also works correctly.

More complicated scenes containing a skin model and several enclosed organs were constructed to demonstrate the system's operation. Due to the scene's complexity, geometric verification of the results was mathematically intractable. Target areas were selected on one of the models, and the system was used to determine an optimized port location (Figure 3-9). In addition, multiple port locations were selected manually and scored to verify that the system-selected port location had a better score. During these tests, it was found that the optimized port location for a typical scene can be calculated in only a few minutes on a modern PC.

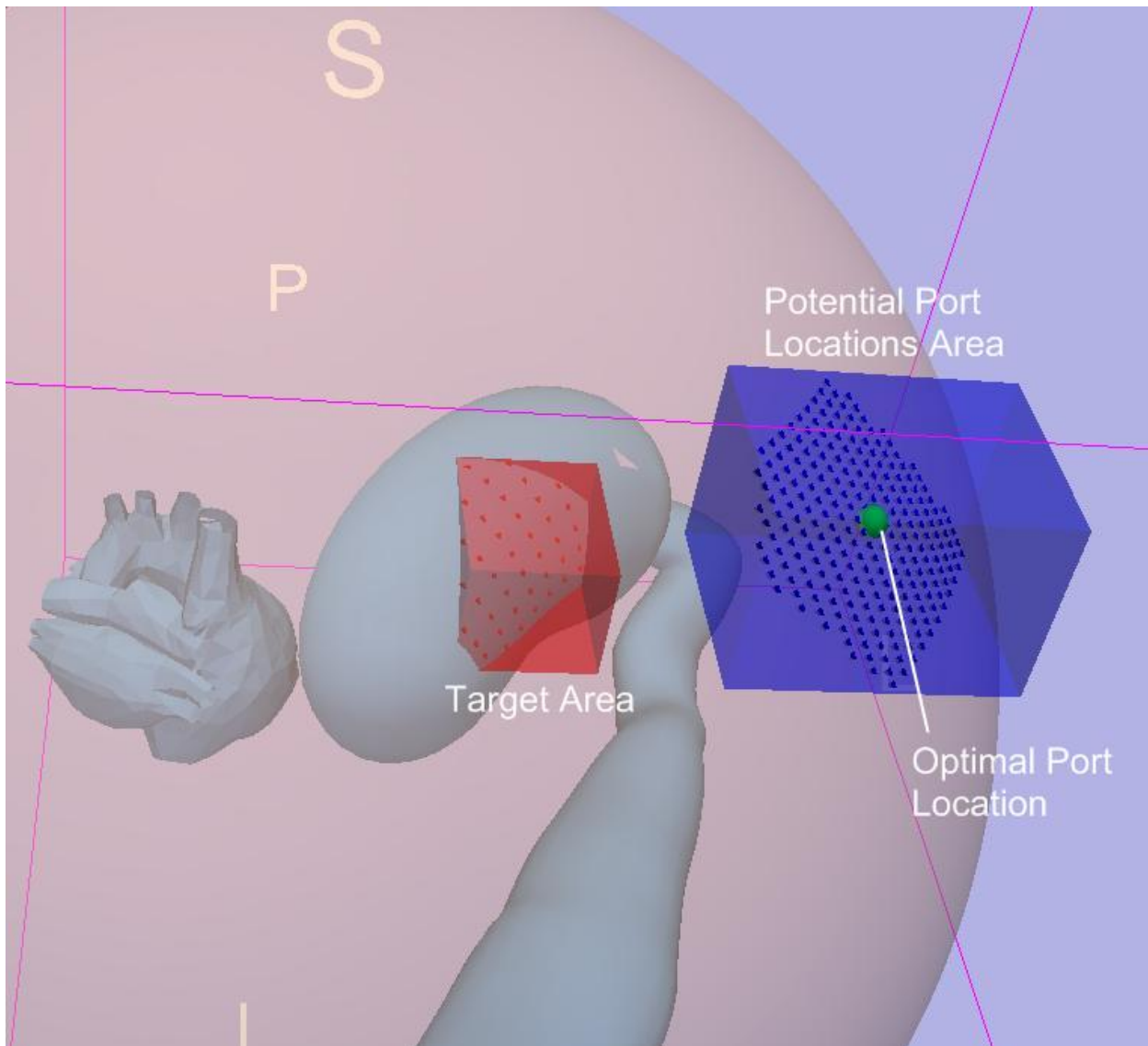


Figure 3-9: Port placement within the visualization system. The blue box encloses potential port locations, with the green dot indicating the optimal location for use with the enclosed red target area.

We also demonstrated the ability of the system to find all possible reachable points from a given port location in a complex scene. As expected, the system avoided points where collisions would occur and indicated only those points that were reachable according to the scoring function. The visualization of these results is shown in Figure 3-10.

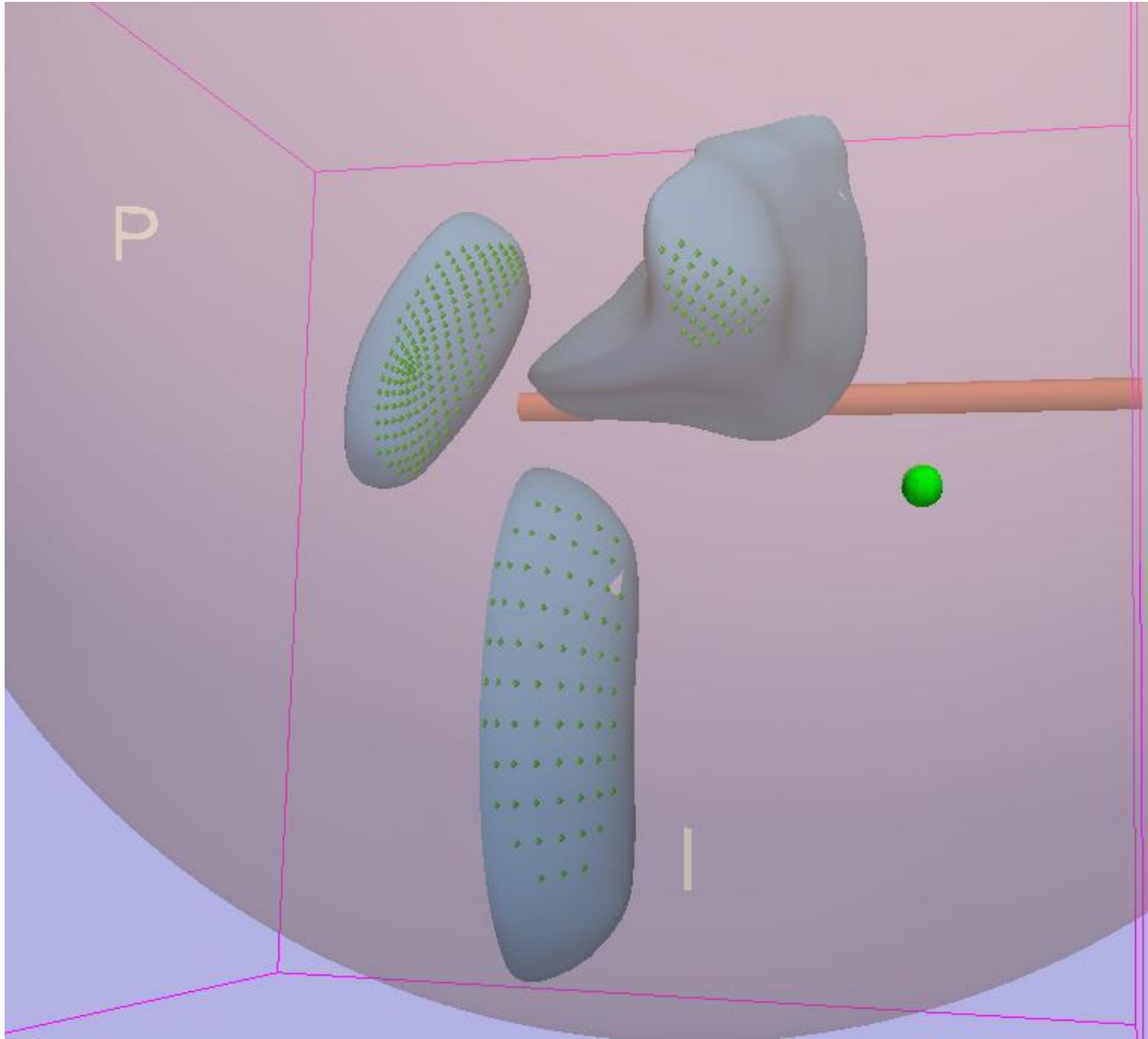


Figure 3-10: Visualization system showing all points reachable (green markers) by the biosensor from the manually selected port location (green dot)

3.4 Discussion

Biosensors and medical robotics used *in vivo* hold the potential to rapidly identify and treat disease. Biosensors have strict physical limitations that make picking a port location a non-trivial task for a human operator. In addition, current techniques developed for automated port placement are designed for laparoscopic surgical instruments. This work demonstrates a novel automated technique for selecting port locations specifically for biosensor applications.

Using existing patient 3D modeling techniques, it is able to find a proper location using user specified targets in a matter of seconds.

The technique described in this chapter does have a few limitations. One limitation is that it assumes all structures are rigid (non-deformable). This limitation is a consequence of the complexity of tissue deformation models. Furthermore, the system also assumes that body structures do not move as a result of insufflation, manipulation, respiration, etc. Consequently, CT and MRI scans should be in the same pose as the surgery. Additional algorithms would be needed to accommodate tissue deformation and movement. This is an ongoing area of research [52, 53].

Another limitation exists within the collision algorithm. There is the possibility of missed collisions with very large triangles within the 3D models. Since this method tests for collisions at the points of the triangle, it is possible for the vector representing the biosensor to pass through the middle of a large triangle (Figure 3-11). This is possible if each point of the triangle resides outside the radius of the biosensor. In this case a collision should obviously occur, but will go undetected. This possibility can be eliminated with a pre-processing stage that ensures the 3D models have none of these triangles. This pre-processing stage would test each triangle in the scene and perform triangle subdivision if any triangle is determined to be too large [54].

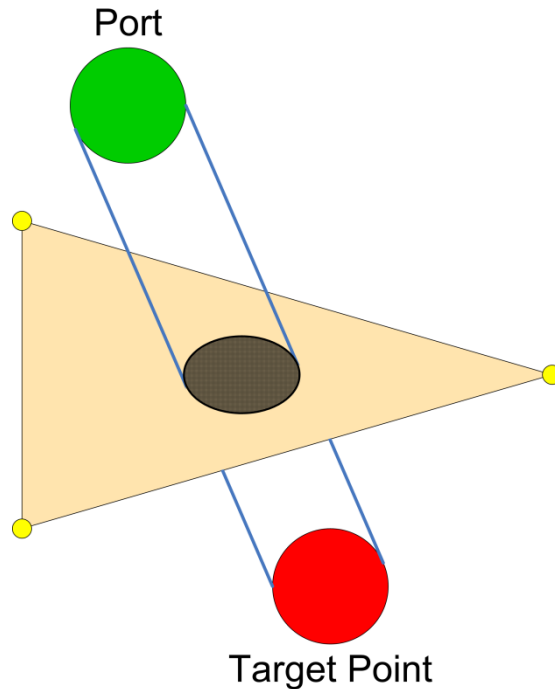


Figure 3-11: Example of a collision that would be undetected due to wide triangle point spacing. This problem can be prevented with a pre-processing stage.

Currently the execution speed of this applications is acceptable for offline, pre-surgery processing. However, there are many possible solutions for speed increases. The highly parallel nature of this task makes it a prime candidate for multithreading and parallel processing. Other opportunities for speed increases include faster processors and more efficient algorithm implementations. These performance increases may allow for near real-time results. If near real-time performance can be achieved, intraoperative medical imaging technology (e.g. 3D ultrasound) could be used to update tissue models and reachable points during a procedure.

Currently this work uses a Raman probe for prototyping the algorithms. However, the system can handle any other biosensor that can be used laparoscopically. To support biosensors of different physical dimensions, modifications can be made to the parameters used in the collision algorithms, such as probe radius and length. Flexible probes can be supported

by creating a 3D model of the probe and performing traditional collision detection [55]. Other types of biosensors (besides Raman spectroscopic probes) can be supported with different scoring functions that are developed to accommodate their different physical data capture characteristics. For example, ultrasound probes require a more direct angle of approach in order to image the tissue of the target. In this case Equation 3-2 could be modified to use a more restrictive angle, such as 80° , instead of 45° . Other biosensors, such as many compound detection sensors, only need to touch the target, in which case angle of contact has no effect. In this case, the biosensor-specific scoring function would simply not be used.

In conclusion, this chapter presented the implementation, testing, and verification of an automated port placement system for *in vivo* biosensors. The port placement system provides a new way of determining the best port location for biosensor applications. The port placement system also includes scoring for user-selected ports. This scoring system is used for the analysis of human performance in the task of port placement, which is the topic of the next chapter.

CHAPTER 4: HUMAN PERFORMANCE IN THE TASK OF PORT PLACEMENT

The automated port placement system described in Chapter 3: includes the ability to score user-selected ports for given test scenes. In this chapter, we investigate human performance in the task of port placement across a variety of scenarios. Using the automated port placement system's evaluation methods, we grade user-specified placement. Such an evaluation has never been done before because biosensor use has not been prevalent in surgery and no grading system was available for this type of port placement task. The information gathered from these tests will give us insight into human performance in the task of port placement for Raman and other similar biosensors. This will help in the development of training options to improve human performance. In addition, the results will help improve future automated systems to better augment human performance. We believe this will make the use of biosensors more feasible in the operating room.

4.1 Methods

4.1.1 Participants

This study was approved by the Human Investigation Committee at Wayne State University. Informed consent was obtained from each participant. A sample of 20 participants was chosen for testing without exclusion criteria corresponding to adult age, gender, or expertise. Fourteen participants were under the age of 30, four were women, and two were surgeons. No participant had any previous training or experience with the tests being conducted, so their backgrounds had minimal influence on their performance.

4.1.2 Apparatus

Tests were performed on a laptop computer running 3D Slicer [51]. 3D Slicer was modified to incorporate the port placement algorithms described in Chapter 3: . In addition, functions were added to collect data such as the chosen port location during the testing. 3D test scenes were created, which consisted of individual 3D models representing different organs and bodily structures. The user interface consisted of a computer mouse that was used by the participants to choose a location in 3D space on the presented 3D scene.

4.1.3 Experimental Task

Fifty tests were designed to mimic the requirements of biosensor port placement during surgery. They were developed with a specific biosensor in mind: a Raman spectrometer probe.

Each test scene consisted of 3D models representing the skin, target organs, and the dimensions of a Raman probe (as a size reference). Rather than using complete scans of actual patients, the scenes were built from smaller sets of simpler 3D models. We didn't use actual patient data because we didn't want the subjects to be overly reliant on their medical knowledge. Moreover, actual patient data would not have given us control over specific dimensions of task difficulty.

Red markers were placed on the target organs to indicate points of interest that should be scanned with the Raman spectrometer (Figure 4-1). Across all 50 test scenes, there were a minimum of 9, a median of 54, and a maximum of 826 target points to scan from the selected port location.

The participants were instructed to pick a desired port location on the skin using the mouse pointer. They were directed to choose a port location that would maximize the number

of target points reachable with a virtual Raman probe. In addition, the participants were told about the limiting factors used by the port placement system to determine if an individual target point is reachable. These factors are described below. The participants used the mouse to rotate, zoom, and pan the virtual scene as desired, and they indicated their decision for the port location by pressing a button on a keyboard.

There are three factors evaluated by the port placement system to determine if a target point is reachable. These are the same as the three tests described in section 3.2.1 and briefly described here for clarity. First, the ability of the virtual probe to reach the target point from the port location (via a straight line) is calculated. In other words, it is determined if the probe has sufficient length. Second, a collision detection algorithm is executed to verify the absence of any obstructions between the target point and the port location using the dimensions of the Raman probe. Finally, an algorithm calculates the angle of incidence of the biosensor from the target surface (at the target point) to determine if the angle is within 45° of perpendicular. This constraint was chosen to imitate the characteristics of a real Raman probe, which can experience compromised data acquisition beyond this angle. If a target point passes all three tests, it is considered reachable.

Test scenes were created without regard to the number of target points that are actually reachable. Thus, participants did not know if it was possible to reach every target point or only a subset of them. We used our automated port placement system to find an optimized port location for each test scene. As expected, the port placement system did not always reach 100% of the target points within the tolerance of the criteria for an allowable scan. Therefore,

the number of points the port placement system reached was used to represent the maximum number of points reachable in each test scene.

4.1.4 Trial-Level Procedure

Each participant had to go through all 50 test scenes. The tests were presented in a random order with one test shown at a time. Once a participant chose a port location, the next test was presented immediately. No feedback was given to the participant as to the quality of his performance. This was done to minimize learning effects throughout the study. The execution of one test by a participant was considered to be one trial.

4.1.5 Experimental Design

The 50 tests were divided into five sections, with ten tests in each section. Each section was designed to test a specific condition related to the task of port placement. These specific conditions were decided upon during a discussion with a surgeon. The surgeon was asked what types of conditions would present difficulties when trying to laparoscopically position a biosensor to scan target tissues. The surgeon indicated four conditions in which biosensor sampling would be impeded due to improper port placement. Four sections of the study were derived from these problem conditions. A fifth section with no significant impediments was added as a control case. These test sections are described in greater detail below.

The first section of ten tests served as a baseline/control condition; it was designed to be simple. In this type of scenario, the skin surface and target surfaces were smooth or flat, and the line from the ideal port location to the target surface was roughly orthogonal to the target surface. The number of target points was small, and they were clustered close together. Figure 4-1 shows an example from this section.

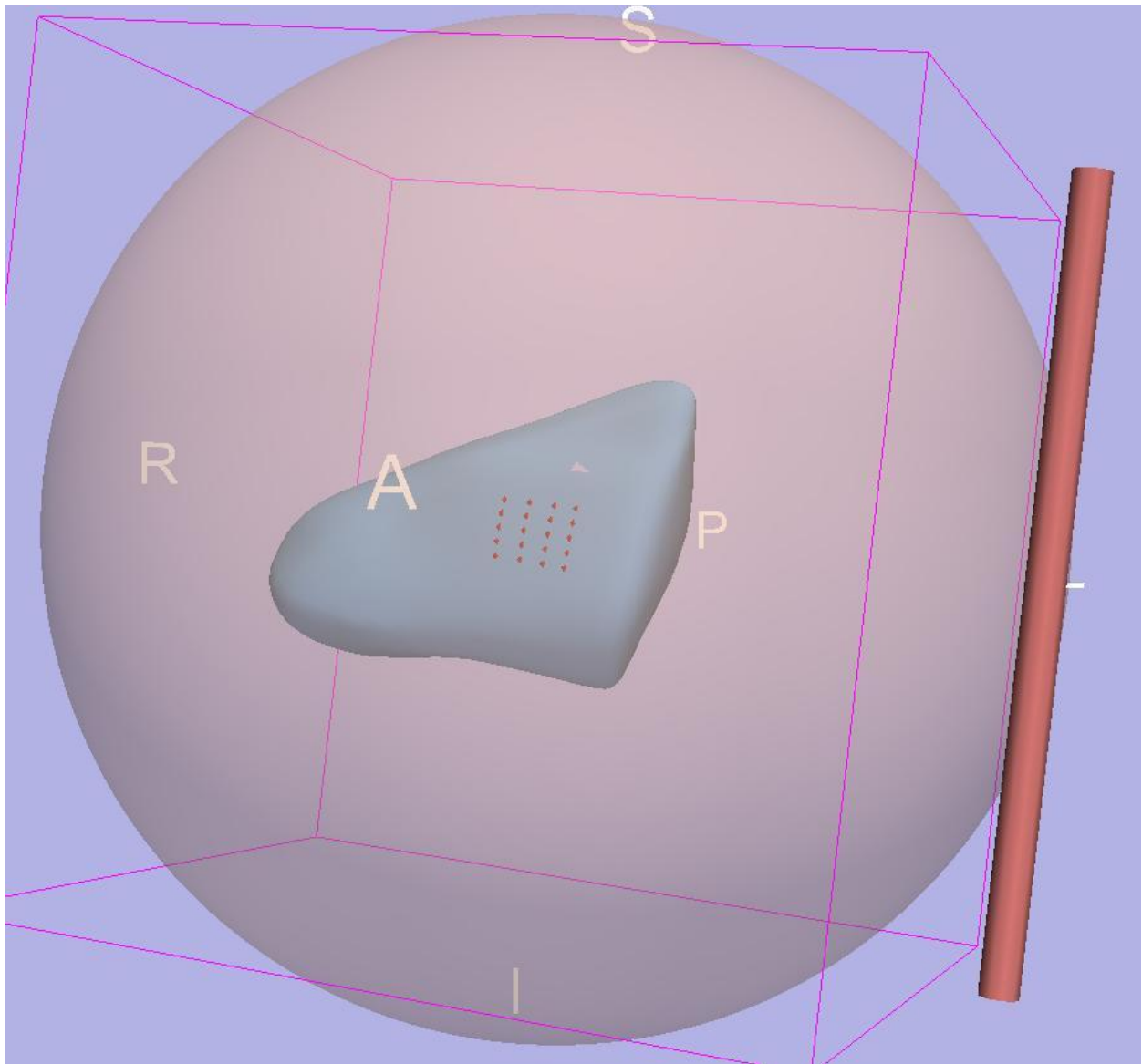


Figure 4-1: Example test scene from section 1. The pink sphere is the skin surface, and the enclosed blue model provides the target surface. The red dots represent target points. The red cylinder is a representation of the Raman probe, which provides a reference for scale. The letters are used by 3D Slicer to provide information about the current viewpoint (right, anterior, posterior, etc.).

The second section of tests focused on complex target surfaces. In this type of scenario, the skin surface was smooth, but the target surfaces were bumpy or contained complex angles and grooves. The target points remained relatively few in number and clustered close together. Figure 4-2 shows an example from this section.

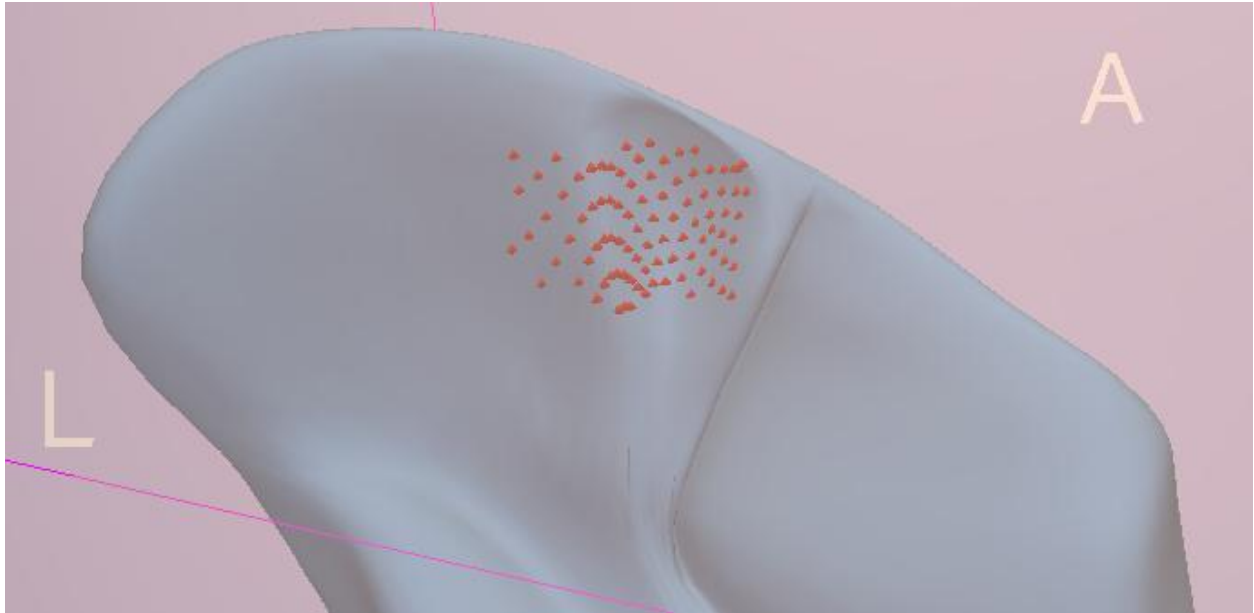


Figure 4-2: Close-up view of a section 2 test scene that demonstrates a complex target surface

The third section of tests focused on the size of the target surface. In this type of scenario, the skin surface and target surfaces were smooth. The number of target points was large, and there were some cases in which groups of target points were separated by distance from each other. Figure 4-3 shows an example from this section.

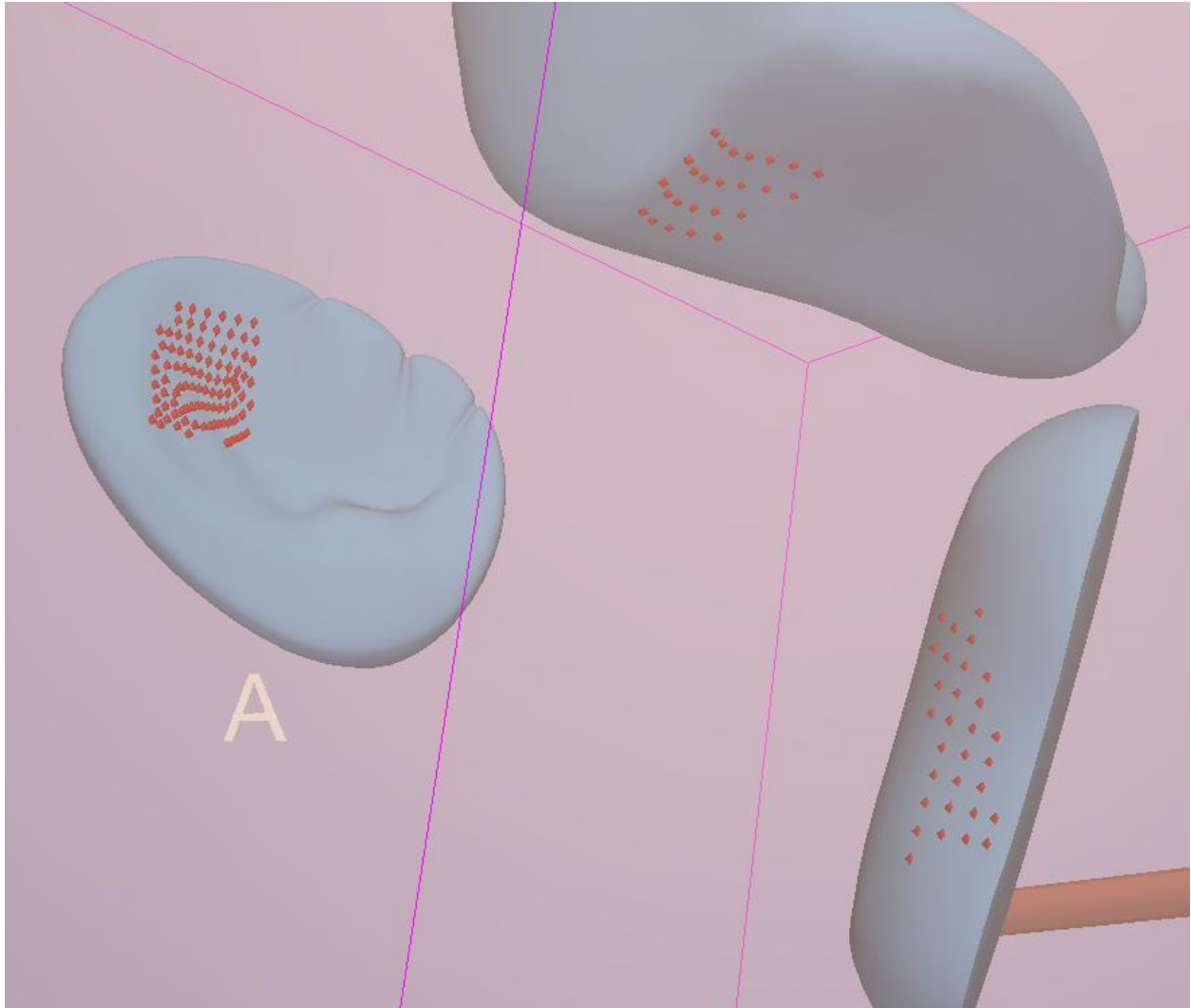


Figure 4-3: Close-up view of a section 3 test scene that demonstrates large target surface area

The fourth section of tests focused on the complexity of the skin surface. In this type of scenario, target surfaces were smooth, but the skin surface was bumpy or contained complex angles and grooves. The number of target points was relatively small, and they were clustered close together. Figure 4-4 shows an example from this section.



Figure 4-4: Close-up view of a section 4 test scene that demonstrates a complex skin surface

The final section of tests focused on obstructions. In this section, the skin surface and target surfaces were smooth. The number of target points was small, and they were clustered close together. However, additional surfaces were placed in positions that would obstruct the placement of the port. Figure 4-5 shows an example from this section.

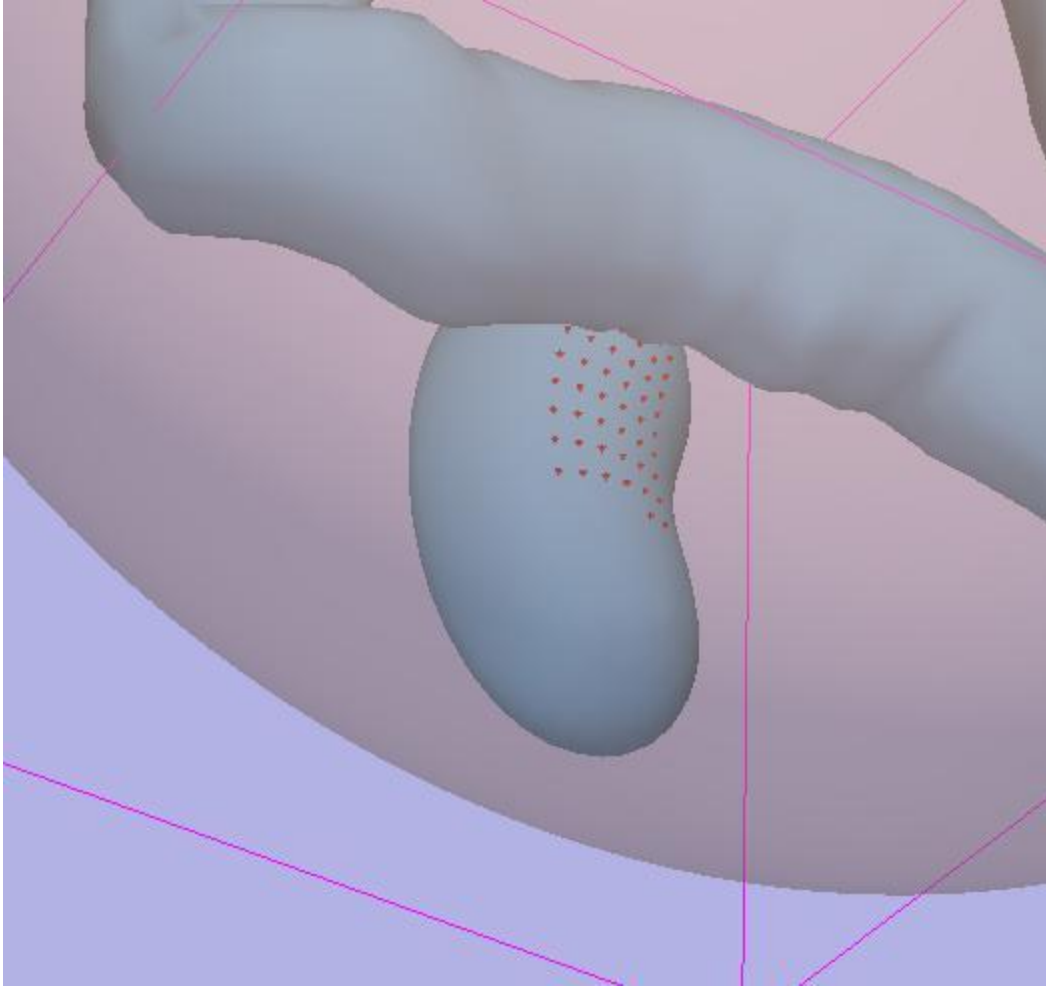


Figure 4-5: Close-up view of a section 5 test scene that demonstrates an obstruction

Each participant was presented each test once. The trials were analyzed independently, and the performances of different participants served as replicates of the experiment for statistical analysis. The time for each test was not considered. The only data collected during testing was the set of Cartesian coordinates (x, y, z) of the port location chosen by the participant for each test.

Although there were no time constraints placed upon the subjects during the testing, the tests were designed to be completed in about 30–45 minutes. Since only a mouse and keyboard had to be used during the tests, no physical exertion was required. Since there were

no time constraints or performance requirements, little mental stress was placed upon the participants. Consequently, fatigue was not found to be an issue during the testing.

Post-processing was done using the port placement system's evaluation methods. Participants were given a score for each test that was equal to the number of target points reachable with the virtual Raman probe from the participant's chosen port location. An individual target point was considered reachable if the three criteria described in the Experimental Task section were met.

From the score (the number of reachable target points) each participant achieved for each test scene, two percentages were calculated. The first is the participant's score divided by the maximum number of reachable target points, or the percentage of maximum (PoM). As stated before, the maximum number of reachable target points was determined using the port placement system. The second is the participant's score divided by the total number of target points present in the scene, or the percentage of total (PoT).

It is important to obtain a measure of the difficulty of each of the five test sections. To calculate this, we obtained the average of the PoMs for all participants in all tests of each test section. PoM was used because it utilizes the port placement system's score as the maximum number of points. This normalizes the results among scenes that have different amounts of reachable target points.

4.2 Results

We used the average of the PoMs to compare the different scenarios to each other based on difficulty in order to provide an indication of the types of scenarios in which human

performance suffers. Figure 4-6 shows the averages obtained and the 95% confidence interval for each test section.

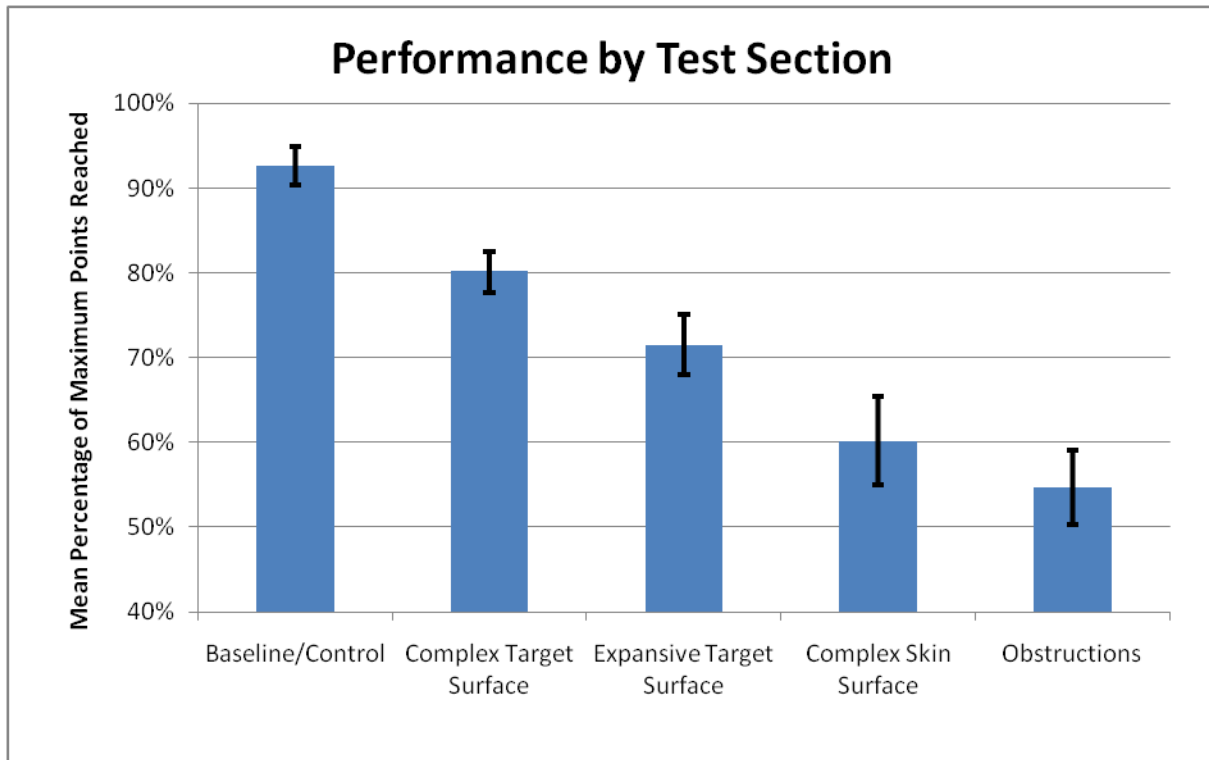


Figure 4-6: Average percentage of maximum (PoM) points reached for each test section. The black vertical lines represent the 95% confidence interval about each mean.

The participants' average PoMs across all scenes ranged from 57% to 78%. Confidence intervals of the mean PoMs were calculated for all participants, and inspection of the interval plots did not reveal any outlying participants. Figure 4-7 shows the average PoM and 95% confidence interval for each participant.

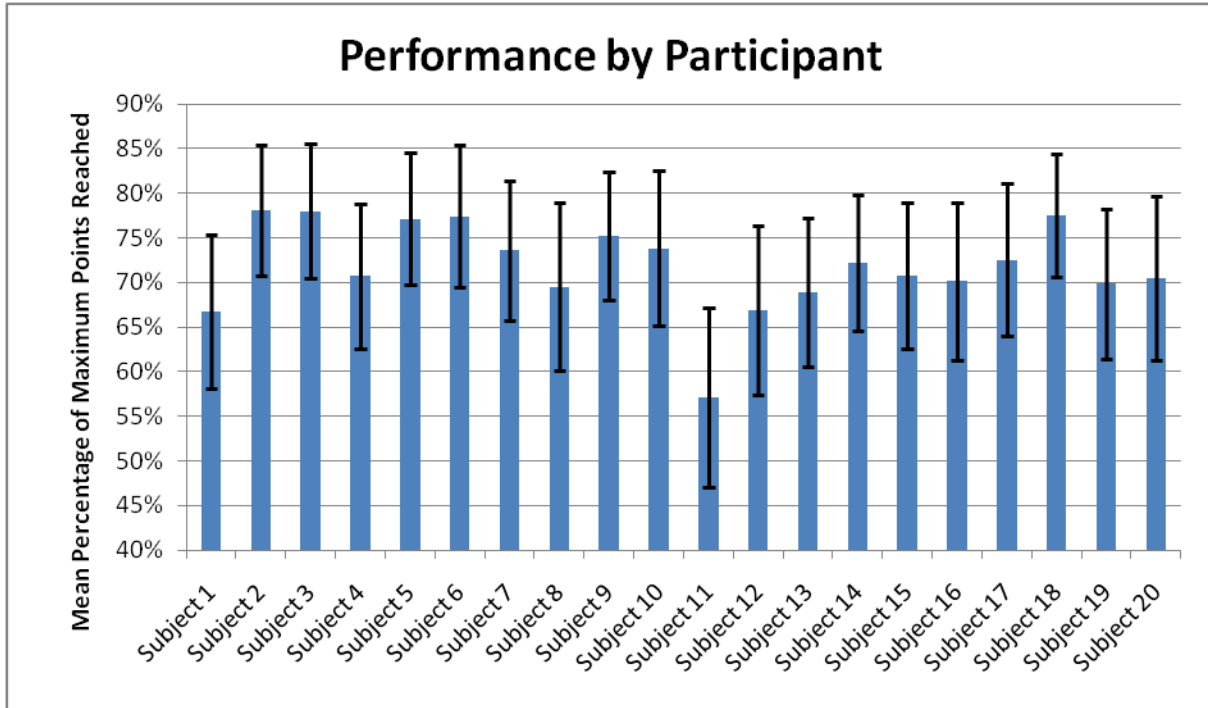


Figure 4-7: Average percentage of maximum (PoM) points reached for each participant over all test scenes. The black vertical lines represent the 95% confidence interval about each mean.

In addition, it is also important to investigate performance on a scene-by-scene basis. This provides an opportunity to find scenes in which the difference between the average participant performance and the computer algorithm's performance is greater than other scenes in the same test section. These outlying scenes can help us understand specific scenarios in which performance is degraded. To calculate this, we obtained the average of the PoTs for all participants for each scene. PoT was used in this case to better compare the performances of the port placer system and the participants. The following graphs display the results of the calculations, with one graph per test section. For clarity, the graphs' contents are sorted by ascending computer algorithm performance.

The baseline/control section represented the first type of scene. As shown in Figure 4-8, average participant performance ranged from 0% to 19% less than the computer's results. This was expected because these tests were the easiest.

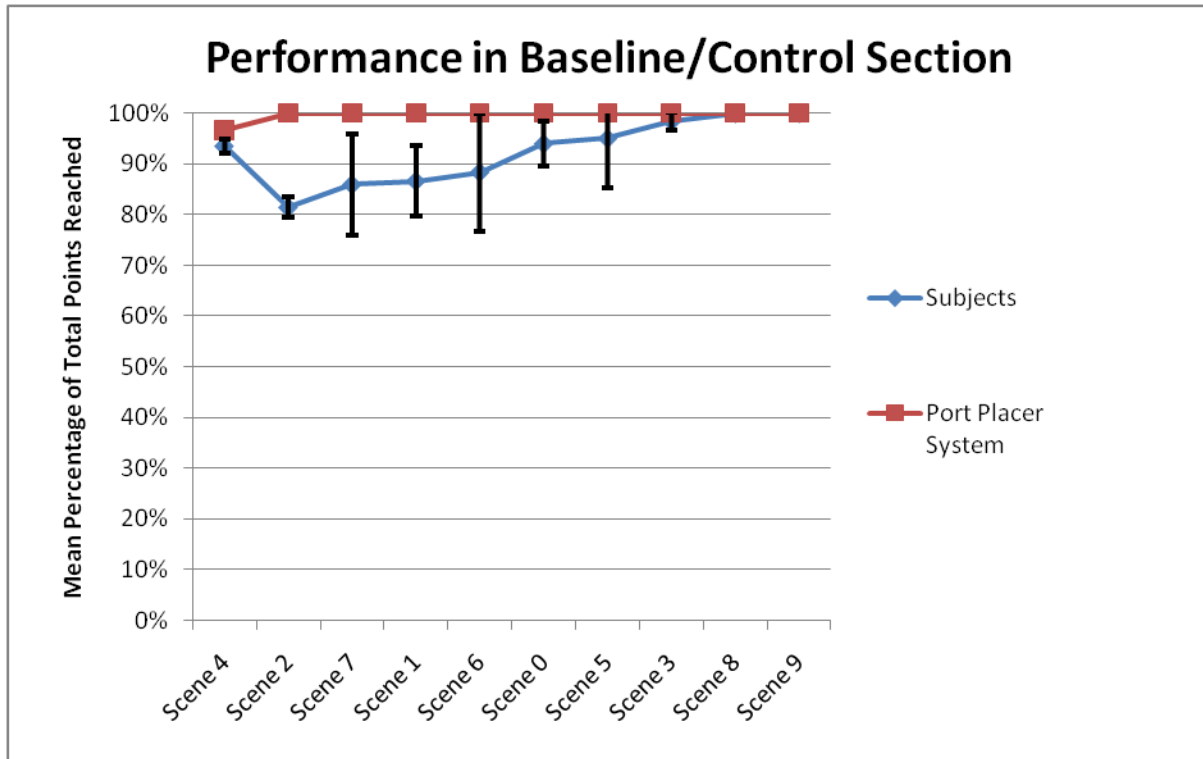


Figure 4-8: Performance for the baseline/control section. Squares represent the port placer system's performance, while diamonds represent the average participant performance. The black vertical lines represent the 95% confidence interval about each mean.

The complex target surface section represented the second type of scene. As shown in Figure 4-9, average participant performance ranged from 6% to 25% less than the port placer system's results.

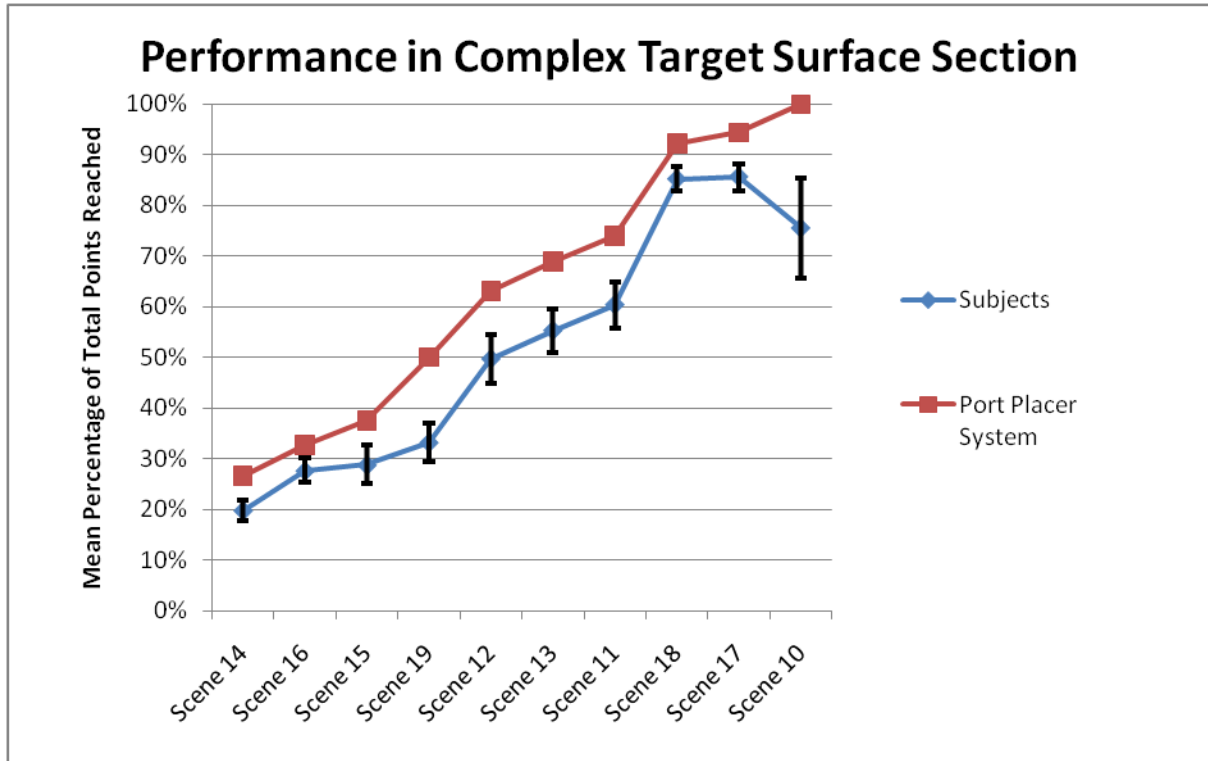


Figure 4-9: Performance for the complex target surface section. Squares represent the port placer system's performance, while diamonds represent the average participant performance. The black vertical lines represent the 95% confidence interval about each mean.

The expansive target surface section represented the third type of scene. As shown in Figure 4-10, average participant performance ranged from 6% to 35% less than the computer's results.

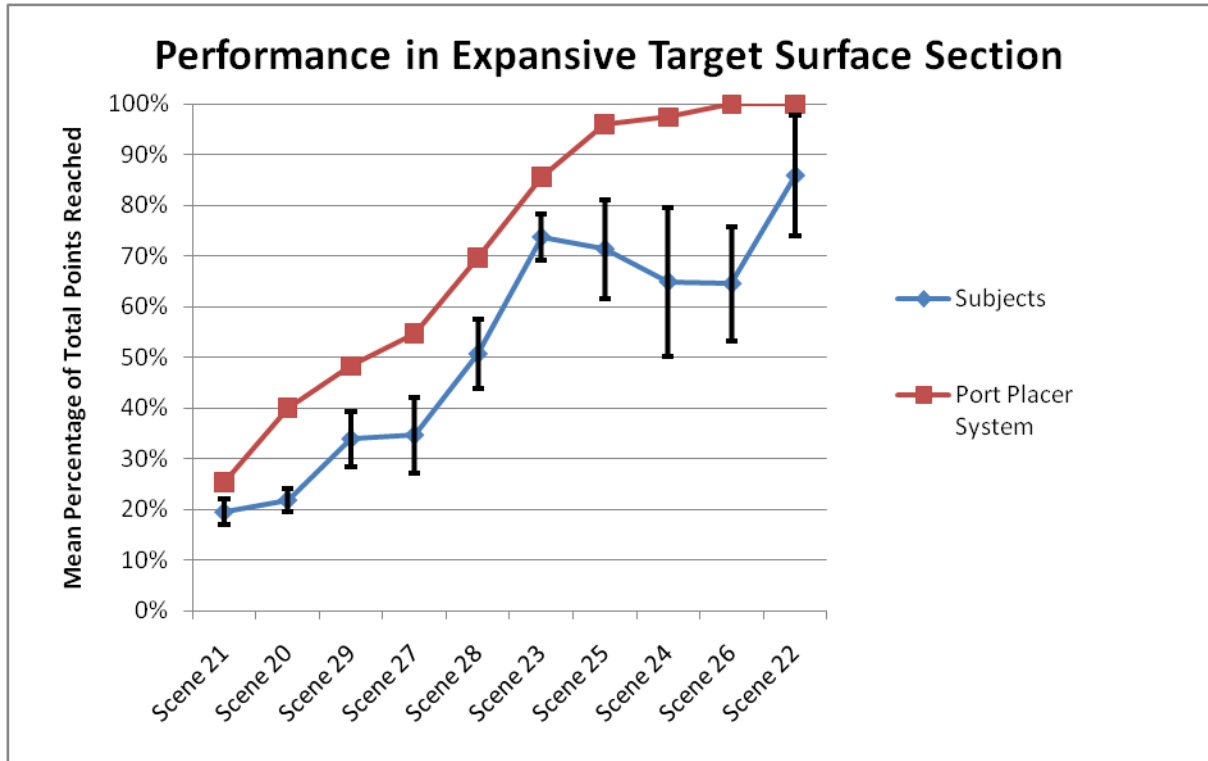


Figure 4-10: Performance for the expansive target surface section. Squares represent the port placer system's performance, while diamonds represent the average participant performance. The black vertical lines represent the 95% confidence interval about each mean.

The complex skin surface section represented the fourth type of scene. As shown in Figure 4-11, average participant performance ranged from 0% to 93% less than the port placer system's results.

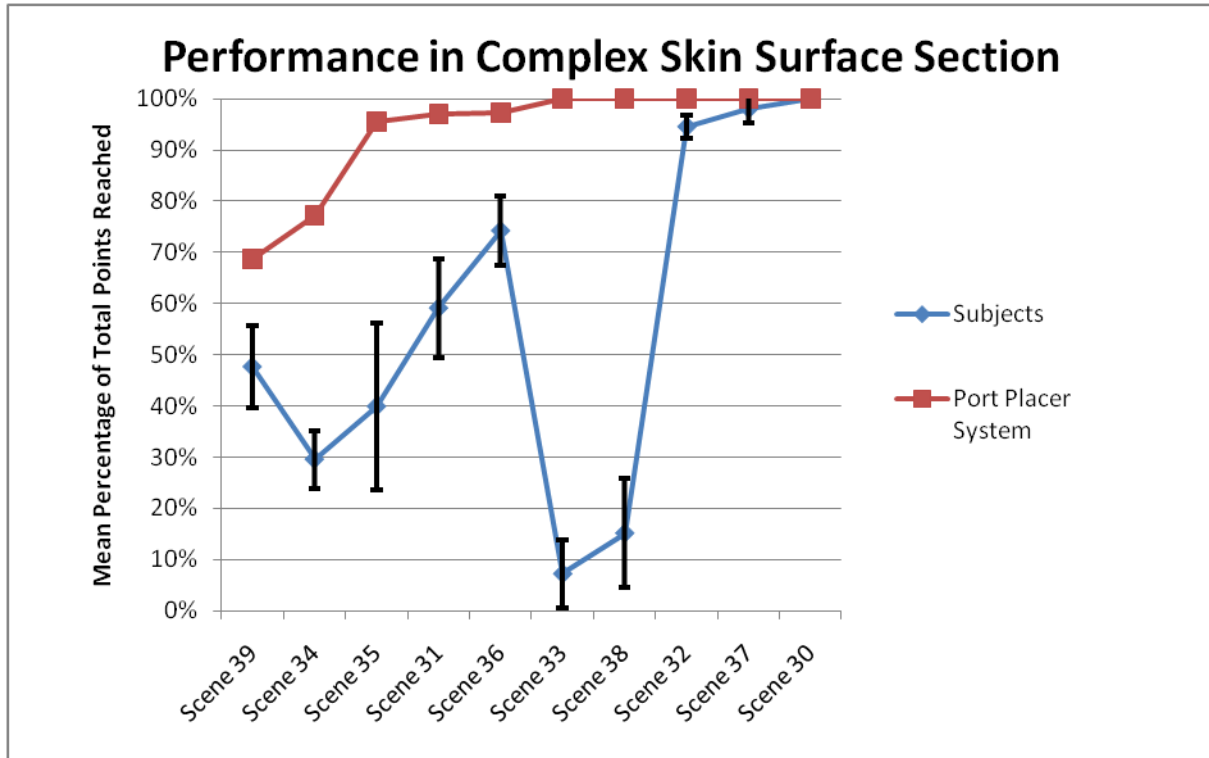


Figure 4-11: Performance for the complex skin surface section. Squares represent the port placer system's performance, while diamonds represent the average participant performance. The black vertical lines represent the 95% confidence interval about each mean.

The obstructions section represented the fifth type of scene. As shown in Figure 4-12, average participant performance ranged from 5% to 43% less than the computer's results.

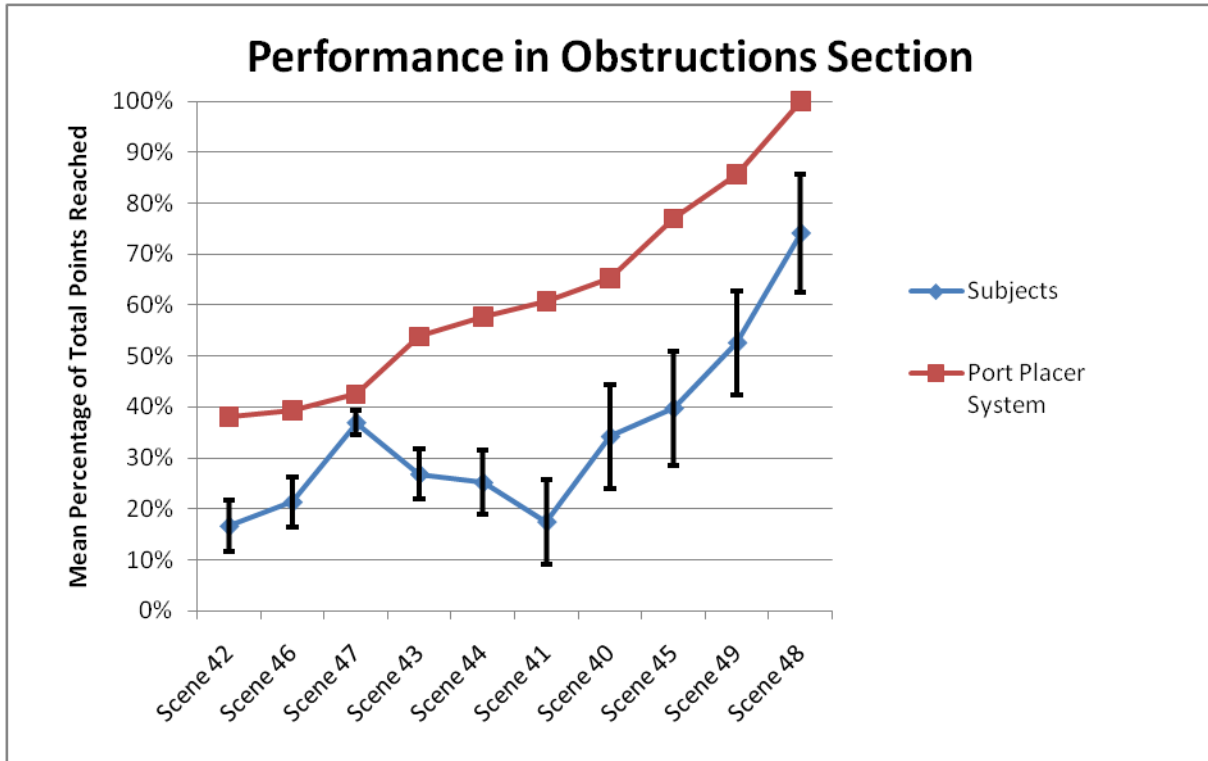


Figure 4-12: Performance for the obstructions section. Squares represent the port placer system's performance, while diamonds represent the average participant performance. The black vertical lines represent the 95% confidence interval about each mean.

4.3 Problem Scenarios

The results demonstrate that human performance tends to lag behind the port placement system's performance by 10% to 25% (on average) depending on the type of scenario. However, there were many cases where human performance was significantly lower than the ideal performance of the port placement system. This section aims to identify conditions that led to these drops in performance.

4.3.1 Separating Ridge

Scene 10 (from the complex target surface section) demonstrates a target surface with target points on both sides of a ridge. In this case, the participants' tendency was to assume that not all of the points could be reached. Therefore, they chose to concentrate on obtaining a

better score on just one side of the ridge. The computer system demonstrated that it is indeed possible to reach 100% of the points in this test. Figure 4-13 shows an example of this scenario.

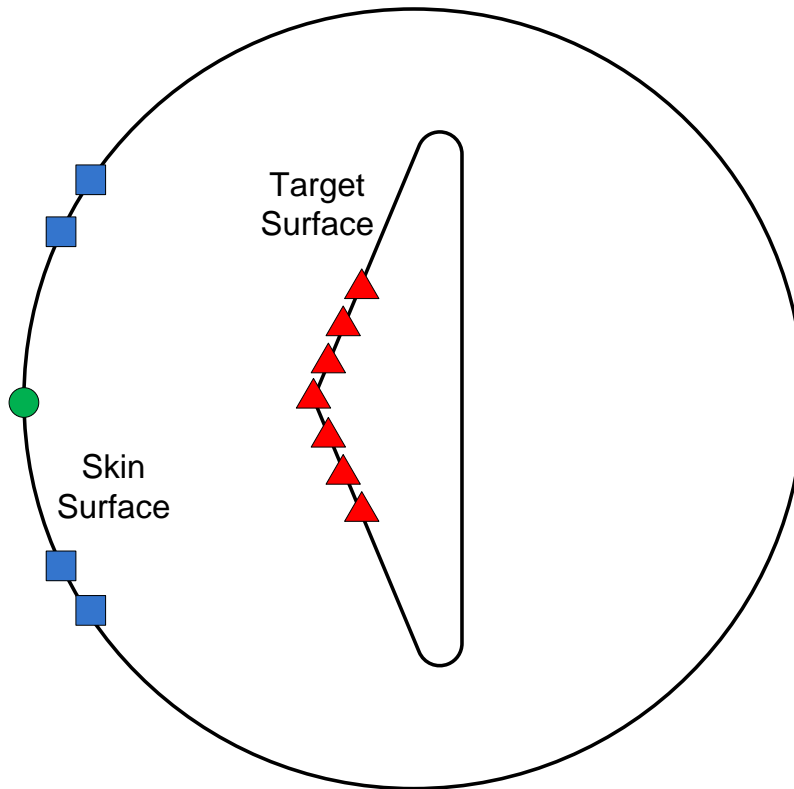


Figure 4-13: Example of the “separating ridge” scenario. The green circle represents the correct choice for port placement, while the blue squares represent typical choices made by participants. The red triangles represent the target points.

4.3.2 Multiple Targets Separated by Distance

Scenes 24, 25, and 26 (from the expansive target surface section) demonstrate multiple groups of target points separated by distance. This case is an extension of the previous case (separating ridge). As in the previous section, the participants had a tendency to focus on reaching one group of points with high accuracy rather than trying to reach both groups with less accuracy. The computer system showed that it is possible to reach both groups of points. Figure 4-14 provides an example of this scenario.

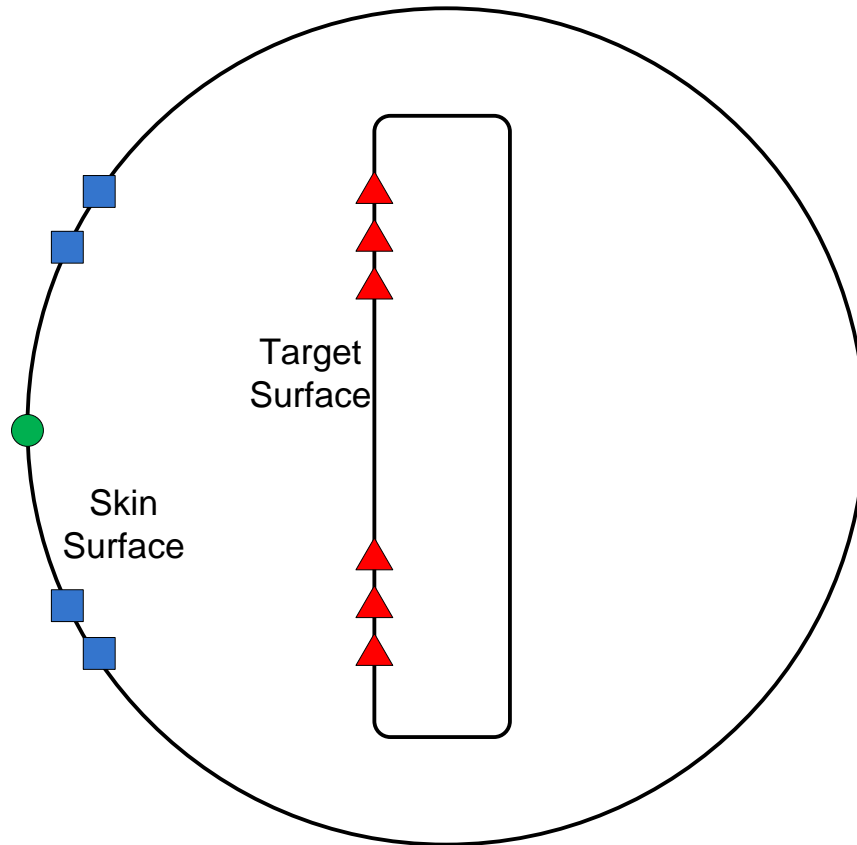


Figure 4-14: Example of the “multiple targets separated by distance” scenario. The green circle represents the correct choice for port placement, while the blue squares represent typical choices made by participants. The red triangles represent the target points.

4.3.3 Significant Distance from Target

Exceptionally low performance was observed for scenes 33, 35, and 38 (from the complex skin surface section). Upon review, it was discovered that these trials contained a second element of difficulty beyond the complex skin surface. The potential port locations that the target surface directly faces (the port locations that would otherwise provide the highest score) are too far away from the skin surface for the probe to reach. Some participants chose these locations regardless, whereas others chose port locations along the side. The extra variable of distance (in addition to the angle of incidence at the target surface) resulted in

participants choosing widely varying port locations. Figure 4-15 provides an example of these results.

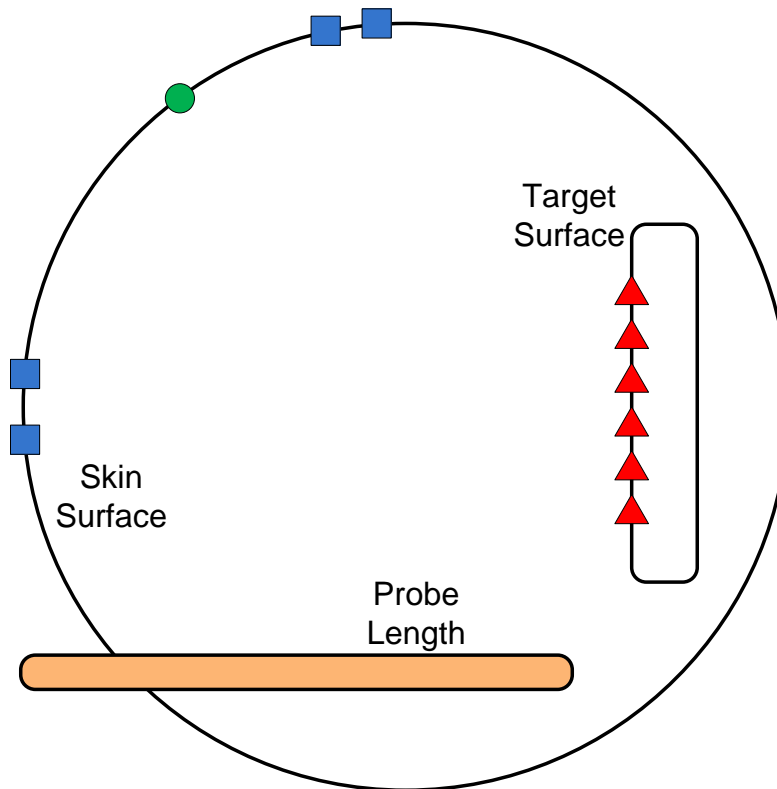


Figure 4-15: Example of the “significant distance from target” scenario. The green circle represents the correct choice for port placement, while the blue squares represent typical choices made by participants. The red triangles represent the target points. The probe model was shown in all scenes to give participants a representation of its length.

4.3.4 Indented Ridge

Scenes 31 and 34 (from the complex skin surface section) have target surfaces very near the skin surface as well as ridges in the skin surface near the optimal port location. As shown in Figure 4-16, it appears that participants were picking port locations along a ridge. This may have been because the ridge was indented and picking points within this indent would serve to minimize the distance to the target surface. However, the distance to the target surface was not an issue in these scenes (unlike the scenes mentioned in the previous section). The challenge of the complex skin surface may have led participants to focus on what seemed to be

a simple solution (minimizing the distance) even though it didn't provide an optimal placement.

Figure 4-16 shows the results of scene 34.

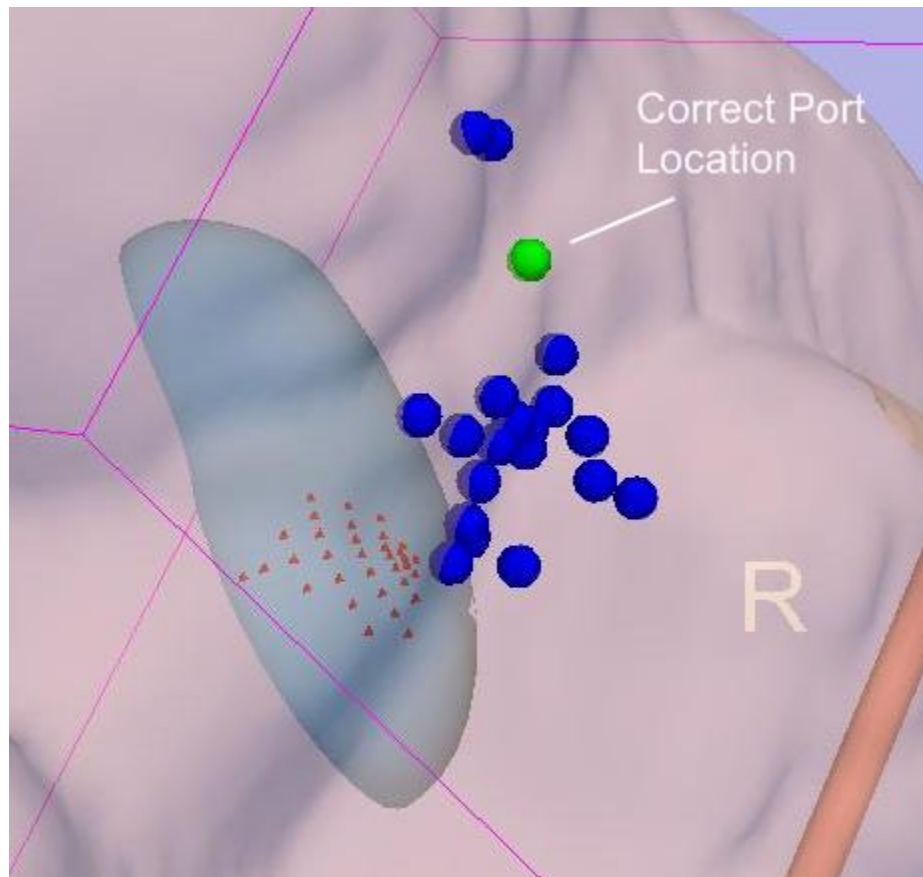


Figure 4-16: Example of the “indented ridge” scenario. The correct choice for port placement (the green circle) is surrounded by the choices of participants (blue circles). The red triangles represent the target points.

4.3.5 Obstructions

Highly inconsistent levels of performance were observed for the obstructions section. Some scenes resulted in relatively good performance, whereas others produced very poor results. Looking closely at the geometric distributions of chosen port locations, it is obvious that in the scenes with better performance, the obstruction was positioned in a manner that obviously limited the choice to one area on the skin surface. The scenes with worse performance had obstructions that made the choice less obvious. In these cases, the

placement of the port varied significantly, leading to poor average performance. Figure 4-17 shows both cases.

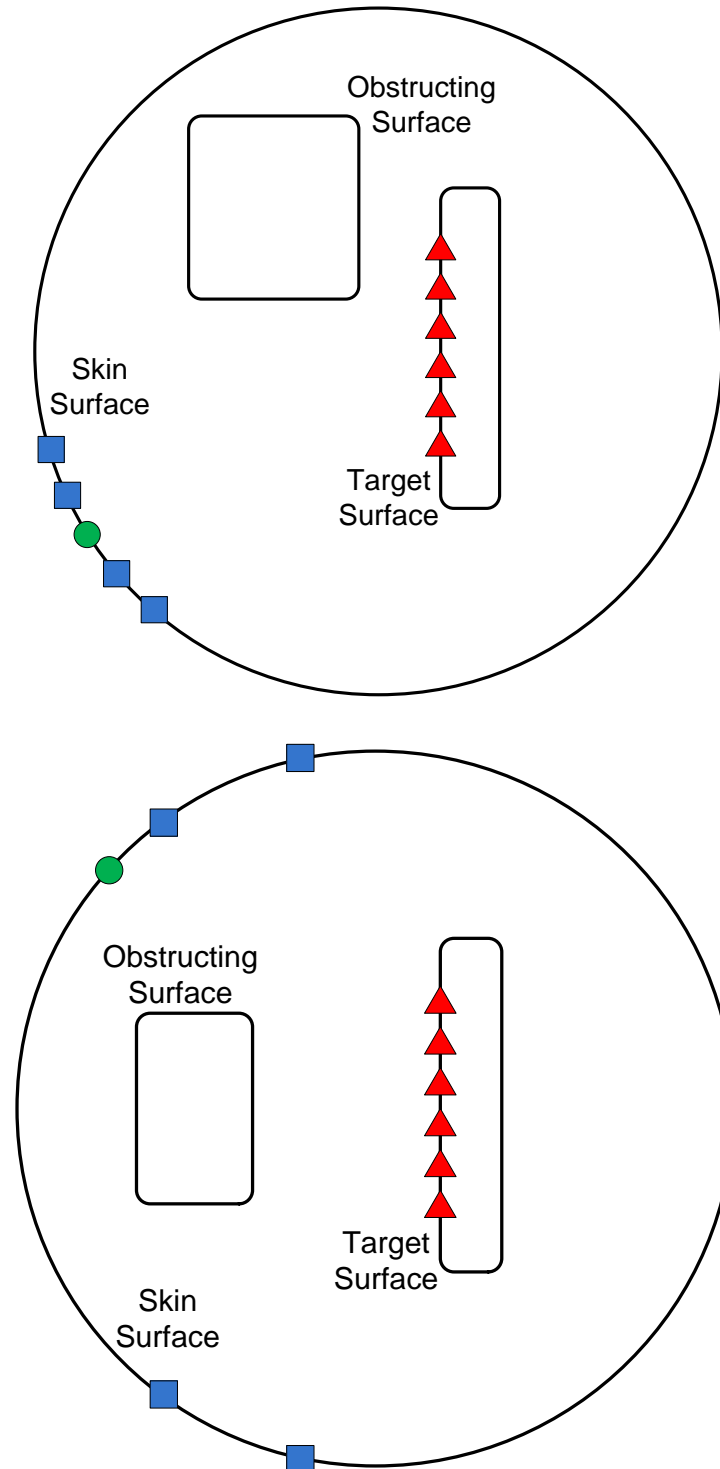


Figure 4-17: Examples of the “obstructions” scenario. The top diagram demonstrates a scenario in which the choice is obvious, whereas the bottom demonstrates a scenario in which the choice is ambiguous. The green circles represent the

correct choices for port placement, while the blue squares represent typical choices made by participants. The red triangles represent the target points.

4.4 Discussion

Proper port placement is critical to a biosensor's ability to gather high quality data and to a surgeon's ability to perform a successful biopsy. Thus, it is important to evaluate the ability of people to find optimal port locations. An optimized port placement system was developed to select the best port location based on the surgeon's area of interest, the biosensor's characteristics, and the patient's anatomy. This system was used to analyze the port selection performance of a group of participants over a variety of test scenarios. The scenarios were designed to investigate different challenges involved in the selection of a port location.

A number of conclusions can be drawn from the analysis of the participants' performance. The first is that the participants uniformly obtain scores approximately 10–25% below the scores obtained by the port placement system. This was expected due to the algorithm's exhaustive search technique for obtaining port locations. However, this indicates that human performance could be improved, perhaps through better training.

From Figure 4-8 through Figure 4-12, we see that the 95% confidence interval of the percentage of target points reached in a given scene was generally 10–20% about the mean. Thus, the number of points reached in a scene was relatively inconsistent. Because the number of reachable points is directly related the quality of the chosen port location, we can infer that the test participants picked port locations of varied quality. Therefore, the second conclusion we can make is that the quality of port locations chosen for a given scene was inconsistent among participants.

In addition, Figure 4-7 shows that for each participant, the 95% confidence interval across all scenes was generally 15%. Consequently, the third conclusion is that the number of reachable points (and thus the port location quality) a given participant achieved was inconsistent from scene to scene.

Lastly, we can see that no one participant vastly outperformed the other participants over the entire experiment. From this data, we can conclude that while port placement was inconsistent from participant to participant for a given test scene, participants on average performed the same over the entire test space.

The results of this study suggest some ways to improve human performance. It may be possible to use the port placement system and the data gathered here to create a training program. Since feedback was not provided to participants during the tests, a minimal amount of learning was able to occur during the tests. By adding modifications to collect and present different performance metrics, it is envisioned that the system could be used as a training tool. For example, by focusing on the areas where performance was degraded and using the computer system to indicate proper placement, it may be possible to increase human performance. In addition, further collection and analysis of data may indicate ways to make the port selection process easier for people.

We identified a common source of error in the Problem Scenarios section for tests involving a significant distance from the target. Subjects erroneously chose port locations that were too distant from the target for the probe to reach the surface. A potential way to improve performance would be to add a virtual tool or measurement device that could be positioned at

a chosen port location to evaluate the ability of the probe to reach the target surface. The effects of such a tool could be analyzed as part of a future study.

Surgeon feedback may suggest further improvements that can be made to the port placement system. One possible improvement would be allowing multiple port locations to be determined. This would enable the system to reach more target points (if the surgeon deems multiple ports to be acceptable). In addition, it would enable the system to be generalized for use in laparoscopic and robotic cases (where multiple ports are required). Another related potential improvement would be generalizing the port placement algorithms to work with tools other than biosensors. Together, these improvements could have broader impacts in port placement during neurosurgery and laparoscopic procedures.

With enhancements and further testing of the port placement system, varying levels of human augmentation and even automation may be possible. Using pre-operative patient imaging, the system could be used to select port locations with minimal human intervention. To assist surgeons in physically creating a port in a patient at the determined location, an augmented reality interface with positioning cues could be implemented [56]. Furthermore, if the system were integrated with a medical robot, the selected port location could be reached automatically. The positioning of a medical robot is the topic of the next chapter.

CHAPTER 5: AUTOMATING BIOSENSOR PROBE PLACEMENT

The InPhotonics portable Raman probe obtains a spectrum from a very small area (e.g. on the order of microns in diameter). Therefore, scanning the relatively large surface area of a tumor requires that the probe be placed at many target locations to take many samples. This is unfeasible to do by hand as stability and accuracy are not within acceptable limits. As stated before, this probe is typical of biosensor designs and therefore provides an analog for general biosensor requirements. This chapter describes the automation of the movement of a surgical robot (AESOP 1000) for the application of manipulating biosensor probes about target locations *in vivo*. In addition, the positional accuracy of this robot is unknown and is therefore analyzed. As a contingency for poor accuracy, the specific factors contributing to the accuracy are identified for consideration in current and future robotic systems for application in biosensor placement.

5.1 Background

The AESOP 1000 robot manipulator is a six degree-of-freedom (DOF) robot consisting of four actively powered joints and two passive joints (Figure 5-1). It was originally designed to hold a laparoscopic camera during minimally invasive surgical procedures. The camera is threaded through a trocar (also called a port) location. The robot allows the surgeon to control the camera without having to use his own hands. The robot communicates with a motion controller (Figure 5-2) through a 55-pin cable. This motion controller accepts input in the form of voice communication or button presses that move the camera through simple motions such as to the left or to the right.



Figure 5-1: AESOP 1000 robotic arm



Figure 5-2: AESOP 1000 motion controller

For simplicity, the robot's joints are referred to by simple nicknames, mimicking a human arm (Figure 5-3).

1. The translational joint is called the linear joint
2. The first rotational joint is called the shoulder
3. The second rotational joint is called the elbow
4. The third rotational joint is called the wrist
5. The fourth rotational joint is called the finger
6. The fifth rotational joint is called the nail

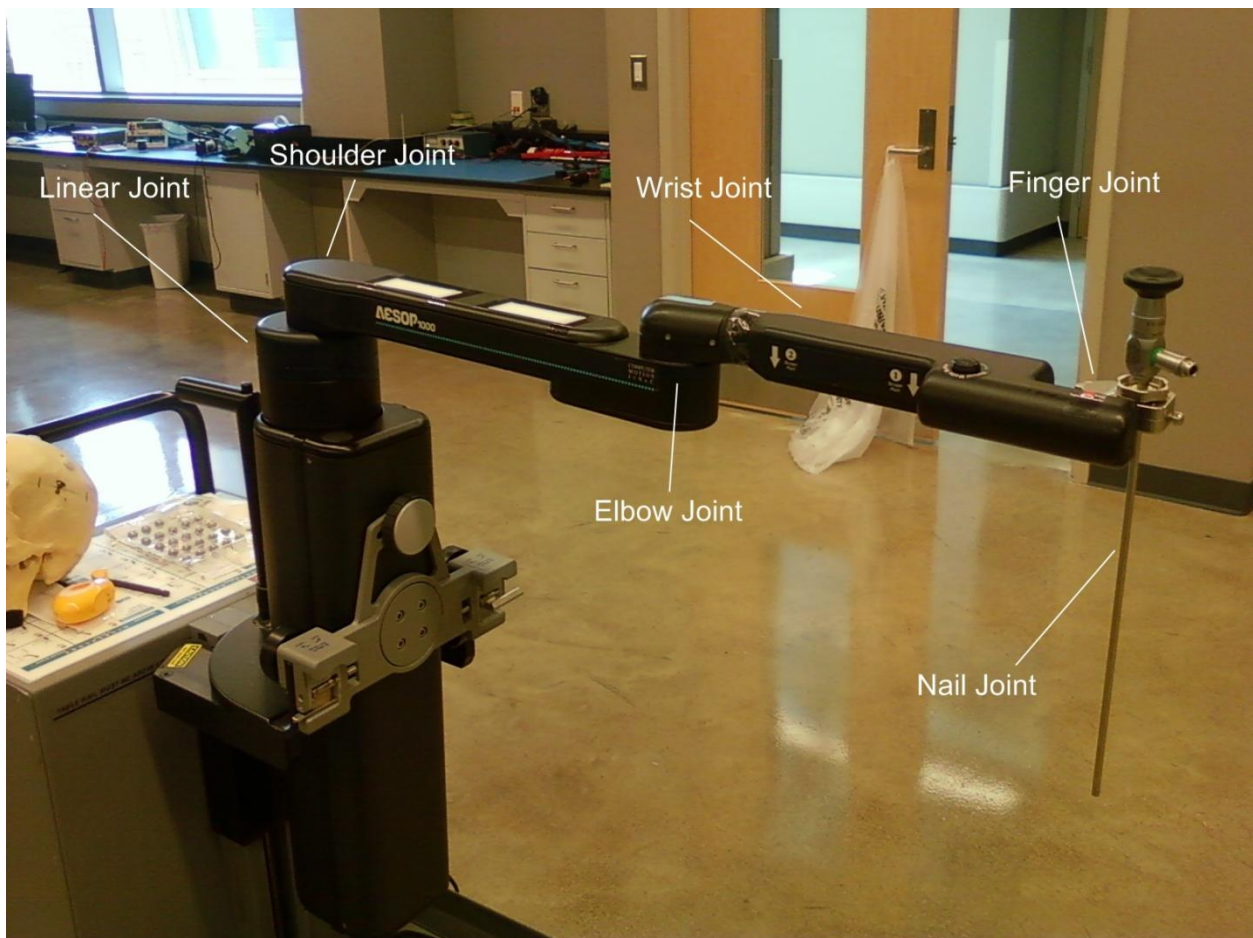


Figure 5-3: The AESOP 1000 in the default position. Joint names are nicknames for easy reference.

Because the robot is rigid and capable of moving an end-effector to a desired location, it fills the role of holding and manipulating the Raman probe. However, the motion control system is too simple for the complex movements needed to move the probe. In addition, the motion control system is proprietary and closed, making modification impossible. However, it is possible to obtain full control through the use of a different motion controller.

5.1.1 Denavit-Hartenberg (D-H) Notation

Robotic manipulators consist of a set of joints and linkages. A robot with n joints is called an n degree-of-freedom robot. This robot would also have $n+1$ links joining each joint with a neighbor. The first link is attached to a static point called the base, and the last link is attached to the end-effector (or in this research, the Raman probe). Figure 5-4 shows an example of a three DOF robot. Note that the joints here are abstracted and could be either rotational or translational. This figure simply demonstrates the notation used for joints and their corresponding links.

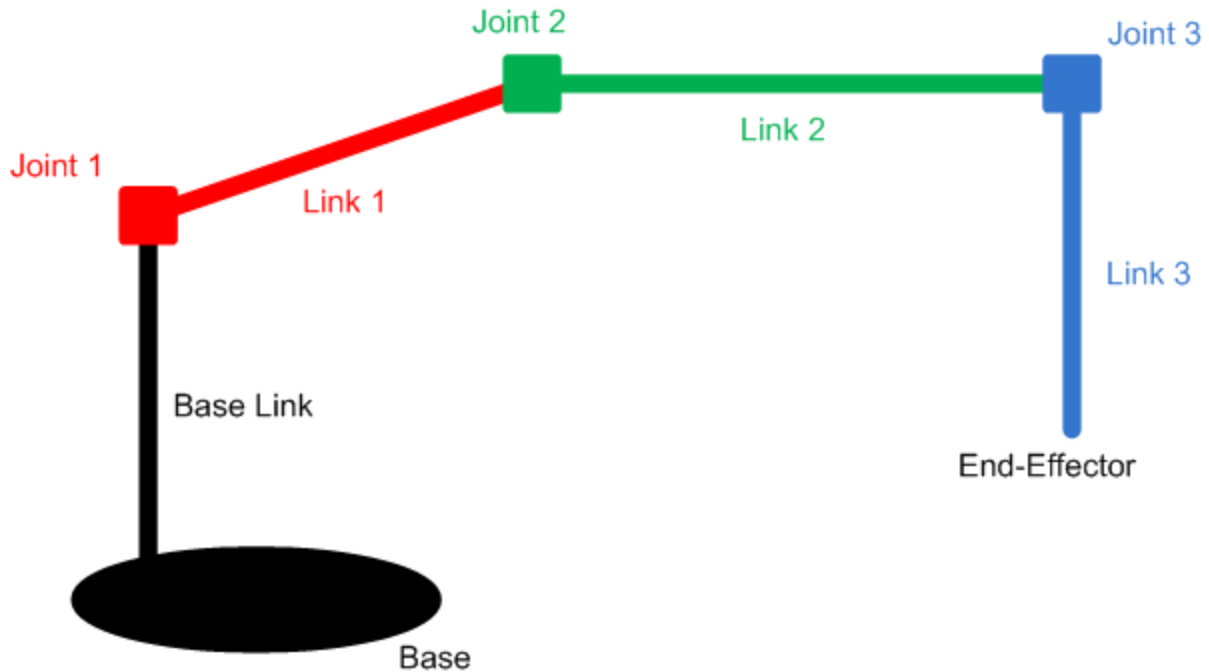


Figure 5-4: A three degree-of-freedom robot

There are two types of joints commonly utilized in robotic manipulators. The first type, translational, extends or retracts its associated link along a fixed axis. The second type, rotational, rotates its associated link about a fixed axis.

Knowing the orientation and dimensions of each link of the robot allows the end-effector location to be found in 3D space. Denavit-Hartenberg (D-H) notation is a way of describing each link in a robot's chain using four parameters [57]. Specifically, the parameters relate each joint's position and orientation to the position and orientation of the previous joint in the chain.

While D-H notation has two forms (standard and modified), only standard notation was used in this research. Standard D-H notation uses four values for each link in the robot chain. Link length (a_i) is the distance between the z_{i-1} and z_i axes along the x_i axis. Link twist (α_i) is the angle from the z_{i-1} and z_i axes about the x_i axis. Link offset (d_i) is the distance from the origin of

frame $i-1$ to the x_i axis along the z_{i-1} axis. Finally, the joint angle (θ_i) is the angle between the x_{i-1} and the x_i axes about the z_{i-1} axis. The link offset (d_i) is variable for a translational joint, while the joint angle (θ_i) is variable for a rotational joint. Figure 5-5 illustrates these values.

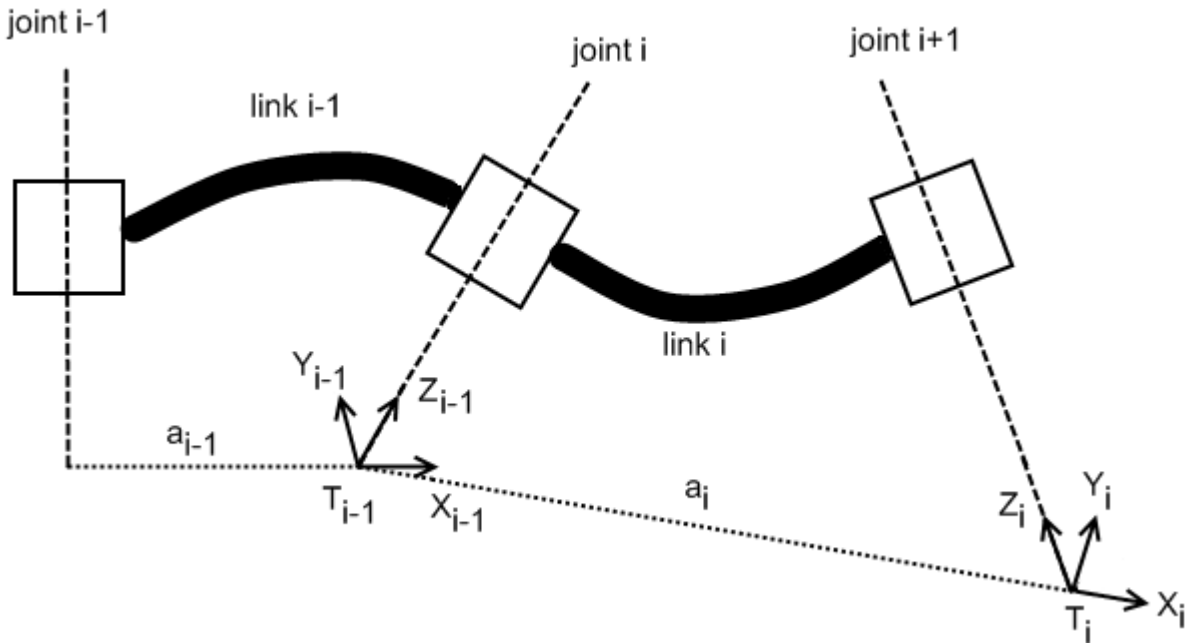


Figure 5-5: Example of standard D-H notation

5.1.2 Locating the End-Effector (Forward Kinematics)

Locating the end-effector (or Raman probe tip) in relation to the base is essential to this research. The base is a fixed point that is used to define a coordinate system in which the positions of the robot's links, joints, and end-effector are established. The end-effector location is found through the use of standard 3D transformation matrix equations [58]. These equations require the knowledge of the physical parameters of the robot including joint variables, link lengths, and general dimensions of the robot.

5.1.2.1 Base-to-Tip Transformation

Utilizing D-H parameters and measurements of the variable joint angles or displacements, a homogeneous 3D transformation matrix can be constructed (Equation 5-1) for each joint location. This transformation describes the location and orientation of the joint in relation to the previous joint in the chain. Multiplying these matrices together results in a transformation matrix that ($T_{BaseTip}$) describes the location and orientation of the end-effector (the robot's tip) in relation to the robot's base (Equation 5-2).

$$joint_trans_i = \begin{bmatrix} \cos(\theta_i) & -\cos(\alpha_i) * \sin(\theta_i) & \sin(\alpha_i) * \sin(\theta_i) & a_i * \cos(\theta_i) \\ \sin(\theta_i) & \cos(\alpha_i) * \cos(\theta_i) & -\sin(\alpha_i) * \cos(\theta_i) & a_i * \sin(\theta_i) \\ 0 & \sin(\alpha_i) & \cos(\alpha_i) & d_i \\ 0 & 0 & 0 & 1 \end{bmatrix} \quad \text{Equation 5-1}$$

$$T_{BaseTip} = joint_trans_1 * joint_trans_2 * \dots * joint_trans_n \quad \text{Equation 5-2}$$

In addition, the transformation matrix can be considered a composite of two smaller matrices: the rotation (Equation 5-3) and position (Equation 5-4) matrices.

$$rotation_trans_i = \begin{bmatrix} \cos(\theta_i) & -\cos(\alpha_i) * \sin(\theta_i) & \sin(\alpha_i) * \sin(\theta_i) \\ \sin(\theta_i) & \cos(\alpha_i) * \cos(\theta_i) & -\sin(\alpha_i) * \cos(\theta_i) \\ 0 & \sin(\alpha_i) & \cos(\alpha_i) \end{bmatrix} \quad \text{Equation 5-3}$$

$$position_trans_i = \begin{bmatrix} a_i * \cos(\theta_i) \\ a_i * \sin(\theta_i) \\ d_i \end{bmatrix} \quad \text{Equation 5-4}$$

Therefore the joint transformation matrix can also be written as:

$$joint_trans_i = \begin{bmatrix} rotation_trans_i & position_trans_i \\ 0 & 0 & 0 & 1 \end{bmatrix} \quad \text{Equation 5-5}$$

5.1.2.2 Registration

To enable the robot to interact with objects, we need a way to know its position in relation to a physical environment (e.g. around and inside the patient). Thus, we need a way to relate the coordinate system of the robot to that of the physical environment. This relationship is defined by a transformation matrix that links the object's coordinate system to the robot's coordinate system. The transformation relates the object's established coordinate system to the base of the robot, which is a fixed point in space. The transformation is found through a process called registration.

To help visualize the robot's position in the real environment, we can use a virtual or augmented reality environment. This space can be populated with 3D models that represent the physical object(s) of interest (such as a patient). The models can be constructed from pre-operative imaging.

Fiducial markers are placed on an object, which have known locations on the object's model in the virtual environment (Figure 5-6). For each fiducial marker, the robot is placed in an orientation such that the end-effector touches the fiducial marker. The *TBaseTip* transformation is recorded for each of these fiducial markers. An algorithm based on iterative Levenberg-Marquardt optimization utilizes the recorded *TBaseTip* transformations and the known fiducial locations to establish a homogeneous transformation matrix (*TObjectBase*) from the object's coordinate system to the robot's coordinate system [14].

The process of registration is done one time before any procedure using the robot. Therefore, any movement of the patient during surgery destroys the registration (*TObjectBase* is no longer accurate). Consequently, any tracking of the end-effector would no longer be

possible until registration is performed again. Examples of types of movements include tissue movements or deformations due to fluid interaction or cavity introduction, patient shifting, or breathing and heart beats. As with the port placement system described in Chapter 3: , this work does not consider the movements of patients and tissues when tracking the end-effector. This limitation is due to the complexity of tissue deformation models and is outside the scope of this research to overcome.

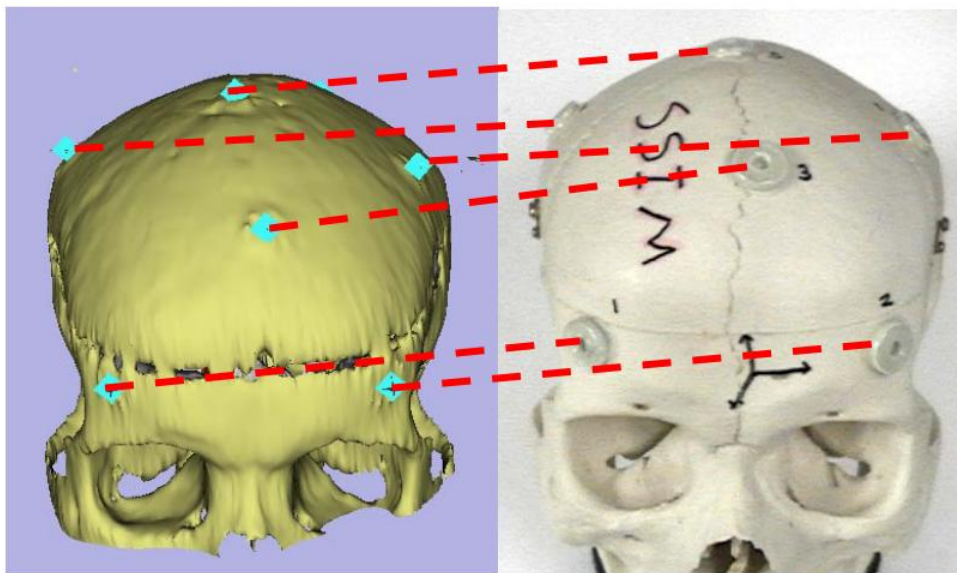


Figure 5-6: Fiducial markers in a virtual scene and their corresponding markers on the real object. Image provided with permission from author of [14].

At least three fiducial markers are needed to generate the transformation matrix. To avoid loss of accuracy due to positioning errors, more fiducials are generally used. For example, seven fiducial markers were used for the model shown in Figure 5-7.

5.1.2.3 End-Effector Location in the Object's Coordinate System

Calculating the location of the end-effector in the object's coordinate system is accomplished by multiplying the registration matrix, $T_{ObjectBase}$, by the current $T_{BaseTip}$ transformation (Equation 5-6).

$$TObjectTip = TObjectBase * TBaseTip$$

Equation 5-6

5.1.3 Optical Encoders

Actively powered joints can use quadrature optical encoders to track their rotation or displacement with a high degree of accuracy. Optical encoders use metal discs rigidly attached to the drive shaft of a motor. These discs have alternating transparent and opaque areas through which a light source is shined. A detector on the opposite side detects if light is shining through the opening or not. The number of cycles of light on and off can be translated to an amount of rotation by the motor and consequently the rotation or displacement of a joint of the robot. Although not utilized in this project, there is a class of encoders called absolute encoders which provides rotation or displacement measurements with respect to a known location referred to as the “zero” location.

By using two sensors, the encoder can not only measure the rotation of a motor, but also the direction of rotation. The two sensors, A and B, are placed in such a way that their outputs are 90° out of phase. In this arrangement, the output of the sensors produces a two-bit Gray code counter.

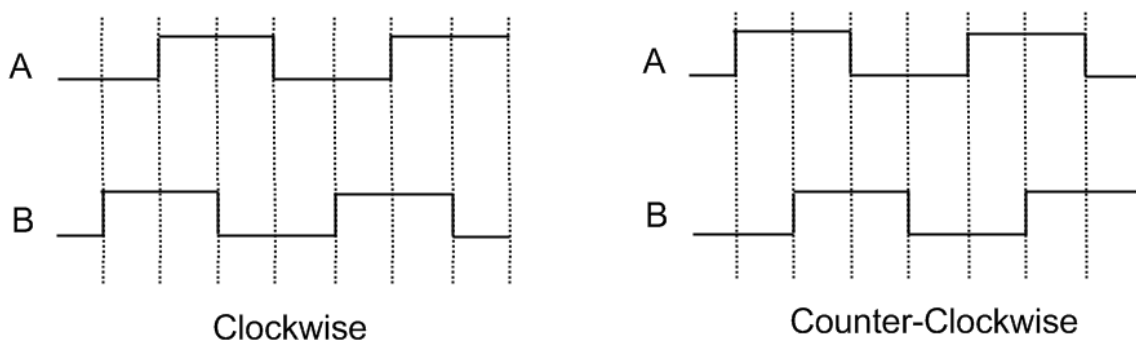


Figure 5-7: Quadrature optical encoder outputs for sensors A and B for clockwise and counter-clockwise movements of a motor

In Figure 5-7, the outputs from the detectors of the optical encoder are shown for both clockwise and counter-clockwise rotations. In clockwise rotation, the output from sensors A and B is 00→01→11→10→00 and so on, where B leads A in changes. During counter-clockwise rotation, the output is 00→10→11→01→00 and so on, where A leads B in changes.

5.2 Methods

Several steps (explained in detail in the following sections) are required in order to obtain full control of the movement of the AESOP robotic arm. First, a test platform was constructed to understand the operation of the robot, and a new motion control system was attached to the robot. Next, the physical parameters of the AESOP robot were measured, allowing the end-effector to be located using forward kinematics. Finally, an inverse kinematics algorithm was implemented, allowing the end-effector to be moved to any desired location.

5.2.1 Test Platform

The test platform allows us to both manipulate the robot in a controlled fashion and observe the control signals going to and from the robot. It consists of a break-out box and a motion controller, both of which are described below.

5.2.1.1 Break-Out Box

In order to attach a different motion controller to the AESOP robot, we had to first decipher the control signals coming from the proprietary controller. To accomplish this, a break-out box was constructed. This consisted of two sets of terminal blocks where the wires from each side of a severed control cable were attached (Figure 5-8). This allowed us to observe the signals coming from and going to the robot during operation. Appendix A: AESOP 1000 Control Pins describes the function of each pin.

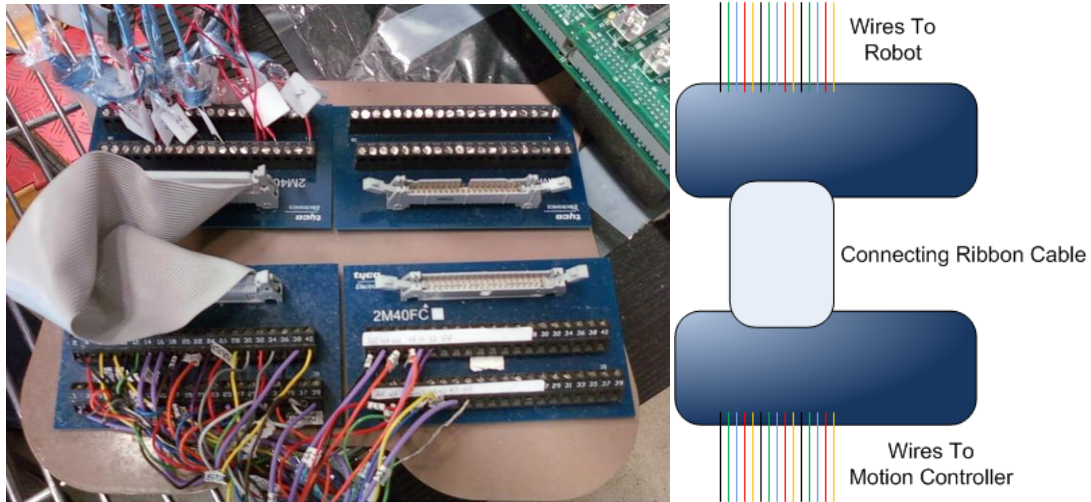


Figure 5-8: AESOP 1000 break-out box and block diagram

The AESOP 1000 uses a combination of optical encoders and potentiometers to track joint variables. The linear, shoulder, and elbow joints have redundant systems of both optical encoders and potentiometers. The passive wrist and finger joints only use potentiometers. The nail joint uses only an encoder.

5.2.1.2 Galil Motion Controller

The Galil DMC-2153 (Galil Motion Control, Rocklin, CA) is a robotic motion controller (Figure 5-9). It is capable of both controlling and tracking robotic motors. This particular version is capable of controlling up to five motors while using either optical encoders or potentiometers for feedback. A user can command the motion controller through several means, including direct serial communication and computer network (TCP/IP) protocols.

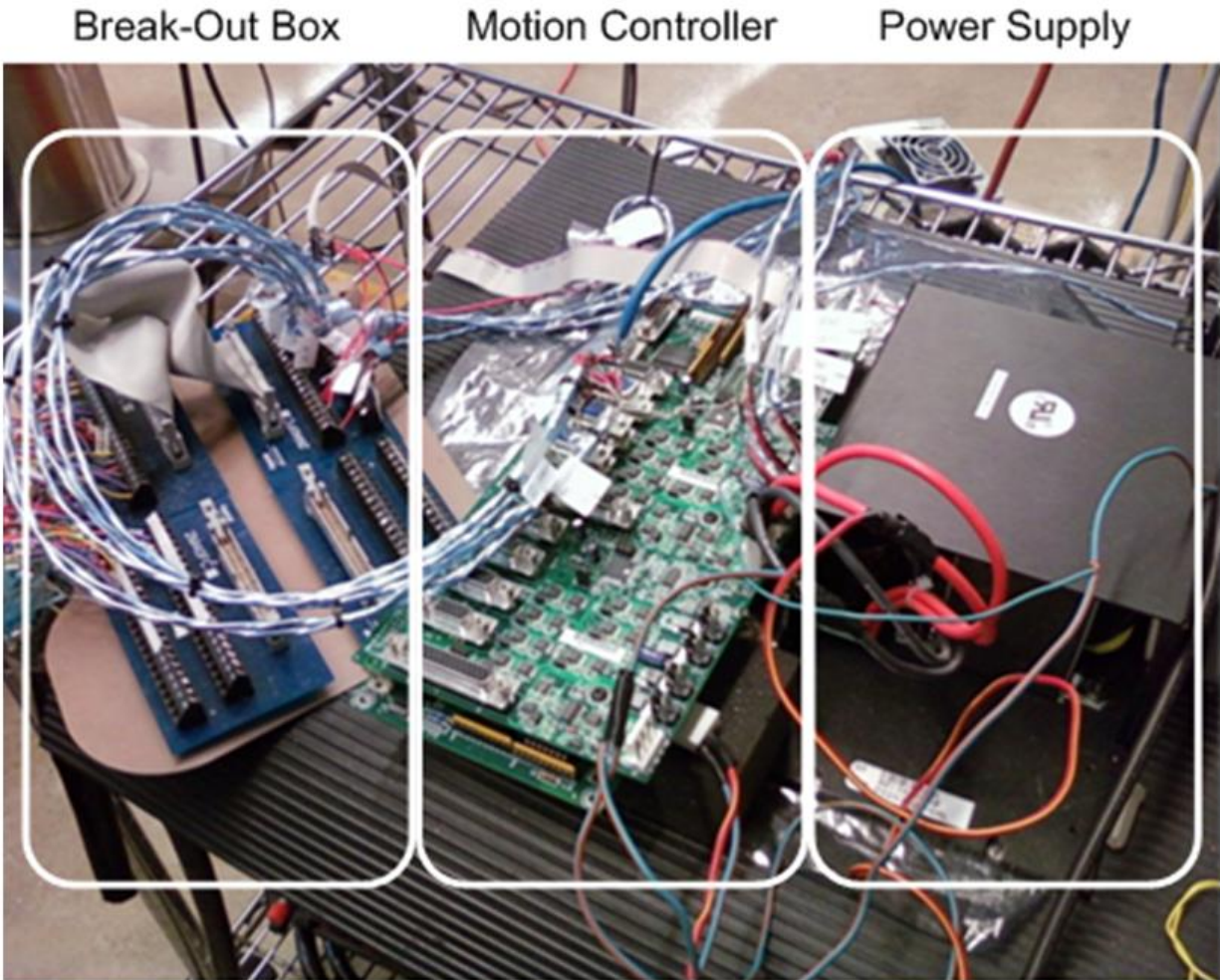


Figure 5-9: Galil motion controller attached to the break-out box

The Galil motion controller was attached to the AESOP robot through the break-out box in place of the standard motion controller. Only optical encoders were used to track the joint variables for the linear, shoulder, and elbow joints because the information from the potentiometers would be redundant. The wrist and finger joints were tracked using the potentiometer measurements. Since the nail joint only affects the rotation of the end-effector, which is not a factor for Raman scans, the nail joint was not wired into the motion controller.

5.2.2 Physical Parameters

Knowledge of the physical parameters of the robot is necessary for locating the end-effector (or Raman probe tip) in relation to the base as well as for controlling the robot. Parameters such as link lengths and joint limitations must be measured. The following subsections describe the physical properties of the AESOP manipulator.

5.2.2.1 Denavit-Hartenberg (D-H) Parameters

Obtaining the D-H parameters is a difficult task with the AESOP robot due to its large size and oddly shaped chassis (Figure 5-1). The large size makes the use of optical methods difficult because the robot extends outside the operating envelope of the measurement device. Ultimately the parameters were obtained using a vernier caliper. Table 5-1 shows the obtained values while Figure 5-10 shows the D-H configuration of each of the joints. Note that we assume the base is located in the same position as the linear joint, which means there is a null transformation from the base to the first joint. The linear joint coincides with the center of the shoulder joint when the linear joint's link is fully retracted. Also note that link 4 is a "dummy" joint. This is needed due to D-H convention's inability to encapsulate a link length along a desired axis of rotation. The dummy joint is inserted as an intermediary to reorient the coordinate frame. Finally note that the ' d ' parameter for link 7 is equal to the length of the attached probe. The probe used in this work had a length of 275.42 mm.

Link	a	A	d	θ	Joint Type
1	0 mm	0 radians	0 mm	0 radians	Translational
2	384.44 mm	0 radians	0 mm	0 radians	Rotational
3	52.71 mm	$\pi/2$ radians	0 mm	0 radians	Rotational
4	0 mm	$\pi/2$ radians	0 mm	$\pi/2$ radians	Dummy
5	0 mm	$\pi/2$ radians	250.7 mm	π radians	Rotational
6	17.2 mm	$-\pi/2$ radians	0 mm	$\pi/2$ radians	Rotational
7	0 mm	0 radians	-275.42 mm	$-\pi/2$ radians	Rotational

Table 5-1: AESOP 1000 D-H parameters

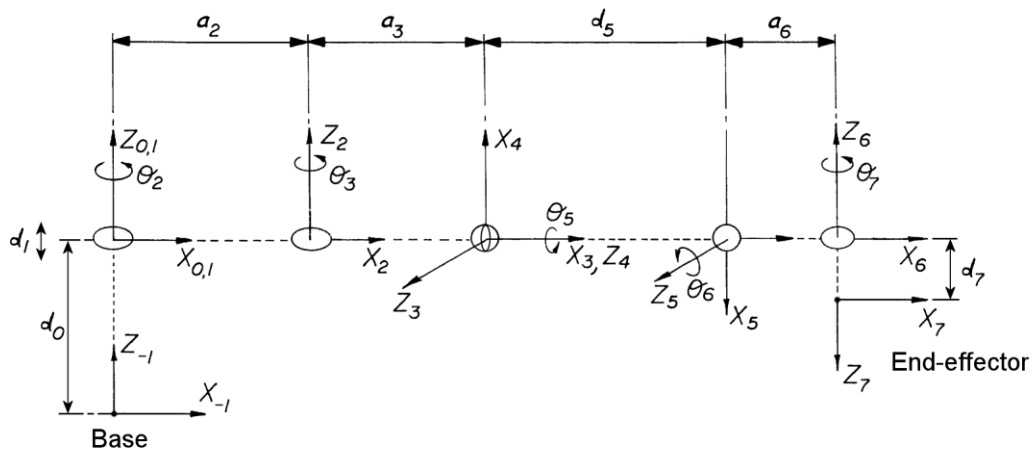


Figure 5-10: Diagram of the D-H configuration of the AESOP 1000 robot

Normally a D-H parameter table contains no values for the variable portion of a particular joint (such as θ for a rotational joint). Table 5-1 contains values in some of these places, which correspond to a default position of that joint. The default positions were chosen to produce a convenient reference configuration of the AESOP's joints. In addition, because the AESOP 1000 uses optical encoders that provide no absolute position information, the reference configuration can be used to define the starting position of each joint (for which the encoder count is zero). The default orientation is shown in Figure 5-3.

5.2.2.2 Joint Limits

The joints of the AESOP manipulator have physical limitations with respect to how far they can rotate or extend before further movement is impossible. When moving the robot with the motion controller, these limitations must be considered so that we do not attempt to move the robot into a potentially damaging or impossible orientation. Therefore, for safe, effective control of the robot with a motion controller, these limitations must be known. Table 5-2 shows the limitations of the joints. Each joint's limitations represent the maximum possible changes from the default orientation. Note that these values do not represent the actual physical limits. The measurement of these values is difficult as the robot tends to rebound slightly when pushed to the limits. In order to keep the robot from approaching these rebound points, these values were picked to be slightly (a few degrees of rotation) lower than the actual physical limits.

Joint	Positive Limit	Negative Limit
Linear	320 mm	0 mm
Shoulder	2.106 radians	-2.106 radians
Elbow	2.711 radians	-2.711 radians
Wrist	2.356 radians	-2.356 radians
Finger	1.570 radians	-1.570 radians
Nail	3.141 radians	-3.141 radians

Table 5-2: AESOP 1000 joint limits with respect to the default orientation

5.2.2.3 Joint Angle Conversion

As stated before, the AESOP robot uses a combination of optical encoders and potentiometers to track joint positions. The active joints (liner, shoulder, and elbow) use optical encoders, while the passive joints (wrist and finger) use potentiometers.

The Galil motion controller monitors the quadrature encoders and produces a real-time count of encoder transitions for each active joint's movements (i.e. 00→01 is one count). In

addition, the motion controller reads the analog potentiometer signals for the passive joints. Since movement and end-effector location are dependent on joint angles/displacement, a conversion from encoder counts and potentiometer voltage to joint angles/displacement is needed.

To obtain this conversion for the rotary shoulder and elbow joints, each joint was put through a procedure that involved moving it a specific number of encoder counts. First, two markers were placed on the robot, and the positions of these markers were recorded, as (X,Y,Z) coordinates, using a Polaris Accedo (Northern Digital Inc., Waterloo, Ontario) optical tracker. From the coordinates of the two markers, a 3D vector connecting the markers was constructed. The robot was then moved, and another vector was constructed for this new joint angle. A vector dot product and inverse cosine provided the angle between these two orientations (Equation 5-7). This was repeated several times, and the average number of encoder counts per radian of rotation was calculated. For the shoulder, an average of 131,583 encoder counts per radian was found. For the elbow, an average of 114,998 encoder counts per radian was found. The collected data is presented in Appendix C: AESOP 1000 Shoulder Joint Encoder Conversion and Appendix D: AESOP 1000 Elbow Joint Encoder Conversion.

$$angle = \arccos(vector_1 \cdot vector_2) \quad \text{Equation 5-7}$$

For the linear joint, the joint was moved a specific number of encoder counts and tracked with the Polaris Accedo. In this case, however, one marker was placed on the linear joint and measured as an (X,Y,Z) coordinate. Comparison with subsequent measurements after moving the joint provided the linear displacement of the joint. This was repeated several times, and the average number of encoder counts per millimeter of displacement was calculated. An

average of 793 encoder counts per millimeter was found. The collected data is presented in Appendix B: AESOP 1000 Linear Joint Encoder Conversion.

For the passive wrist and finger joints, each joint was moved a random amount and securely locked into position, and the analog voltage from the joint's potentiometer was measured. The joint was then photographed using a stationary camera pointing down the axis of rotation. Using two fixed markers on the joint from the gathered image, a simple 2D vector was constructed. Another vector that represented the zero angle was constructed from two fixed points on the robot. The atan2 function (a quadrant-sensitive arctangent function) was used to determine the angle between these two vectors. This function was used for its ability to represent angles beyond $\pm 90^\circ$. This was repeated several times, and a first degree polynomial equation relating the angle to the voltage was fitted to the data. Equation 5-8 shows the equation for the wrist, and Equation 5-9 shows the equation for the finger. The collected data is presented in Appendix E: AESOP 1000 Wrist Joint Potentiometer Conversion and Appendix F: AESOP 1000 Finger Joint Potentiometer Conversion.

$$\text{wrist_angle} = -0.2637(\text{wrist_voltage}) + 0.0096 \quad \text{Equation 5-8}$$

$$\text{finger_angle} = -0.176(\text{finger_voltage}) - 0.0302 \quad \text{Equation 5-9}$$

5.2.3 Positioning the End-Effector (Inverse Kinematics)

Using forward kinematics, we can utilize the knowledge of the joints' orientations to determine the location of the end-effector in space. Conversely, to place the robot into a desired position and orientation, the appropriate joint variables must be determined. The process of finding the necessary joint variables is called inverse kinematics.

Let

$$\Theta = \begin{bmatrix} \theta_1 \\ \theta_2 \\ \vdots \\ \theta_n \end{bmatrix} \quad \text{Equation 5-10}$$

be the set of joint variables from which $T_{BaseTip}$ can be derived as described in Equation 5-2. Also let

$$t = \begin{bmatrix} x_1 & y_1 & z_1 & p_1 \\ x_2 & y_2 & z_2 & p_2 \\ x_3 & y_3 & z_3 & p_3 \\ 0 & 0 & 0 & 1 \end{bmatrix} \quad \text{Equation 5-11}$$

be the target position/orientation for the end-effector given as a homogeneous transformation matrix with respect to the base coordinate frame. Therefore

$$E = T_{BaseTip}^{-1} * t \quad \text{Equation 5-12}$$

is the transformation from the current end-effector position/orientation to the target. The goal of inverse kinematics is to find a new set of joint variables Θ that moves the end-effector to the target t , via the transformation described in E .

There exist several methods for solving the inverse kinematics problem. This work utilizes a technique involving a Jacobian matrix and its pseudo-inverse. This algorithm was chosen for its ability to be generalized to any robot manipulator. Note that the Pseudo-inverse algorithm is unstable near singularities (target points where no robot configuration will place the end-effector at that target). These singularities occur when one or more of the robot's joints are near their limit. This is of little concern for this application as we determine the operating envelope for the robot, and in surgical applications, the robot is rarely placed in positions where the joints are near their limits. In addition, a form of the pseudo-inverse

algorithm is implemented in the MATLAB Robotics Toolbox [59], providing a reference for verification. The following subsections describe the process of calculating the manipulator Jacobian and the pseudo-inverse algorithm.

5.2.3.1 Manipulator Jacobian

The manipulator Jacobian, $J(\theta)$, is a multidimensional matrix that relates movement at the end-effector to movements of the joints [60]. It is essentially a multidimensional form of a partial derivative. In robotic kinematics, two different Jacobian matrices can be used.

The first is called the analytical Jacobian. It requires that equations describing the end-effector location/orientation are known. Specifically, there must be three equations describing the location (X , Y , and Z) and a minimum of three equations describing the orientation with respect to the joint variables θ . The orientation could be in any notation desired, but a minimum of three parameters is necessary to describe an orientation, such as Euler angles. Assuming three orientation parameters, these equations describe a surface in a 6-variable position/orientation space. The analytical Jacobian is populated with the partial derivatives of these equations with respect to each of the joint variables. Thus, this Jacobian relates the changes in the end-effector location to the changes in the joint variables.

When evaluating the Jacobian with a specific set of joint variables, the resulting values of the partial derivatives describe the gradient of the surface in position/orientation space. The described surface is complex for any practical robot; therefore the computed value of the gradient is only valid for the specific set of joint variables.

The second type of Jacobian matrix is called the geometric Jacobian. It is calculated using the D-H parameters. In many cases of robot kinematics, knowing the end-effector

velocities is desirable. In addition, in almost all cases, direct equations describing the end-effector location/orientation are not known. Let ω_x , ω_y , and ω_z be the end-effector angular velocities and v_x , v_y , and v_z be the positional velocities. Also, let e be the vector set of end-effector velocities and $d\Theta$ be the set of joint velocities.

$$e = \begin{bmatrix} \omega_x \\ \omega_y \\ \omega_z \\ v_x \\ v_y \\ v_z \end{bmatrix} \quad \text{Equation 5-13}$$

$$d\Theta = \begin{bmatrix} d\theta_1 \\ d\theta_2 \\ \vdots \\ d\theta_n \end{bmatrix} \quad \text{Equation 5-14}$$

The geometric Jacobian relates changes in the end-effector velocities (e) to the joint velocities ($d\Theta$). This Jacobian is a $6 \times n$ matrix (n being the number of joints) and is calculated via one of several different methods. The method used in this work is a method described by Orin and Shrader [61]. The Jacobian matrix is of the following form:

$$J(\Theta) = \begin{bmatrix} \frac{\partial \omega_x}{\partial \theta_1} & \frac{\partial \omega_x}{\partial \theta_2} & \cdots & \frac{\partial \omega_x}{\partial \theta_n} \\ \frac{\partial \omega_y}{\partial \theta_1} & \frac{\partial \omega_y}{\partial \theta_2} & \cdots & \frac{\partial \omega_y}{\partial \theta_n} \\ \frac{\partial \omega_z}{\partial \theta_1} & \frac{\partial \omega_z}{\partial \theta_2} & \cdots & \frac{\partial \omega_z}{\partial \theta_n} \\ \frac{\partial v_x}{\partial \theta_1} & \frac{\partial v_x}{\partial \theta_2} & \cdots & \frac{\partial v_x}{\partial \theta_n} \\ \frac{\partial v_y}{\partial \theta_1} & \frac{\partial v_y}{\partial \theta_2} & \cdots & \frac{\partial v_y}{\partial \theta_n} \\ \frac{\partial v_z}{\partial \theta_1} & \frac{\partial v_z}{\partial \theta_2} & \cdots & \frac{\partial v_z}{\partial \theta_n} \end{bmatrix} \quad \text{Equation 5-15}$$

In addition, a relationship between the end-effector velocities, joint velocities, and the Jacobian is as follows:

$$e = J(\Theta)d\Theta \quad \text{Equation 5-16}$$

In this work we are not concerned with velocities. Instead, we wish to move the robot from one position to another without any concern for time. We therefore use the set of joint velocities ($d\Theta$) as an estimate of the required change in joint variables. The inverse kinematics algorithm described below uses an iterative process that compensates for any estimation errors. Solving for $d\Theta$ we find

$$d\Theta = J(\Theta)^r e \quad \text{Equation 5-17}$$

where $J(\Theta)^r$ is the pseudo-inverse (or Moore-Penrose inverse) of the Jacobian [62]. To solve this equation, e must be calculated. The set of end-effector velocities is found using a method presented in the MATLAB Robotics Toolbox [59]. This and most methods use the current end-effector (*TBaseTip*) and target (t) positions/orientations. Note that while the method only produces an estimate of the end-effector velocity vector, the estimation can be used due to the iterative nature of the inverse kinematics algorithm described below.

5.2.3.2 Pseudo-Inverse Algorithm

The pseudo-inverse algorithm provides a solution for finding the joint variables needed to place the end-effector at a desired location in space. The pseudo-inverse is used because a true inverse of the Jacobian matrix may not exist. In addition, the algorithm uses an iterative solution to minimize error introduced due to the use of estimates for the velocities. Using the forward kinematics and Jacobian calculations described above, the algorithm is as follows:

1. Compute $T_{BaseTip}$ using current set of joint variables (θ) as in Equation 5-2
2. Find the estimation of e
3. Find the Jacobian matrix based on current joint variables (θ)
4. Calculate the pseudo-inverse (Moore-Penrose inverse) of the Jacobian matrix
5. Calculate $d\theta$ using Equation 5-17
6. Update the joint variables according to $\theta = \theta + d\theta$
7. Go to step 1; repeat until $d\theta$ is below a defined threshold (usually defined as the magnitude of the $d\theta$ vector)

5.2.3.3 Movement Algorithm

The pseudo-inverse algorithm provides the joint variables that place the robotic arm into a particular position and orientation. However, the AESOP 1000 operates through a port that reduces the degrees of freedom at the end-effector. Specifically, there is only one orientation achievable for a given position of the end-effector. Consequently, when a new position is specified, the corresponding orientation is calculated using the target position and the position of the port.

In addition, the tissue surface that the biosensor must touch is often bumpy, with peaks of the surface potentially blocking the path of the biosensor end-effector. The tissue surface should not be impeded upon. However, the area above the tissue is generally open during minimally invasive surgical procedures. This is due to patients being insufflated.

A movement algorithm has been devised that takes into account both the port location and impeding tissues. The movement algorithm is shown in Figure 5-11 and uses the following steps:

1. Back the end-effector away from the current target by a set amount (e.g. 20 mm)
2. Move the end-effector to a position above the next target
3. Move the end-effector towards the next target until it touches the surface

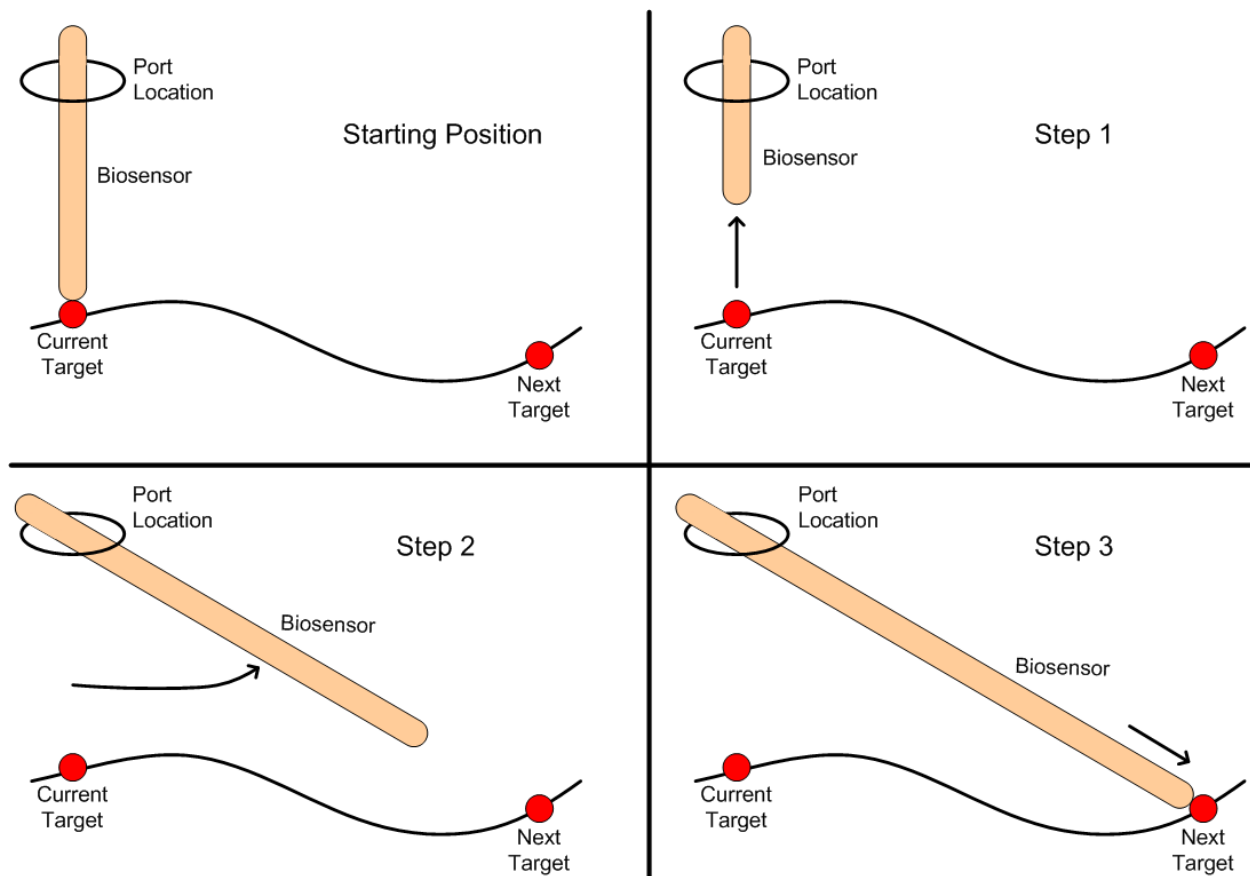


Figure 5-11: Starting and intermediary positions for robot movement from current target to next target

5.3 Results

To verify the operation of the forward kinematics, the robot was registered with a phantom skull filled with various objects. The robot was then moved manually to different locations and tracked using 3D Slicer to visualize a virtual model of the skull and end-effector. This was done without the use of port. It was observed that the virtual end-effector followed the movements of the real robot. While this process did verify the operation of the forward kinematics, it did not evaluate the accuracy of the AESOP robot.

The inverse kinematics algorithm was verified with test cases developed in MATLAB. The MATLAB model of the AESOP robot was created using the MATLAB Robotics Toolbox and the D-H parameters described above. Various target positions/orientations were used as input to both MATLAB's algorithm and our system. In all test cases, the calculated joint variables were the same between the two systems.

Finally, the movement of the robot was evaluated using a port that can be fixed anywhere in space and simple target locations on a flat surface. The movement algorithm performed correctly, following the three steps described above. However, it was noticed that while the end-effector moved in the correct directions and stopped near the target point, it routinely failed to move to the desired location with reasonable accuracy.

To test the positional accuracy of the AESOP robot, a simple test was designed. In order to eliminate additional sources of error, the test was designed to forgo external measurement of the end-effector's location and rely simply on the kinematics of the robot. The AESOP robot base was fixed in a location, while a target point was fixed in 3D space. The AESOP's end-effector was manipulated (without using a port) in order to touch this target from several

orientations. Consequently, the end-effector location (in XYZ coordinates) should always have been the same even when the orientation changed. In this test, the orientation portion of the end-effector is ignored (as it will be changing); only the positional portion is considered. The data collected from four separate tests is presented in Appendix G: AESOP Positional Accuracy Tests.

Simple observation of the data showed that different orientations of the robot result in different end-effector positions, contrary to what was expected and desired. That is, the XYZ values should all be the same (or very close), but they are not. We can see that the largest differential between two data points occurred in test 4, with a difference of 67.22 mm. This means that while the robot end-effector was touching the same place in 3D space, the kinematics algorithms believed those locations to be 67.22 mm apart. The source of this inaccuracy is a combination of factors, which are described in the following subsections.

5.3.1 Home Position and Encoder Conversion

The conversion from joint encoder counts to radians of rotation or millimeters of displacement ultimately determines the orientation of a particular joint. The optical encoders employed by the AESOP robot, however, are not absolute devices. They only provide measures of movement from a known reference position. The reference positions for the joints are obtained through the process of “homing” the robot, whereby the robot is placed into a known orientation and the encoder’s values are set to zero (zeroed).

The AESOP robot’s shoulder and elbow joints have a small amount of flex at their limits of movement. This means that driving the joints to their limits with the motors will not always make the joints end up in the same position. Because of this design, the shoulder and elbow

joints could not be zeroed by rotating the joints to one extreme or the other. Instead, a process was adopted whereby the shoulder and elbow joints were positioned in an outstretched pose (see Figure 5-3) called the “home” position. This process was done by hand and lined up by eye. Therefore, it was possible to introduce angular error by placing the robot in an incorrect home position.

The AESOP’s motors use attached rubber belts to move the various joints. Over time, these belts stretch, causing a change in the encoder conversion factors. Therefore, a new conversion factor must be obtained (or the old values verified) periodically in order to maintain the proper joint angle conversion.

5.3.2 D-H Parameters

The D-H parameter model makes certain assumptions about the motion of particular robotic joints. For example, translational joints are assumed to only move along a fixed linear axis. Similarly, rotational joints are assumed to rotate around a fixed axis at the center of the joint. However, due to loose components, flexing components, etc., there may be undesired motion that is not modeled.

One type of undesired motion is the sagging of the robot when the arm is outstretched. In the home position or other orientations that are similar, the robot sags by a few degrees under the weight of the arm. This can be observed at the robot’s mounting points or, to a slightly lesser extent, in the arm itself. This sag can introduce angular and positional error.

The *TBaseTip* calculation (see Equation 5-2) describes the location of the end-effector in space. This calculation relies on the D-H parameters. Because of the AESOP’s structure, obtaining the D-H parameters proved to be a daunting task. Ultimately, the parameters were

found manually using a vernier caliper. For this reason, there is the potential for error in the measurements.

5.3.3 Registration

The process of registration requires a minimum of three points on the object to which the robot is being registered. This process produces the $TObjectBase$ matrix. As described before, more than three points are generally used. This implies an anticipation of a small amount of error. However, any small amount of error in the $TObjectBase$ matrix will be multiplied into $TObjectTip$ when locating the end-effector in relation to an object (see Equation 5-6). The result is additional error in the position/orientation of the end-effector.

5.3.4 Port Location Registration

As described before, the port location must be known for the movement algorithm to determine an orientation for the robot. While the process of registration may rely on multiple points for redundancy, the port location is a single point in space. The registration of this point therefore lends itself to error. Error in the port location will lead to improper calculation of the orientation needed to place the robot in the desired position. In addition, the greater the distance the end-effector is threaded through the port, the greater an error is produced due to a fulcrum effect. There exist algorithms that are capable of automatically finding the port location in space through a process of moving the end-effector and computing the pivot point [63]. However, these algorithms can be ill-suited for some applications because large movements *in vivo* are not desirable. In addition, inaccurate D-H parameters make the determination of the end-effector position impossible.

5.4 Discussion

Many biosensors gather data from extremely small areas. For example, Raman spectrometers typically gather data from areas smaller than 150 microns in diameter. Therefore, scanning tissues *in vivo* requires many scans. At these scales, the accuracy of the human hand is inadequate for positioning and holding biosensors. This work demonstrates the potential of using medical robotics to accomplish the positioning and holding duties of biosensors, while simultaneously enabling the tracking of these tools for use with image-guided surgery techniques.

Although the robot chosen for this work, the AESOP 1000, was ultimately unable to adequately provide these abilities, it was shown that the techniques for biosensor placement were sound. The limitations of this particular robot lie in its accuracy. Therefore, the lessons learned from this work relate to specific factors that affect accuracy. These factors can be used in future analyses of existing robotic devices, or the design of new robotic devices for the task of biosensor placement.

The single biggest factor limiting the AESOP is accurate D-H parameters. While the registration, encoder conversion, and homing of the robot all affect the accuracy, these processes are fairly well defined. The D-H parameters for the AESOP were obtained with a vernier caliper. This process is inaccurate due to human error and the complex structure of the robot. In addition, inaccurate D-H parameters affect other factors discussed above. For example, registration is affected because the end-effector location must be known in order to calculate the $T_{ObjectBase}$ matrix.

Some newer medical robots already address some of the issues identified here. The da Vinci surgical system, for example, uses a virtual trocar in its movement algorithms. This solves the problem of port location registration as the robot has a defined way of using a fixed location in space. Another example is the neuromate (Renishaw, Gloucestershire, England). This is an FDA-approved robot with a high degree of accuracy that is specifically designed for neurosurgery [64-66]. In addition, it currently integrates with image-guided surgery systems and has been used in a host of applications. We believe that future robots that address the issues identified here will be capable of accurately positioning biosensors *in vivo*.

CHAPTER 6: SUMMARY, APPLICATIONS, AND FUTURE WORK

This chapter will summarize the three major contributions of this dissertation. Following that will be potential applications of this work, including some preliminary investigations. Finally, future areas of research will be presented.

6.1 Summary/Contributions

Minimally invasive surgical procedures are becoming more prevalent every day. New procedures and tools are opening new doors with outcomes never thought possible. However, the lack of direct physical contact with the patient inherently leads to a loss of information for the surgeon. Biosensors offer the possibility to restore this information and take it much further. There are three novel contributions of this dissertation.

The first technological contribution of this dissertation is the implementation details of an automated surgical port placement system specifically designed for biosensors, capable of calculating proper port placement from pre-operative patient imaging. This is a new technology and the implementation is important for researchers in the areas of pre-operative planning and biosensors. This has not been done before due to the lack of biosensor use in minimally invasive surgical procedures. Current port placement algorithms are developed using assumptions for laparoscopic tools and minimally invasive procedures.

The second technological contribution of this dissertation is the implementation of movement algorithms for and the investigation of a surgical robot's suitability for *in vivo* biosensor placement. It was unknown if surgical robotic arms could be adapted for biosensor placement. The implementation details include a detailed description of control algorithms and

robot kinematics, which should be useful to future researchers in the area of robotics. A discussion about the accuracy of the robotic platform and its consequences on biosensor placement is also included, which should be useful for future robotic design considerations. In addition, this work provided a demonstration of our vision of a robotically positioned biosensor.

The human factors contribution of this dissertation is that we have provided an analysis of human performance in the task of port placement. Although the placement of ports for laparoscopic procedures according to surgeon intuition and prior knowledge has been routine, it was unknown if this type of placement would be suitable for biosensor use. This is due to the physical limitations that are inherent to biosensor design. Specifically, we have provided scenarios in which human performance is degraded in comparison to the computer algorithms. Thus, the added cost of utilizing the automated system may be justified.

The ultimate aim of this work is to provide tools and the underlying knowledge that enables biosensors to be used *in vivo* during minimally invasive surgical procedures. While the port placement work shows great promise with positive results, the tested robotic platform lacks the positional accuracy to enable biosensor use. Although this provides a good demonstration, we believe that other systems, such as the da Vinci (Intuitive Inc.) or future robotic systems utilizing the knowledge gained from this dissertation will enable acceptable accuracy.

6.2 Applications and Future Research

There is a large amount of work to be completed in order to realize a robotically positioned biosensor. The most significant work remains in the discovery or development of a robot capable of the accuracy needed for such a task. It is recommended that future

researchers focus on the two largest limitations identified in this work. These are the discovery of accurate structural parameters, and a repeatable, accurate method for placing the robot in a home position.

The following subsections contain applications of the work presented here as well as preliminary and potential future work in these areas.

6.2.1 Robotically Positioned Raman Biosensor

The most obvious future application of this work is a completely robotically positioned Raman biosensor system. It is envisioned that such a system could greatly impact the areas of cancer resection and diagnosis. As conventional histopathology takes 24–48 hours for a complete analysis of removed tissue, a Raman biosensor capable of diagnosing cancer in near real time would greatly enhance the accuracy and speed of cancer resection procedures.

Once an accurate robot is identified, we envision future work to focus on surgical planning and visualization. Some preliminary work on the overall system has been completed [67, 68]. This work utilizes an extremely accurate MicroScribe G2X (Immersion, San Jose, CA) tracking arm (see Figure 6-1). However, this arm is passively articulated, making it unsuitable for surgical use.



Figure 6-1: The Raman probe, attached to the end of the MicroScribe G2X, is used to scan a plastic cup and other objects with the phantom skull

A portable Raman spectrometer was attached to the MicroScribe G2X, registered with a phantom skull filled with various objects (providing an analog for a surgical environment), and tracked using 3D Slicer. Raman scans of the various objects were analyzed using neural networks [67-71]. The results of these scans were presented within the 3D Slicer environment (see Figure 6-2).

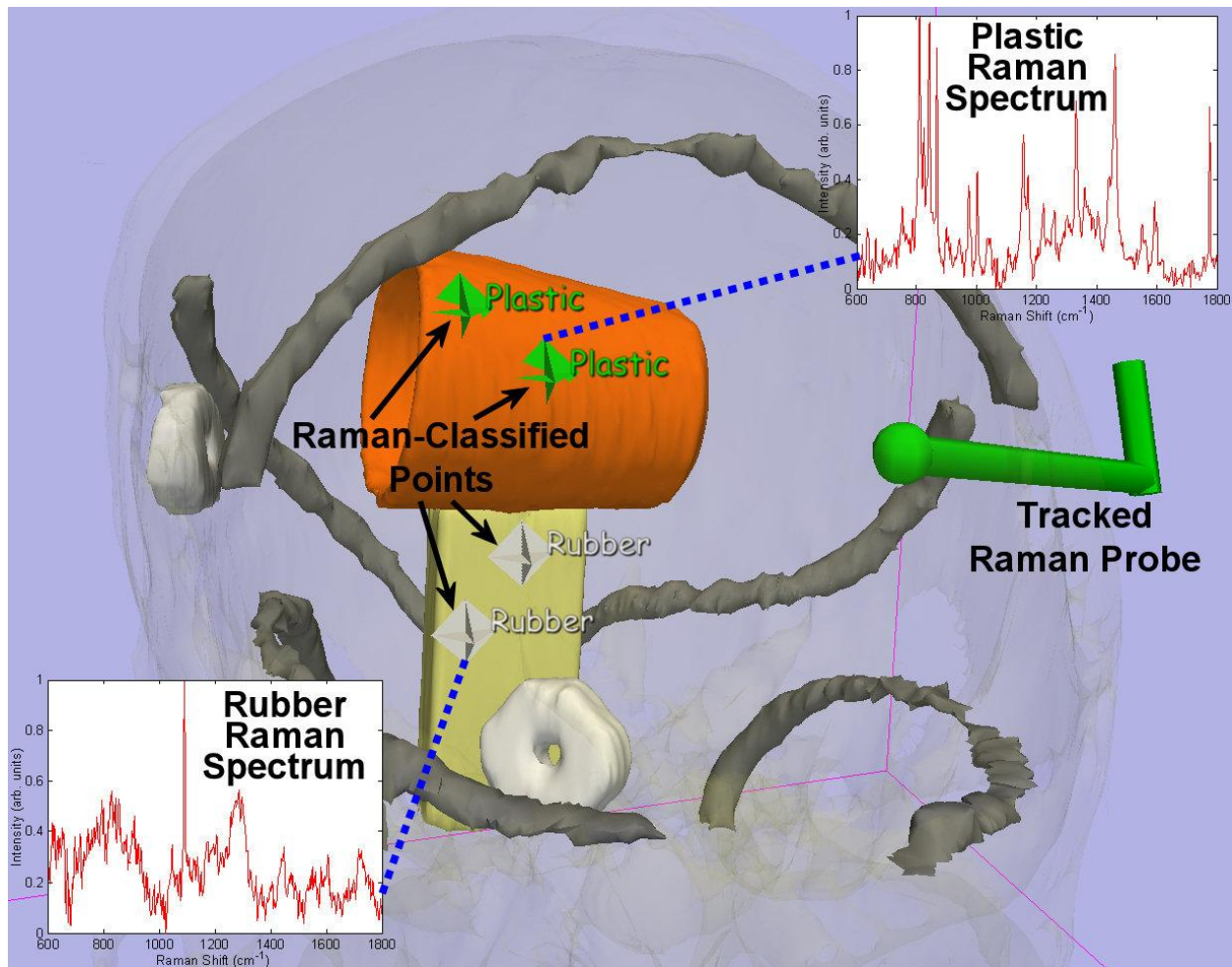


Figure 6-2: A screenshot of our visualization system showing 3D models (derived from CT imaging of the phantom skull), the location of the tracked Raman probe, collected Raman spectra, and colored markers denoting the classifications (computed from Raman scan data) of various objects within the skull

6.2.2 Automated Laparoscopic/Robotic Surgical Camera Placement

One application already showing progress is automated endoscopic camera placement [72, 73]. The AESOP robotic arm was originally designed to hold and manipulate an endoscopic camera. This method uses voice, hand, or foot controls, while conventional camera placement for laparoscopic procedures involves an assistant holding/manipulating the camera. The control algorithms and test platform developed in this work have led to the investigation of automating the control of the endoscopic camera. A system derived from this work tracks the surgical instruments and moves the camera to keep the instruments in view. This system has

the potential of improving surgeon awareness by eliminating the need to concentrate on camera placement.

6.2.3 Port Placement Training

In Chapter 4: human performance in the task of port placement was investigated. The results of this work, in addition to showing that an automated system may be desirable, identified several types of surgical scenarios in which performance was significantly degraded. This information, along with the testing methodology, could be used to design a training program for surgeons with the purpose of increasing accuracy of port placements. The port placement system described in Chapter 3: provides a grading system, while the testing methodology would enable the rehearsal of specific cases. Results could be tracked to show progress over time. Such a system could improve both laparoscopic and robotic minimally invasive procedures.

6.2.4 Optimized Ablation

The port placement system provides an effective starting platform for other software systems pertaining to laparoscopic-related tools. An example of such kinds of tools are microwave or cryoablation tools, which are used for destroying cancerous tissues *in vivo*. Currently these tools are held and positioned by hand. Preliminary work has been done by our research group to investigate the use of software algorithms to optimize the placement of these probes. In this work, pre-operative imaging is used to develop a 3D virtual model of the patient. This is the same process as presented in the port placement system described in Chapter 3: . The algorithm indicates the points from which optimal coverage of a tumor can be achieved with the minimum application of radiation. In the future, this program could be

extended using other features of the port placement system. It is envisioned that the port placement system could decide the best location from which to reach the target points. In addition, with accurate robotics, it may be possible to place the ablation probes at the target locations without any surgeon interaction.

APPENDIX A: AESOP 1000 CONTROL PINS

Pin	Use	Description
1	Ground	
2	Linear up control	When moving up quickly: 4 V When moving up slowly: 4–24 V When moving down: 24V
3	Linear down control	When moving down quickly: 8.5 V When moving down slowly: 8.5–24 V When moving up: 24V
4	Linear potentiometer	At top: 8.78 V At bottom: -8.76 V
5	Shoulder potentiometer	Fully CW: -9.09 V Fully CCW: 8.95 V
6	Elbow potentiometer	Fully CW: -8.9 V Fully CCW: 8.93 V
7	Ground	
8	Shoulder & elbow CCW control	Manual mode: 0 V for CCW motion Variable 0→24 V for increasing CW speed Hand control: 24 V for CW motion Variable 24→0 V for increasing CCW speed
9	Shoulder & elbow CW control	Manual mode: 0 V for CW motion Variable 0→24 V for increasing CCW speed Hand control: 24 V for CCW motion Variable 24→0 V for increasing CW speed
10	9.48 V DC	
11	-9.49 V DC	
12	Wrist potentiometer	Fully CW: 9.14 V Fully CCW: -8.8 V
13	Finger potentiometer	Fully up (default): 9.11 V Fully down: -8.93 V
14	Ground	
15	Ground	
16	Ground	
17	Delayed finger potentiometer?	Acts like a slow/delayed version of the finger potentiometer with lower voltages. Fully up (default): 1.254V Fully down: -2.589 V
18	4.98 V DC	
19	Should & elbow encoder 1	Elbow and shoulder not moving: Stays at 0.25 V or 4.99

		V. When elbow or shoulder moving: ~ 2.3 V (average)
20	Should & elbow encoder 2	Same properties as pin 19
21	Shoulder CCW control	Manual mode: (0 V for CCW motion?) 24 V when no motors engaged 0 V when other motor(s) engaged Variable 0→25 V for increasing CW speed Hand control: (24 V for CW motion?) 24 V normally Variable 24→~17 V for increasing CCW speed
22	Shoulder CW control	Manual mode: (0 V for CW motion?) 0 V normally Variable 0→24 V for increasing CCW speed Hand control: (24 V for CCW motion?) 24 V normally Variable 24→0 V for increasing CW speed
23	Nail CW control	Hand control: (24 V for CCW motion?) 24 V normally Variable 24→~16 V for increasing CW speed
24	Nail CCW control	Hand control: (24 V for CW motion?) 24 V normally Variable 24→~16 V for increasing CCW speed
25	Ground	
26	Linear encoder 1	Linear not moving: Stays at 0.25 V or 4.98 V. When linear moving: ~ 2.5 V (average)
27	Linear encoder 2	Same properties as pin 26
28	Shoulder encoder 1	Shoulder not moving: Stays at 0.25 V or 5 V. When shoulder moving: ~ 2.5 V (average)
29	Shoulder encoder 2	Same properties as pin 28
30	Motor power?	When motors engaged (ready for motion): 24 V [e.g. when manual mode button held down or when configured for hand control (finger held horizontal and manual mode button pushed)] Otherwise: 0 V
31	Motor ground?	(Not a green-tubed wire) 0 V normally 0.4 V when any motor is moving
32	5 V DC	
33	Poor ground?	Fixed DC voltage of 0.035 V
34	Nail encoder 1	Nail not moving: Stays at 0.3 V or 4.99 V. When nail moving: ~ 2.6 V (average)

35	Nail encoder 2	Same properties as pin 34
36	4 V DC	
37	Poor 0.57 V DC?	Jitters around an average DC voltage of ~ 0.57 V
38	Ground	(Green-tubed wire)
39	Ground	(Green-tubed wire)
40	Ground?	(Yellow wire) Fixed DC voltage of 0 V (?) Either a ground or floating
41	Poor ground?	Fixed DC voltage of 0.097 V Either a poor ground or floating
42	Ground	(Black wire)
43	Poor ground?	(Red wire) Fixed DC voltage of 0.001 V Either a poor ground or floating
44	Ground	(Green-tubed wire)
45	4 V DC	
46	Poor 0.6 V DC	Jitters around an average DC voltage of ~ 0.6 V
47	5.08 V DC	
48	Poor ground?	(Orange wire) ~ 0 V Either a ground or floating
49	Poor ground?	(Yellow wire) ~ 0 V Either a ground or floating
50	Ground	(Green-tubed wire)
51	4.99 V DC	
52	4.99 V DC	
53	Ground	(Green-tubed wire)
54	Cable ground	Connected to the inside and outside of the connectors on both ends of the cable
55	Cable ground	Connected to the inside and outside of the connectors on both ends of the cable

APPENDIX B: AESOP 1000 LINEAR JOINT ENCODER CONVERSION

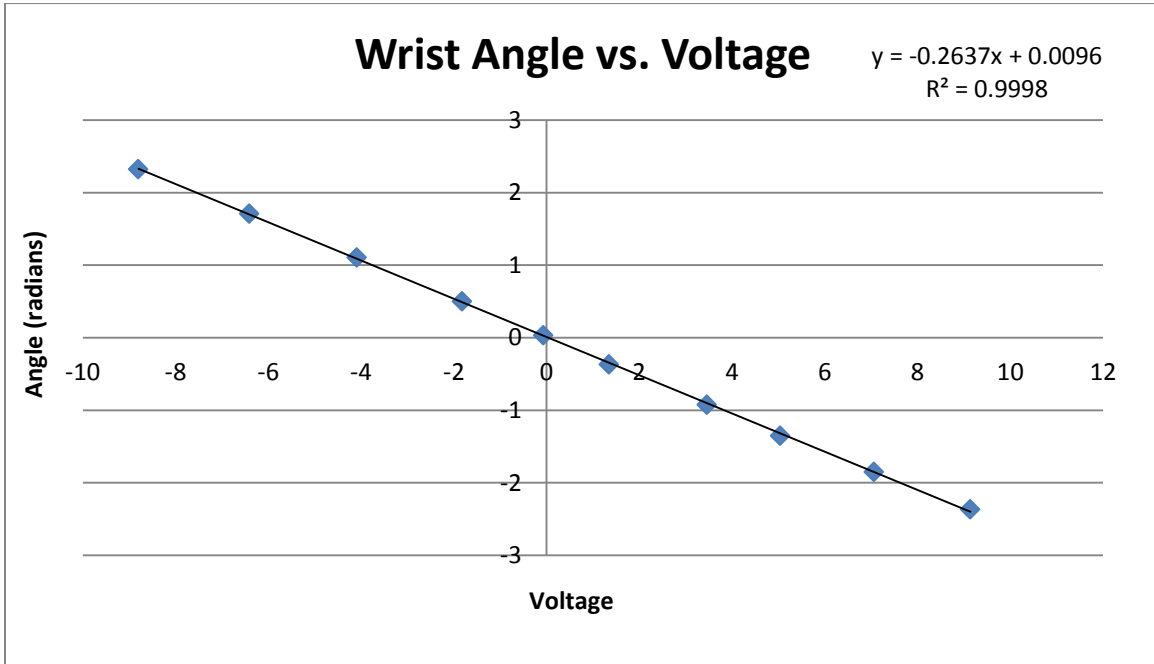
Encoder Count	Tx	Ty	Tz		Distance Moved (mm)	Encoder Change	Encoder Counts Per mm
45220	174.3	-160	-1115.8				
25034	148.8	-160	-1118.7		25.66437219	-20186	-786.5378451
5054	124	-160.1	-1122.4		25.07468843	-19980	-796.8194721
-14911	99	-160.1	-1126.2		25.28715089	-19965	-789.5314142
-34910	74.2	-160	-1129.8		25.06012769	-19999	-798.0406263
-54917	49.3	-159.8	-1132.8		25.0808692	-20007	-797.6996267
-74897	24.2	-159.8	-1136.5		25.37124356	-19980	-787.5057425

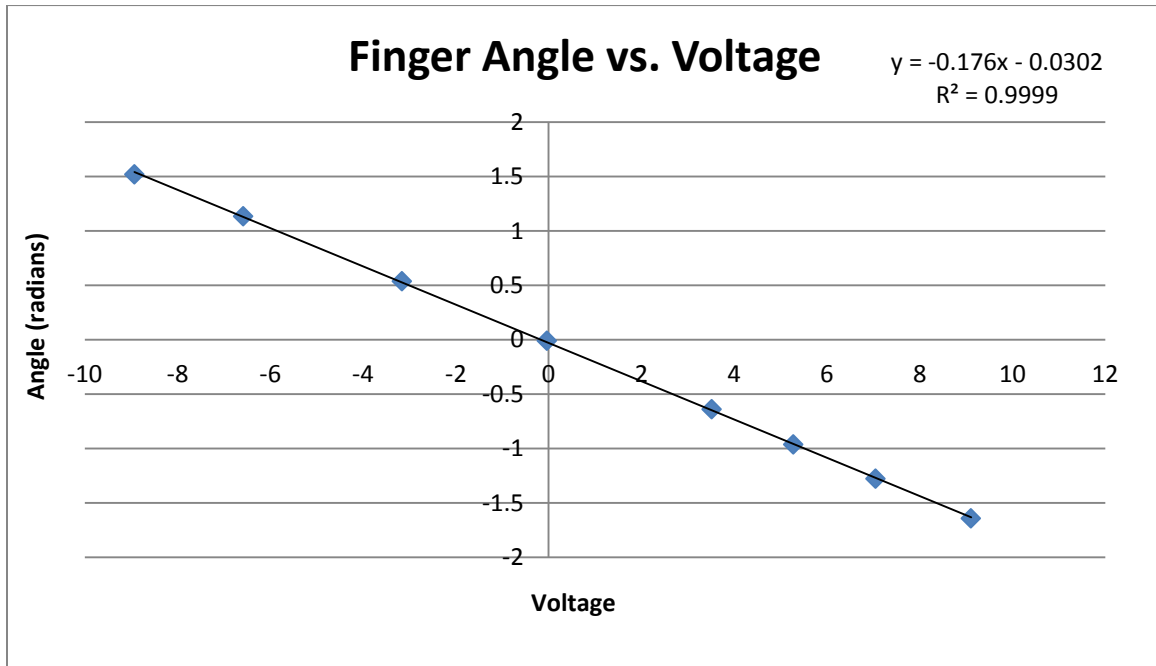
APPENDIX C: AESOP 1000 SHOULDER JOINT ENCODER CONVERSION

Encoder Count	Tx1	Ty1	Tz1	Tx2	Ty2	Tz2		Vx	Vy	Vz	Distance Moved (radians)	Encoder Change	Encoder Counts Per radian
-226501	68.5	-54.54	-1218.5	43.96	-4.7	-1039.5		-24.54	49.84	179			
-196499	69.48	-35.7	-1223.4	47.25	54.26	-1060		-22.23	89.96	163.4	0.23024199	30002	130306.3789
-166499	70.97	-16.6	-1235.1	52.28	108.25	-1095.35		-18.69	124.85	139.75	0.225350596	30000	133125.8957
-106498	75.5	11.1	-1267.2	66.85	185.4	-1196.2		-8.65	174.3	71	0.456694537	60001	131381.033
13497	87.15	12.4	-1349.1	101.8	175.7	-1441.4		14.65	163.3	-92.3	0.909042556	119995	132001.5209
133495	94.36	-52.8	-1400.6	121.64	-27.4	-1584.6		27.28	25.4	-184	0.915319918	119998	131099.518

APPENDIX D: AESOP 1000 ELBOW JOINT ENCODER CONVERSION

Encoder Count	Tx1	Ty1	Tz1	Tx2	Ty2	Tz2		Vx	Vy	Vz	Distance Moved (radians)	Encoder Change	Encoder Counts Per radian
16415	103.57	66.2	-1256.2	98.7	71.8	-1229.1		-4.87	5.6	27.1			
-33585	103.4	62.1	-1253.9	99.2	79.4	-1232.2		-4.2	17.3	21.7	0.463615558	-50000	-107847.9769
-83587	103.1	59.6	-1251.2	100.34	84.6	-1238.1		-2.76	25	13.1	0.415167244	-50002	-120438.2106
-133586	102.55	58.7	-1246.9	101.46	86.4	-1245.1		-1.09	27.7	1.8	0.42077071	-49999	-118827.1873
-183585	101.65	59.5	-1243	103.1	85.4	-1253.2		1.45	25.9	-10.2	0.449270529	-49999	-111289.294
-283574	100.35	65.4	-1238.2	105.3	74.65	-1264.3		4.95	9.25	-26.1	0.857626953	-99989	-116587.9869

APPENDIX E: AESOP 1000 WRIST JOINT POTENTIOMETER**CONVERSION**

APPENDIX F: AESOP 1000 FINGER JOINT POTENTIOMETER**CONVERSION**

APPENDIX G: AESOP POSITIONAL ACCURACY TESTS

Test #1

Data Point	X	Y	Z
1	524.574358	-82.66687	-205.629861
2	521.476404	-78.174722	-172.333582
3	522.434961	-81.548368	-206.99088
4	524.094198	-73.140039	-191.916763
5	516.573776	-65.794138	-179.998825
6	518.531857	-72.890142	-178.44276
7	514.180436	-70.706134	-200.704265
8	516.750571	-69.606718	-189.466138
9	513.893028	-63.367088	-185.941974
10	504.188694	-87.1076	-202.060968
11	503.334216	-82.658407	-205.942266
12	493.520333	-84.534993	-203.837181
13	494.06761	-85.822935	-209.662253
14	502.190709	-81.440484	-199.305455
15	507.957224	-86.01856	-199.561571
16	507.941914	-78.993437	-208.240378
17	488.794133	-88.600587	-215.481894
18	507.562293	-71.759283	-175.479235
19	508.043326	-79.792907	-203.694318

Test #2

Data Point	X	Y	Z
1	18.485291	-537.015165	-214.177931
2	20.273482	-536.668742	-223.862184
3	22.158442	-534.140172	-230.294728
4	26.635293	-531.277909	-213.264834
5	29.073236	-524.50478	-225.988738
6	25.2811	-527.126186	-222.273663
7	19.036653	-531.980441	-225.316845

8	10.684031	-538.775684	-223.050654
9	18.245047	-536.995149	-209.31205
10	3.258392	-519.350927	-234.319754
11	7.631817	-521.684997	-231.721661
12	2.232406	-525.168048	-234.730204
13	-2.477423	-512.270224	-240.899376
14	1.013554	-510.734701	-242.788318
15	9.718285	-522.388459	-228.621032
16	9.562081	-522.702631	-231.451111
17	8.027885	-524.847683	-234.322736
18	-4.465863	-524.417876	-241.040227
19	1.595823	-513.431963	-242.596411
20	6.090366	-521.692036	-238.838741

Test #3

Data Point	X	Y	Z
1	34.929897	464.54613	-233.679731
2	33.030776	472.748133	-233.262941
3	29.345985	484.576663	-231.061935
4	33.242722	479.478279	-218.286226
5	26.306863	476.954919	-213.997085
6	27.863606	480.041216	-218.628338
7	26.712156	482.270287	-223.362634
8	28.831057	477.229757	-214.569399
9	34.365535	461.82662	-229.094998
10	32.743183	476.105035	-227.424429
11	7.506911	499.399716	-220.799958
12	25.853032	505.614993	-216.056662
13	26.222353	511.146144	-200.992237
14	8.593604	500.949085	-191.899831
15	-2.624963	492.556077	-206.813654
16	-6.837628	494.571891	-214.312867
17	-1.631633	502.056593	-222.8102
18	28.733932	512.927089	-219.18805
19	22.044373	509.588548	-228.798511
20	25.744467	510.52167	-193.9703

Test #4

Data Point	X	Y	Z
------------	---	---	---

1	466.862132	-35.432239	58.253058
2	459.137845	-36.688081	59.679882
3	443.583376	-44.763205	44.091864
4	447.794926	-42.796132	26.734014
5	470.778863	-42.568024	46.773337
6	468.430939	-37.769842	36.480447
7	455.649124	-41.524379	55.840116
8	442.70271	-46.745095	31.896692
9	455.786389	-40.811082	36.322987
10	468.150749	-37.810554	48.613235
11	482.06815	-29.709164	61.220936
12	482.931875	-32.250105	39.684082
13	475.156482	-26.697006	73.378358
14	476.212836	-16.360409	81.612702
15	467.638048	-6.248758	61.800813
16	476.167195	-29.477224	35.316124
17	477.835745	-27.830806	37.566424
18	473.597536	-31.066708	28.94066
19	479.603077	-29.572549	56.665067
20	464.539535	-17.888448	77.322196

BIBLIOGRAPHY

- [1] J. Wang, "Glucose biosensors: 40 years of advances and challenges," *Electroanalysis*, vol. 13, pp. 983-88, 2001.
- [2] K. Lange, B. E. Rapp, and M. Rapp, "Surface acoustic wave biosensors: a review," *Analytical and Bioanalytical Chemistry*, vol. 391, pp. 1509-19, Jul 2008.
- [3] J. T. Motz, M. Hunter, L. H. Galindo, J. A. Gardecki, J. R. Kramer, R. R. Dasari, and M. S. Feld, "Optical fiber probe for biomedical Raman spectroscopy," *Applied Optics*, vol. 43, pp. 542-54, Jan 20 2004.
- [4] T. Vo-Dinh and B. Cullum, "Biosensors and biochips: advances in biological and medical diagnostics," *Fresenius Journal of Analytical Chemistry*, vol. 366, pp. 540-51, Mar-Apr 2000.
- [5] A. S. Haka, K. E. Shafer-Peltier, M. Fitzmaurice, J. Crowe, R. R. Dasari, and M. S. Feld, "Identifying microcalcifications in benign and malignant breast lesions by probing differences in their chemical composition using Raman spectroscopy," *Cancer Research*, vol. 62, pp. 5375-80, Sep 15 2002.
- [6] A. S. Haka, K. E. Shafer-Peltier, M. Fitzmaurice, J. Crowe, R. R. Dasari, and M. S. Feld, "Diagnosing breast cancer by using Raman spectroscopy," *Proceedings of the National Academy of Sciences of the United States of America*, vol. 102, pp. 12371-6, Aug 30 2005.
- [7] A. Lorincz, D. Haddad, R. Naik, V. Naik, A. Fung, A. Cao, P. Manda, A. Pandya, G. Auner, R. Rabah, S. E. Langenburg, and M. D. Klein, "Raman spectroscopy for neoplastic tissue

- differentiation: a pilot study," *Journal of Pediatric Surgery*, vol. 39, pp. 953-6; discussion 953-6, Jun 2004.
- [8] R. Rabah, R. Weber, G. K. Serhatkulu, A. Cao, H. Dai, A. Pandya, R. Naik, G. Auner, J. Poulik, and M. Klein, "Diagnosis of neuroblastoma and ganglioneuroma using Raman spectroscopy," *Journal of Pediatric Surgery*, vol. 43, pp. 171-6, Jan 2008.
- [9] *Deaths/Mortality*. Available: <http://www.cdc.gov/nchs/fastats/deaths.htm>
- [10] A. Jemal, R. Siegel, E. Ward, T. Murray, J. Xu, and M. J. Thun, "Cancer statistics, 2007," *CA: A Cancer Journal for Clinicians*, vol. 57, pp. 43-66, Jan-Feb 2007.
- [11] M. S. Anscher, P. Jones, L. R. Prosnitz, W. Blackstock, M. Hebert, R. Reddick, A. Tucker, R. Dodge, G. Leight, Jr., J. D. Iglehart, and et al., "Local failure and margin status in early-stage breast carcinoma treated with conservation surgery and radiation therapy," *Annals of Surgery*, vol. 218, pp. 22-8, Jul 1993.
- [12] C. C. Park, M. Mitsumori, A. Nixon, A. Recht, J. Connolly, R. Gelman, B. Silver, S. Hetelekidis, A. Abner, J. R. Harris, and S. J. Schnitt, "Outcome at 8 years after breast-conserving surgery and radiation therapy for invasive breast cancer: influence of margin status and systemic therapy on local recurrence," *Journal of Clinical Oncology*, vol. 18, pp. 1668-75, Apr 2000.
- [13] D. M. Herron and M. Marohn, "A consensus document on robotic surgery," *Surgical Endoscopy*, vol. 22, pp. 313-25; discussion 311-2, Feb 2008.
- [14] A. Pandya, "Medical augmented reality system for image-guided and robotic surgery: development and surgeon factors analysis," Dissertation, Biomedical Engineering, Wayne State University, 2004.

- [15] S. Fantini, S. A. Walker, M. A. Franceschini, M. Kaschke, P. M. Schlag, and K. T. Moesta, "Assessment of the size, position, and optical properties of breast tumors in vivo by noninvasive optical methods," *Appl Opt*, vol. 37, pp. 1982-9, Apr 1 1998.
- [16] J. C. Hebden, H. Veenstra, H. Dehghani, E. M. Hillman, M. Schweiger, S. R. Arridge, and D. T. Delpy, "Three-dimensional time-resolved optical tomography of a conical breast phantom," *Appl Opt*, vol. 40, pp. 3278-87, Jul 1 2001.
- [17] C. M. Sehgal, T. W. Cary, S. A. Kangas, S. P. Weinstein, S. M. Schultz, P. H. Arger, and E. F. Conant, "Computer-based margin analysis of breast sonography for differentiating malignant and benign masses," *Journal of Ultrasound in Medicine*, vol. 23, pp. 1201-9, Sep 2004.
- [18] J. R. Ferraro, K. Nakamoto, and C. W. Brown, *Introductory Raman spectroscopy*, 2nd ed. Amsterdam ; Boston: Academic Press, 2003.
- [19] T. Howley, M. Madden, M.-L. O'Connell, and A. Ryder, "The effect of principal component analysis on machine learning accuracy with high-dimensional spectral data," *Knowledge-Based Systems*, vol. 19, pp. 363-70, 2006.
- [20] R. Weber, "Comparison of discriminant function analysis and neural networks for tissue identification using raman spectroscopy," Thesis, Physics, Wayne State University, 2007.
- [21] L. Reisner, A. Cao, and A. Pandya, "An integrated software system for processing, analyzing, and classifying Raman spectra," *Chemometrics and Intelligent Laboratory Systems*, vol. In Press, 2010.

- [22] J. T. Motz, S. J. Gandhi, O. R. Scepanovic, A. S. Haka, J. R. Kramer, R. R. Dasari, and M. S. Feld, "Real-time Raman system for in vivo disease diagnosis," *J Biomed Opt*, vol. 10, p. 031113, May-Jun 2005.
- [23] T. C. Bakker Schut, M. J. Witjes, H. J. Sterenborg, O. C. Speelman, J. L. Roodenburg, E. T. Marple, H. A. Bruining, and G. J. Puppels, "In vivo detection of dysplastic tissue by Raman spectroscopy," *Analytical Chemistry*, vol. 72, pp. 6010-8, Dec 15 2000.
- [24] A. S. Haka, Z. Volynskaya, J. A. Gardecki, J. Nazemi, J. Lyons, D. Hicks, M. Fitzmaurice, R. R. Dasari, J. P. Crowe, and M. S. Feld, "In vivo margin assessment during partial mastectomy breast surgery using raman spectroscopy," *Cancer Research*, vol. 66, pp. 3317-22, Mar 15 2006.
- [25] A. Mahadevan-Jansen, M. F. Mitchell, N. Ramanujam, A. Malpica, S. Thomsen, U. Utzinger, and R. Richards-Kortum, "Near-infrared Raman spectroscopy for in vitro detection of cervical precancers," *Photochemistry and Photobiology*, vol. 68, pp. 123-32, Jul 1998.
- [26] R. Malini, K. Venkatakrisna, J. Kurien, K. M. Pai, L. Rao, V. B. Kartha, and C. M. Krishna, "Discrimination of normal, inflammatory, premalignant, and malignant oral tissue: a Raman spectroscopy study," *Biopolymers*, vol. 81, pp. 179-93, Feb 15 2006.
- [27] J. Brennan, Y. Wang, R. Dasari, and M. Feld, "Near-infrared Raman spectrometer systems for human tissue studies," *Applied Spectroscopy*, vol. 51, pp. 201-8, 1997.
- [28] A. Mahadevan-Jansen, M. F. Mitchell, N. Ramanujam, U. Utzinger, and R. Richards-Kortum, "Development of a fiber optic probe to measure NIR Raman spectra of cervical tissue in vivo," *Photochemistry and Photobiology*, vol. 68, pp. 427-31, Sep 1998.

- [29] J. D. Allendorf, M. Bessler, R. L. Whelan, M. Trokel, D. A. Laird, M. B. Terry, and M. R. Treat, "Postoperative immune function varies inversely with the degree of surgical trauma in a murine model," *Surgical Endoscopy*, vol. 11, pp. 427-30, May 1997.
- [30] K. H. Fuchs, "Minimally invasive surgery," *Endoscopy*, vol. 34, pp. 154-9, Feb 2002.
- [31] M. J. Mack, "Minimally invasive and robotic surgery," *JAMA*, vol. 285, pp. 568-72, Feb 7 2001.
- [32] A. R. Lanfranco, A. E. Castellanos, J. P. Desai, and W. C. Meyers, "Robotic surgery: a current perspective," *Annals of Surgery*, vol. 239, pp. 14-21, Jan 2004.
- [33] S. M. Prasad, C. T. Ducko, E. R. Stephenson, C. E. Chambers, and R. J. Damiano, Jr., "Prospective clinical trial of robotically assisted endoscopic coronary grafting with 1-year follow-up," *Annals of Surgery*, vol. 233, pp. 725-32, Jun 2001.
- [34] J. W. Cannon, J. A. Stoll, S. D. Selha, P. E. Dupont, R. D. Howe, and D. F. Torchiana, "Port placement planning in robot-assisted coronary artery bypass," *IEEE Transactions on Robotics and Automation*, vol. 19, pp. 912-17, 2003.
- [35] A. M. Chiu, D. Dey, M. Drangova, W. D. Boyd, and T. M. Peters, "3-D image guidance for minimally invasive robotic coronary artery bypass," *Heart Surg Forum*, vol. 3, pp. 224-31, 2000.
- [36] N. Navab, J. Traub, T. Sielhorst, M. Feuerstein, and C. Bichlmeier, "Action- and workflow-driven augmented reality for computer-aided medical procedures," *IEEE Comput Graph Appl*, vol. 27, pp. 10-4, Sep-Oct 2007.

- [37] S. Selha, P. Dupont, R. Howe, and D. Torchiana, "Dexterity optimization by port placement in robot-assisted minimally invasive surgery," in *2001 SPIE International Symposium on Intelligent Systems and Advanced Manufacturing*, 2001, pp. 97-104.
- [38] H. A. Tabaie, J. A. Reinbolt, W. P. Graper, T. F. Kelly, and M. A. Connor, "Endoscopic coronary artery bypass graft (ECABG) procedure with robotic assistance," *Heart Surg Forum*, vol. 2, pp. 310-5; discussion 315-7, 1999.
- [39] J. Traub, M. Feuerstein, M. Bauer, E. U. Schirmbeck, H. Najafi, R. Bauernschmitt, and G. Klinker, "Augmented reality for port placement and navigation in robotically assisted minimally invasive cardiovascular surgery," in *CARS 2004 - Computer Assisted Radiology and Surgery*, 2004, pp. 735-40.
- [40] A. L. Trejos, R. V. Patel, I. Ross, and B. Kiaii, "Optimizing port placement for robot-assisted minimally invasive cardiac surgery," *Int J Med Robot*, vol. 3, pp. 355-64, Dec 2007.
- [41] W. Kucharczyk and M. Bernstein, "Do the benefits of image guidance in neurosurgery justify the costs? From stereotaxy to intraoperative MR," *AJNR. American Journal of Neuroradiology*, vol. 18, pp. 1855-9, Nov-Dec 1997.
- [42] D. L. Pham, C. Xu, and J. L. Prince, "Current methods in medical image segmentation," *Annu Rev Biomed Eng*, vol. 2, pp. 315-37, 2000.
- [43] J. B. Maintz and M. A. Viergever, "A survey of medical image registration," *Medical Image Analysis*, vol. 2, pp. 1-36, Mar 1998.
- [44] C. Studholme, D. L. Hill, and D. J. Hawkes, "Automated 3-D registration of MR and CT images of the head," *Medical Image Analysis*, vol. 1, pp. 163-75, Jun 1996.

- [45] W. Lorensen, H. Cline, C. Nafis, R. Kikinis, D. Altobelli, and L. Gleason, "Enhancing reality in the operating room," in *IEEE Conference on Visualization '93*, 1993, pp. 410-15.
- [46] M. Rosenthal, A. State, J. Lee, G. Hirota, J. Ackerman, K. Keller, E. Pisano, M. Jiroutek, K. Muller, and H. Fuchs, "Augmented reality guidance for needle biopsies: an initial randomized, controlled trial in phantoms," *Medical Image Analysis*, vol. 6, pp. 313-20, Sep 2002.
- [47] R. Azuma, "A survey of augmented reality," *Presence: Teleoperators and Virtual Environments*, vol. 6, pp. 355-85, 1997.
- [48] M. Blackwell, C. Nikou, A. M. DiGioia, and T. Kanade, "An image overlay system for medical data visualization," *Medical Image Analysis*, vol. 4, pp. 67-72, Mar 2000.
- [49] A. Pandya, M. Siadat, L. Zamorano, J. Gong, Q. Li, J. Maida, and I. Kakadiaris, "Tracking Methods for Medical Augmented Reality," in *Medical Image Computing and Computer-Assisted Intervention*, Utrecht, The Netherlands, 2001, pp. 1404-05.
- [50] A. K. Solutions, "Kinematics of Robotic Manipulators," in *Robotics*, ed: Infinity Science Press LLC, 2007.
- [51] D. T. Gering, A. Nabavi, R. Kikinis, N. Hata, L. J. O'Donnell, W. E. Grimson, F. A. Jolesz, P. M. Black, and W. M. Wells, 3rd, "An integrated visualization system for surgical planning and guidance using image fusion and an open MR," *Journal of Magnetic Resonance Imaging*, vol. 13, pp. 967-75, Jun 2001.
- [52] U. Meier, O. Lopez, C. Monserrat, M. C. Juan, and M. Alcaniz, "Real-time deformable models for surgery simulation: a survey," *Computer Methods and Programs in Biomedicine*, vol. 77, pp. 183-97, Mar 2005.

- [53] T. McInerney and D. Terzopoulos, "Deformable models in medical image analysis: a survey," *Medical Image Analysis*, vol. 1, pp. 91-108, Jun 1996.
- [54] J. Warren and S. Schaefer, "A factored approach to subdivision surfaces," *IEEE Comput Graph Appl*, vol. 24, pp. 74-81, May-Jun 2004.
- [55] G. V. D. Bergen, *Collision Detection in Interactive 3D Environments*. San Diego, CA: Elsevier, 2004.
- [56] B. King, L. Reisner, S. Dworzecki, A. Cao, H. Wills, G. Auner, M. Klein, and A. Pandya, "Fusion of tomographic imaging with in vivo Raman cancer diagnosis using augmented reality," presented at the Computer Assisted Radiology and Surgery (CARS 2008), Barcelona, Spain, 2008.
- [57] J. Denavit and R. Hartenberg, "A kinematic notation for Lower-pair mechanisms based on matrices," *ASME Journal of Applied Mechanics*, vol. 22, pp. 215-21, 1955.
- [58] R. Paul, *Robot Manipulators: Mathematics, Programming, and Control*: The MIT Press, 1981.
- [59] P. Corke, "A Robotics Toolbox for MATLAB," *IEEE Robotics and Automation Magazine*, vol. 3, pp. 24-32, 1996.
- [60] L. Sciavicco and B. Siciliano, *Modelling and Control of Robot Manipulators*: London: Springer-Verlag London Limited, 2000.
- [61] D. Orin and W. Schrader, "Efficient computation of the jacobian for robot manipulators," *The International Journal of Robotics Research*, vol. 3, pp. 66-75, 1984.
- [62] V. Klema and A. Laub, "The singular value decomposition: its computation and some applications," *IEEE Transactions on Automatic Control*, vol. 25, pp. 164-76, 1980.

- [63] M. Martinsen, "A generic system for real-time tracking and 3D visualization of medical robotic manipulators," Thesis, Department of Mathematics, University of Oslo, Oslo, 2006.
- [64] Q. H. Li, L. Zamorano, A. Pandya, R. Perez, J. Gong, and F. Diaz, "The application accuracy of the NeuroMate robot--A quantitative comparison with frameless and frame-based surgical localization systems," *Computer Aided Surgery*, vol. 7, pp. 90-8, 2002.
- [65] M. Cossu, G. Lo Russo, S. Francione, R. Mai, L. Nobili, I. Sartori, L. Tassi, A. Citterio, N. Colombo, M. Bramerio, C. Galli, L. Castana, and F. Cardinale, "Epilepsy surgery in children: results and predictors of outcome on seizures," *Epilepsia*, vol. 49, pp. 65-72, Jan 2008.
- [66] T. R. Varma and P. Eldridge, "Use of the NeuroMate stereotactic robot in a frameless mode for functional neurosurgery," *Int J Med Robot*, vol. 2, pp. 107-13, Jun 2006.
- [67] B. King, L. Reisner, M. Klein, G. Auner, and A. Pandya, "Registered, sensor-integrated virtual reality for surgical applications," presented at the IEEE Virtual Reality 2007 (VR 2007), Charlotte, NC, 2007.
- [68] L. A. Reisner, B. W. King, M. D. Klein, G. W. Auner, and A. K. Pandya, "A prototype biosensor-integrated image-guided surgery system," *Int J Med Robot*, vol. 3, pp. 82-8, Mar 2007.
- [69] A. R. de Paula, Jr. and S. Sathaiah, "Raman spectroscopy for diagnosis of atherosclerosis: a rapid analysis using neural networks," *Medical Engineering and Physics*, vol. 27, pp. 237-44, Apr 2005.

- [70] M. Gniadecka, P. A. Philipsen, S. Sigurdsson, S. Wessel, O. F. Nielsen, D. H. Christensen, J. Hercogova, K. Rossen, H. K. Thomsen, R. Gniadecki, L. K. Hansen, and H. C. Wulf, "Melanoma diagnosis by Raman spectroscopy and neural networks: structure alterations in proteins and lipids in intact cancer tissue," *Journal of Investigative Dermatology*, vol. 122, pp. 443-9, Feb 2004.
- [71] S. Sigurdsson, P. A. Philipsen, L. K. Hansen, J. Larsen, M. Gniadecka, and H. C. Wulf, "Detection of skin cancer by classification of Raman spectra," *IEEE Transactions on Biomedical Engineering*, vol. 51, pp. 1784-93, Oct 2004.
- [72] S. M. Ali, L. A. Reisner, B. King, A. Cao, G. Auner, M. Klein, and A. K. Pandya, "Eye gaze tracking for endoscopic camera positioning: an application of a hardware/software interface developed to automate Aesop," *Studies in Health Technology and Informatics*, vol. 132, pp. 4-7, 2008.
- [73] A. Mudunuri, "Autonomous camera control system for surgical robots," Thesis, Electrical and Computer Engineering, Wayne State University, 2010.

ABSTRACT

OPTIMAL SURGICAL PORT PLACEMENT AND AUTOMATED ROBOTIC POSITIONING FOR RAMAN AND OTHER BIOSENSORS

by

BRADY KING

May 2011

Advisor: Dr. Abhilash Pandya

Major: Computer Engineering

Degree: Doctor of Philosophy

Medical biosensors can provide new information during minimally invasive and robotic surgical procedures. However, these biosensors have significant physical limitations that make it difficult to find optimal port locations and place them *in vivo*. This dissertation explores the application of robotics and virtual/augmented reality to biosensors to enable their optimal use *in vivo*.

In the first study, an automated intelligent port placement system for biosensor use was developed. Patient data was displayed in an environment in which a surgeon could indicate areas of interest. The system utilized biosensor physical limitations and provided the best port location from which the biosensor could reach the targets on a collision-free path. The study showed that it is possible to find an optimal port location for proper biosensor data capture.

In the second study, human performance in the task of port placement was evaluated to determine if computer intervention and assistance was needed. Using a virtual surgical environment, we present a number of targets on one or more tissue surfaces. A human factors study was conducted with 20 subjects that analyzed the subject's placement of a port with the

goal of scanning as many targets as possible with a biosensor. The study showed performance to be less than optimal with significant degradation in several specific scenarios.

In the final study, a surgical robot was investigated for potential use in holding and positioning a biosensor *in vivo*. A full control suite was developed for an AESOP 1000, enabling the positioning of the biosensor without hand manipulation. It was found that the robot lacks the accuracy needed for proper biosensor utilization. Specific causes of the inaccuracies were identified for analysis and consideration in future robotic platforms.

Overall, the results show that the application of medical robotics and virtual/augmented reality is able to overcome/mitigate many of the significant physical limitations inherent to biosensor design that currently limit their use in surgery. We conjecture that a complete system, with a more accurate robot, could be used *in vivo*. We believe that results taken from the individual studies will result in improvements to pre-operative port placement and robotic design.

AUTOBIOGRAPHICAL STATEMENT

Brady King was born April 23, 1981, in Royal Oak Michigan. He obtained a Bachelor of Science (B.S.) degree in Computer Engineering (2003) from Lawrence Technological University, and a Master of Science (M.S.) degree in Computer Engineering (2005) from the University of Michigan Dearborn.

In 2005, he came to Wayne State University to pursue a Ph.D. where he has been doing research in medical robotics, visualization, pre-operative planning, and biosensors. His major projects include pre-operative planning software for minimally invasive surgical ports, automation of surgical robots, pre-operative planning for ablation procedures, and an automated Raman spectroscopic probe.

Mr. King has presented his work at several conferences to the medical and engineering community. He has 9 publications in peer-reviewed journals and conferences. He is a member of the Tau Beta Pi engineering honors society and an avid baseball player and bowler.